ACTIVE MICROGRAVITY VIBRATION ISOLATION USING PVDF POLYMER PIEZOELECTRIC ACTUATORS

by

DAVID SCOTT STAMPLEMAN

B.S., Massachusetts Institute of Technology
(1986)

SUBMITTED IN PARTIAL FULFILLMENT OF
THE REQUIREMENTS FOR THE DEGREE OF

MASTER OF SCIENCE
IN AERONAUTICS AND ASTRONAUTICS

at the

MASSACHUSETTS INSTITUTE OF TECHNOLOGY

February 1991

Signature of Author ________________________________
Department of Aeronautics and Astronautics
January 22, 1991

Certified by ________________________________
Professor Andreas H. von Flotow
Thesis Supervisor, Department of Aeronautics and Astronautics

Accepted by ________________________________
Professor Harold Y. Wachman
Chairman, Departmental Graduate Committee

ACTIVE MICROGRAVITY VIBRATION ISOLATION USING PVDF POLYMER PIEZOELECTIC ACTUATORS

by

DAVID SCOTT STAMPLEMAN

Submitted to the Department of Aeronautics and Astronautics on
January 22, 1991
in partial fulfillment of the requirements for the
Degree of Master of Science in Aeronautics and Astronautics

ABSTRACT

Scientists want to take advantage of the near zero gravity environment of space, because sensitive products manufactured on Earth are distorted by its gravitational force. Although in low earth orbit the magnitude of the distorting forces is not zero, it decreases dramatically to one millionth of Earth's surface gravity, a microgravity. The mounting structure for the processing facility must be able to isolate it from the additional spacecraft disturbances which dominate at frequencies above 0.01 Hz. Passive isolation is not sufficient because the likely minimum umbilical cord stiffness of 2 N/m prevents the system resonant frequency from getting this low. Active isolation is only needed between 0.01 and 5 Hz if an active soft mount approach is taken. The mount is made as soft as possible to take advantage of high frequency passive isolation and only has to be active in the above frequency range. The mount must be able to overpower the umbilical cord in order to negate the forces transmitted to the microgravity facility.

A laminated piezoelectric actuator mount has been developed for microgravity isolation. Laminated piezoelectic actuator theory is presented along with the technology developed to make the actuator a reality. The equations are specialized for laminated arc actuators. The pure mechanical dynamics were close to prediction while the arc piezoelectric response was shown to be predictable only to an approximate level. Nonlinear behavior was also observed due to the geometry of an expanding arc. Ways were found to design around these and other problems inherent to the laminated piezoelectric polymer actuator. The final mount used in the experiment consists of six semicircular laminated PVDF arcs each clamped at one end to the spacecraft and hinged at the other end to the payload. A microgravity environment sufficient enough to verify the properties of the PVDF laminated arc actuators was simulated using an air table and measured with accelerometers; but it was not quiet enough to perform a control experiment that demonstrates absolute performance. The mount has an approximate stiffness of 10 N/m and can overpower itself and the umbilical cord for displacements of at least 2.5 mm. These are the minimum characteristics of a satisfactory microgravity mount. The system response was also fairly close to that predicted. Laminated polymer piezoelectric actuator technology has shown itself to be a serious option for performing microgravity isolation.

Thesis Supervisor: Dr. Andreas von Flotow

Title: Associate Professor of Aeronautics and Astronautics

Acknowledgements

I would like to take this opportunity to thank all of those who helped make this project and my work towards my masters degree successful. This project would not have been the same without Andy's guidance and practical advice. I have certainly learned a great deal over the last couple of years. The dedicated days and nights at M.I.T. would not have been nearly as successful without the comradery and valuable help and advice of Bob, Farla, Simon, Kelvin, and everyone else at SERC. Don and Earl's patience and expertise in helping with the construction of the lab experiment were equally invaluable. Undergraduate laboratory assistants Carl and Dan also provided many hours of quality work which were instrumental in this project's success. But most of all, I would like to thank Anne Marie, Joe, and my parents for their unwavering support through some very difficult moments; without them, this would not have been possible.

David S. Stampleman
January 22, 1991

Table of Contents

List of Figures

List of Tables

Chapter 1

Introduction

1.1 Motivation/Objective

This research is borne out of a desire to improve the technology available to solve the disturbance rejection problems inherent in the deployment of payloads on large space-based platforms. Many platforms are being designed to perform a multitude of missions that have stringent requirements.[1,2,3] Unfortunately, the payloads on these platforms are subject to small but nonetheless significant environmental disturbances and more tangible disturbances caused by man and machine. Some scientists have expressed a desire to use instruments for astronomy missions which require pointing accuracies as small as a microarcsecond (μasec). Also needed are isolation facilities that limit the accelerations transmitted to a payload to less than a microgravity for crystal growth or other types of materials processing. A microgravity (μg) is an acceleration level that is a fraction (10^{-6}) of that experienced on the surface of the earth (one g) . The space station in low earth orbit (LEO) is an obvious near term application upon which this type of research can be focused. The space shuttle orbiter is another example. On a platform such as a space station, there are many payloads and many disturbance sources. The isolation of these payloads from any disturbance is examined as a crucial element for the success of their missions. The author's additional personal desire is to develop and implement actual hardware in order to show its readiness and applicability for current and future use. Microgravity vibration isolation of a payload on the space station using piezoelectric polymer laminated film actuators is the fruition of this project.

One of the capabilities much publicized of the space station and other orbiting space platforms is the prospect of manufacturing products free from the distortion of Earth's surface gravity. When exposed to the near free-fall or zero-gravity environment of space, these forces are reduced dramatically. However, minute forces still exist. In LEO, small forces on the order of 10^{-6} of Earth's surface gravity are necessary to keep a microgravity facility from drifting away from the platform to which it is attached or from hitting the walls of its containment area. The direction and magnitude of these forces and torques are either static or they cycle at once or twice the orbital rate of approximately 10^{-4} Hz. The limiting factors are environmental forces and torques caused by gravitational, aerodynamic, solar and magnetic effects inherent to the orbital environment. They cannot be eliminated. However, many artificial, or man-made, disturbances that originate on the spacecraft do not necessarily have to be experienced by the microgravity facility. These disturbances need attenuation at frequencies above 0.01 Hz. If the disturbance is sinusoidal, this translates to a displacement of ± 2.5 mm. Ideally these disturbances could be filtered out by making the mount soft enough to act like a shock absorber. To get the corner frequency below 0.01 Hz, a stiffness of no greater that of 0.4 N/m is required for a microgravity facility of 100 kg. Not only is this very soft but it is softer than the 2 N/m supply line, or umbilical cord, stiffness likely to be necessary for the operation of the facility. This umbilical cord stiffness still provides a fair amount of isolation but not quite enough. Active enhancement is necessary to achieve the microgravity isolation goal. Solutions have already been formulated for this problem using magnetic mounts and air jets.[4,5,6,7]

Piezoelectricity is a material property such that when a material that possesses it is strained, electric charge is produced. There is a piezoelectric polarity direction to this property. When electrodes perpendicular to this direction are placed on either side of the material, the electric charge produced within the volume of piezoelectric material between the electrodes accumulates on those electrodes. This property is taken advantage of in many products such as sensors and phonograph needles.[8] The converse is also true: if electric charge is added to the electrodes encasing the piezoelectric material, strain is induced. It is this latter property which is exploited in the actuation of a piezoelectric material. There have been many applications using ceramic piezoelectric materials as actuators because of the high extensional modulus and forces that result.[9,10] Piezoelectric polymers are much softer than ceramics and the forces resulting from the piezoelectric strain are correspondingly lower. This tends to limit polymer piezoelectric materials to applications of lower force levels when it is used as an actuator. One advantage PVDF polymer film has over ceramic material is that it is capable of larger strain magnitudes. The proposed or actual use of the active properties of piezoelectric polymers is not new but, due to the higher force capability of piezoceramic materials, the applications have been relatively scarce.[8,11-16] Fortunately, the forces affecting a body orbiting around Earth are quite small; and since the necessary stiffness of a microgravity mount is small, and a relatively large amplitude of motion is required, PVDF film finds itself in an environment suited to its capabilities.

This document will explain the above concept in more detail, discussing the basic physics of the problem, the proposed solution and experimental design, and the actual experimental results and conclusion. Chapter 2 outlines the environmental and man-made disturbances and how they affect the microgravity facility, also called the payload. With these dynamics, a representative single degree of freedom model is devised to explore the issues involved in controlling the system intended to isolate the facility from the vibrations of the spacecraft. Using this information it is then shown why this method was chosen over other capable methods. Chapter 3 discusses the PVDF laminated actuator in detail. The chapter is a basic toolbox for use in the design of the PVDF laminated arc. It presents a method of analyzing them and suggests other approaches that might be taken for further derivative actuators. Knowledge of the actuator manufacturing procedure and its corresponding considerations is also necessary for proper design and is correspondingly included. Due to the fact that the mounting conditions of the actuator within the system is crucial to its effectiveness, different mounting configurations are presented, making use of a novel hinged end condition that improves actuator performance.

The second half of this document describes the three degree of freedom experiment performed to verify the capabilities of the PVDF actuator and presents its results. Chapter 4 details all of the laboratory and arc mounting configuration hardware. The reasons for choosing a mount consisting of six laminated PVDF arcs clamped at one end and hinged at the other are discussed; and this is followed by an analysis of the final system as a whole. The choice of feedback sensor and payload suspension were major issues in the experimental design. Although the resulting solutions are relatively simple compared to other methods considered, they were not readily apparent. The type of sensor used for the control feedback dictates the complexity of the system. Fortunately the simplest approach, an accelerometer, is possible. Typical units of the commericially available accelerometer are capable of satisfactory resolution levels; but this resolution tests the limits of the sensors and is better than the published specifications. Satisfactory performance is achievable but it is not guaranteed for the specific units in the experiment. The search for another type of sensor is outlined in Appendix B because of its influence in the design of a microgravity mount. Chapter 5 then discusses the experimental results for a single arc, an actuator grouping of two back-to-back arcs called a node, and the complete three DOF experiment. The conclusions of this research investigating the capability of a laminated polymer PVDF piezoelectric actuator are then outlined in Chapter 6.

Chapter 2

The Problem of Microgravity Vibration Isolation in Low Earth Orbit

2.1 Overview

Scientists want to take advantage of the so called zero-g environment of space. Materials such as ball bearings and other precision products manufactured on earth are made in an unavoidable one-g environment. These products include high quality crystals grown for many applications. Gravitational forces distort these products during manufacture. Consequently these manufacturing processes can benefit from a zero-g environment. Near zero-g environments have been produced on Earth by letting items travel in free-fall but this only allows it to be a matter of seconds in duration. Unfortunately, space is not a zero-g environment either. Although the forces may be small, they are not negligible. Gravitational, aerodynamic, solar, and magnetic forces and torques are present. The respective payload and spacecraft (also called platform) missions determine which of these factors is dominant. This chapter will explain these forces and torques but concentrate on those which dominate the zero-g isolation problem on the space station. It is these forces which hold us from isolating to below 10^{-6} g's (1 microgravity or 1 μg) in LEO.

This chapter will also look at the basic single degree of freedom control problem for the isolation of a space based payload from any unwanted disturbances. It will cover the dynamics of such a mission and the requirements of the hardware involved. Also included are descriptions of approaches that have been attempted or proposed. All of this information will be geared toward determining how and to what degree the acceleration attenuation levels desired by the scientists and manufacturers hoping to use such a facility can be achieved.

2.2 Isolation Requirements

The vibration isolation of sensitive payloads is a significant problem with its own characteristics. The positioning of the payload is a relatively minor concern in that the mount must simply prevent the payload from drifting out of its designated area. The specification that is of utmost importance to a space based microgravity facility is that of the maximum allowable acceleration.[4,17] Figure 2.1 shows the levels of acceleration that are considered ideal from the payload performance standpoint.[4] Manufacturing facilities requirements appear to get more stringent at lower frequencies while crystal growth is not as demanding. Consequently materials processing drives the low frequency requirements envelope while crystal growth does the same for the higher frequencies. If these requirements are those desired by the potential users of a microgravity facility, it is up to the engineer to determine what levels are practical in a actual implementation in LEO. These physical limitations are explained in the following sections.

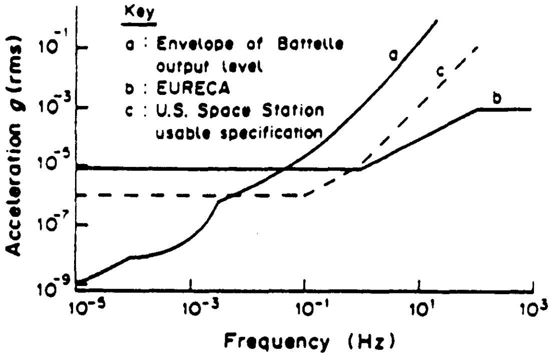

Figure 2.1: Acceleration levels desirable for materials processing (a) and crystal growth (b).

2.3 The Orbital Environment

Many environmental forces are imposed on the dynamics of an orbiting body. Gravity is the most obvious of these forces. It governs the orbital trajectories of these bodies. If a body or multi-body configuration is not inertially balanced, the existing gravity gradient will impose a torque upon it. Gravity gradient also imposes small tidal stresses within any finite body in orbit. The reaction of the structure with the Earth's magnetic field is also a consideration when the specific design of a certain system is attempted. This is usually an order of magnitude below that of the gravity gradient torque, however, and should not dictate the choice of mounting system. A spacecraft orbiting Earth experiences aerodynamic drag forces due to Earth's atmosphere. There will also be solar radiation pressure when the spacecraft is not in the shadow of the Earth. These last two forces act on the projected area of the spacecraft. If the center of pressure is different from the center of gravity, the spacecraft will be subject to additional torque. Two co-orbiting bodies, a payload and its spacecraft for instance, may be affected differently.

The disturbances mentioned above cycle at once or twice the orbital rate of the satellite. The orbital rate is at its highest at low earth orbit (LEO) where it is approximately 10^{-4} Hz. The next few sections summarize the important aspects of these forces as they relate to the choice of mounting structure. A detailed description of these disturbances and how to quantify them is given in Reference 18. A similar description characterizing these disturbances and how they affect the attitude control system (ACS) of the Space Station is given in Reference 19.

This section will also examine the man-made disturbances that appear in a spacecraft. These disturbance forces and torques can be caused by actual astronaut movement or originate from the operation of certain equipment or machines. There will be a brief overview of these man-made disturbances; those disturbances which are likely to be of most interest will be discussed in more detail. Once the disturbance environment has been characterized, a disturbance profile will be chosen and compared to a desired disturbance limit. This will result in an isolation performance specification for a microgravity facility

2.3.1 Gravity Gradient

The classical gravitational attractive force between two point masses is

$$F = Gm_1m_2/r_c^2 \qquad (2.3.1.1)$$

where, G = gravitational constant = $6.67\text{x}10^{-11}$
m_1, m_2 = masses of the two bodies
r_c = distance between the point masses

This comes from Newton. For a distributed body orbiting a spherically symmetric primary, the force and torque exerted by gravity upon the body is calculated as an integral over the body;

$$\vec{f} = -Gm_1 \int_B \frac{\vec{R}\,dm}{R^3} \tag{2.3.1.2}$$

and also

$$\vec{g} = -G \int_B \frac{\vec{r} \times \vec{R}}{R^3}\,d\,m \tag{2.3.1.3}$$

where, $\vec{f}$ = the force vector acting on the orbiting body
m_1 = the mass of the primary body (earth)
$\vec{R}$ = the radial vector from the center of the primary body to an infinitesimal mass element
R = magnitude of $\vec{R}_c$
dm = elemental mass of the orbiting body
$\vec{g}$ = the torque vector acting on the orbiting body

After executing some vector algebra and ignoring some higher order terms, one realizes that the highest torques result from an inequality of the moments of inertia along the different body axes. This occurs when the body's principal axes are not aligned with the local vertical / local horizontal axes (defined by the satellite's motion about the primary body).[20]

$$|g| = \tfrac{3}{2}\omega^2(I_R - I_Y) \tag{2.3.1.4}$$

where, $|g|$ = the magnitude of the torque vector
ω = the orbital velocity of the satellite (rad/s)
I_R , I_Y = the roll and yaw moments of inertia

For a visual aid to understand these variables see Figure 2.2.[18] In the absence of other torques, gravity gradient torques can lead to slow pitch, roll, and yaw librations with periods comparable to or longer than the orbital rate. This will lead to periodic centripetal and tangential accelerations on the order of $\omega^2 L q_{max}$, where L is the distance to the spacecraft center of gravity and q_{max} the amplitude of the libration. These cyclic inertial forces are smaller than the static gravity gradient forces discussed in the next paragraph.

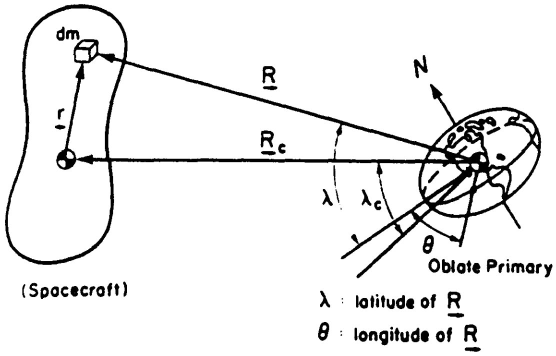

Figure 2.2: Spacecraft in the gravitational field of one inertially nonspherical primary body.

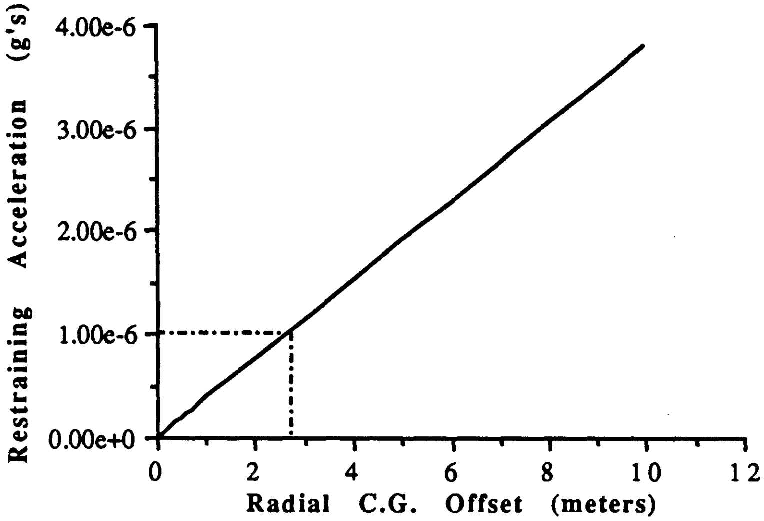

Figure 2.3: Centripetal force necessary to keep an attached payload orbiting the Earth at LEO at the same rate as the platform.

Figure 2.3 shows the centripetal force necessary to keep an attached payload orbiting at the same orbital frequency as the basebody for a particular radial c.g. offset. This "tidal" acceleration is 0.5 milli-g (mg) per meter at LEO, thus at LEO a static nano-g environment is only possible when within a half of a centimeter of the c.g. of the orbiting body. Reference 19 contains figures showing ellipses that represent the μg levels achievable on the Space Station. The author's copy is not suitable for reproduction here but Figure 2.4 is an approximate version, redrawn on a computer, that illustrates the static acceleration levels achievable on the Space Station.

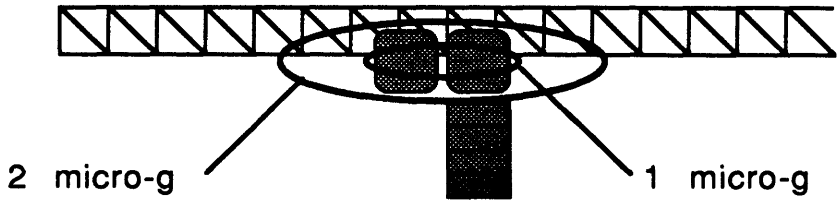

Figure 2.4: Acceleration levels achievable on the Space Station

2.3.2 Aerodynamic Forces

The basic aerodynamic force on an orbiting body as described by Hughes[18] is

$$\vec{f} = (\rho_a V_R^2 A_p)\,\hat{\vec{V}}_R \qquad (2.3.2.1)$$

and

$$\vec{g} = \vec{c}_p \times \vec{f} \qquad (2.3.2.2)$$

where, $\hat{\vec{V}}_R$ = the unit vector of the local atmosphere velocity vector

V_R = the magnitude of $\hat{\vec{V}}_R$

ρ_a = the local atmospheric density

A_p = the projected area of the satellite that the flow sees

$\vec{c}_p$ = the vector of the center of pressure offset from the center of mass (torque moment arm)

Aerodynamic forces may cycle at twice the orbital rate due to the bulge in the Earth's atmosphere at the equator. If the inclination of the orbit is large enough, the density of the atmosphere seen by the body will cycle twice per orbit. It should be noted that two objects in approximately the same orbit may decelerate at different rates and this difference should be taken into account when designing a mount that has to compensate for this effect. For the Space Station, the corresponding acceleration levels are about 0.25 μg directly from aerodynamic drag forces, and then another 0.1 μg from torques caused by the displacement of the aerodynamic center of pressure from the center of gravity.

2.3.3 Solar Pressure

An estimate of the pressure exerted on the orbiting body is given by

$$\vec{f} = p_s A_p \hat{\vec{s}} \qquad (2.3.2.3)$$

where, p_s = 4.5×10^{-6} N/m^2 = the solar radiation pressure

$\hat{\vec{s}}$ = the vector from the sun to the orbiting body

The accuracy of this calculation depends on how well the material of the body, in this case a spacecraft, absorbs the solar radiation. The magnitude and, to a lesser extent, direction will change depending on how or if the photons rebound off of the body. For exact determination of these values see Reference 18. At LEO the solar radiation pressure is over powered by the aerodynamic and gravity gradient effects. The total environmental acceleration contribution from these forces and torques when applied to the Space Station is approximately 0.01 μg. However, as altitude increases, the atmospheric density decreases and gravitational forces become weaker. At geo-synchronous orbit (GEO) and beyond, solar radiation pressure becomes a major environmental disturbance if not the primary one.

2.3.4 Man-made Disturbances

There are also man-made disturbances in the orbital environment that must be attenuated to enable the microgravity facilities to achieve their full potential. There have been various studies on the disturbance environment of an orbiting spacecraft. The types of disturbances and typical values for a generic artificial satellite are shown in Figure 2.5.[21] Missing from this figure are astronaut induced disturbances such as wall push-offs and treadmill use. These peak above 10^{-2} Hz. (more typically at around 1 Hz.). The induced acceleration levels can be as high as 10^{-2} g's. Some data has even been taken from orbiter missions, showing accelerations of many milli-g due to treadmill use.[22,23] Mid deck accelerations due to astronaut treadmill usage were measured at approximately 5 mg in a frequency range of about 1 to 2 Hz. In any case, it is difficult to determine an accurate disturbance spectrum specification until the platform design is near completion. With this in mind, a sinusoidal disturbance envelope was deduced by Jones et al. and is shown here in Figure 2.6 a).[4] This envelope was determined using European space station disturbance studies and correlated well with the previously mentioned disturbance studies.[1] The man-made disturbance envelope climbs above 1 µg at 0.01 Hz and marks the minimum frequency where isolation becomes necessary.

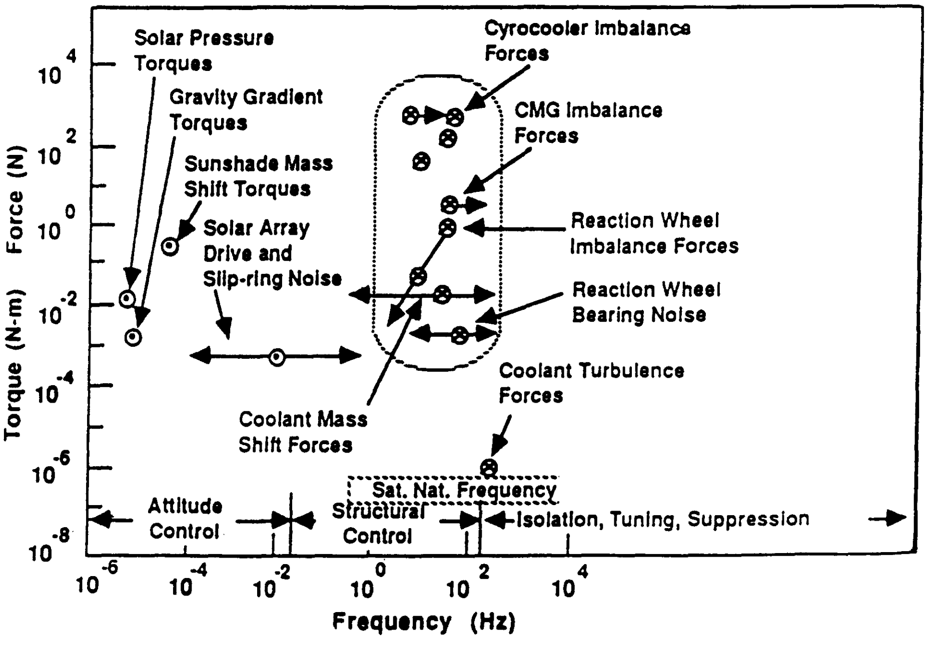

Figure 2.5: Spacecraft originating disturbances

An acceleration limit profile was derived from the previously stated requirements of the isolation facility users and modified according to what is possible in LEO. It too is taken from Jones et al.because of its direct applicability to the problem at hand and because of the desire to have a direct comparison with other methods (specifically, the method used by Jones et al.).[4] This profile is shown in Figure 2.6 b) and when subtracted from that of the disturbance, results in a disturbance attenuation or vibration isolation profile shown in Figure 2.6 c).

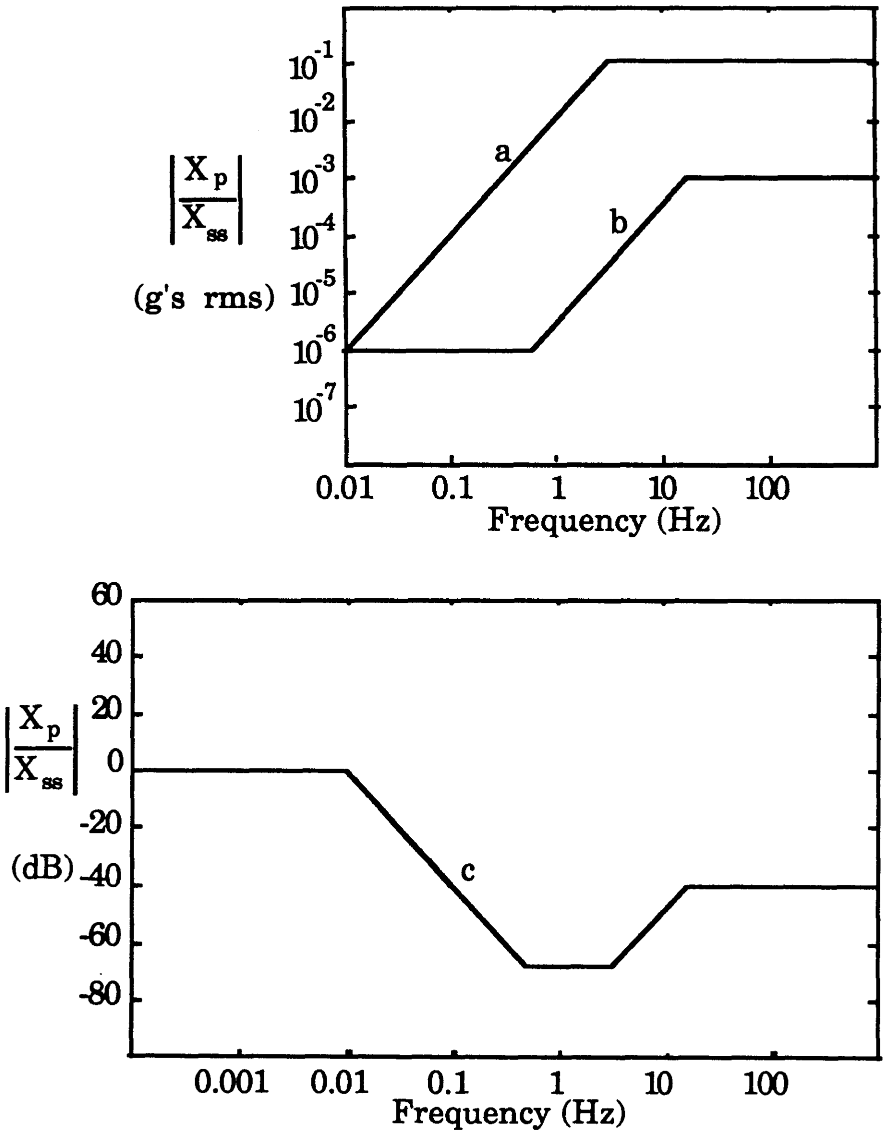

Figure 2.6: Vibration isolation requirements for a microgravity isolation mount. a) Disturbance envelope, b) Acceleration level limit profile for DC microgravity isolation, and c) The disturbance rejection profile.

2.4 The Payload/Mount System

The crucial mount requirement, the isolation specification (Figure 2.6 (c)) has been stated. The following section will expand upon any physical requirements of the mount that stem from this specification and those requirements that have other origins. With this in mind, a single degree of freedom model can be formulated for use as a general design tool.

2.4.1 Payload/Mount Requirements

Figure 2.6 is a sinusoidal specification from which physical meaning can be drawn. If $x_{ss} = A\sin\omega t$ represents the displacement of the basebody then its acceleration is $\ddot{x}_{ss} = -A\omega^2\sin\omega t$. Consequently, above 0.01 Hz., the mounting structure will be moving with the amplitude A which is 2.5 mm. The mount must be able to accommodate payload motion from an equilibrium position of ± 2.5 mm. The mount should also be able to isolate motions of greater amplitude since most disturbances are not sinusoidal in nature. Together with the stiffness of the mount, this displacement also yields the control force necessary to be applied to the payload in order to cancel out that which has been transmitted through the mount. The mount stiffness is a crucial factor in deciding what type of isolation scheme is necessary.

The mount stiffness is dictated by the functions it must perform. Apart from isolating the payload from the orbital disturbances power, data, and coolant flow must exist in order for the mission to be a success. These functions are the lifeline to the envisioned 100 kg payload and are labelled here as umbilical functions. The mount performs them somewhat like an umbilical cord, carrying power, data, and coolant to and from the payload. The characteristic that most affects the nature of the disturbance rejection problem is the stiffness required by this umbilical cord. The author is presently not aware of any extensive literature characterizing umbilical cords. This type of analysis has only been addressed when needed for a certain mission. The numbers used here have been drawn from the work of two microgravity isolation mount studies: Jones et al., 1987, and Gerhold and Rocha, 1987.[4,7] As stated previously, the mount must transfer data, power, and coolant between the payload and the basebody. Low stiffness data and power transfer can be achieved through wiring configurations involving coiling to achieve a soft spring. A common telephone cord helix has an approximate stiffness of 10 N/m. Zero stiffness transfer can even be attained through non-contact methods. However, if the payload is unable to dissipate enough heat it must attach itself to the basebody cooling system. The umbilical must be able to accommodate the flow of coolant. The cost, mass, or space taken up by non-contact methods may also be prohibitive. Jones et al. derive a minimum stiffness of 2 N/m while Gerhold and Rocha design for that of 5 N/m. Beyond this apparent minimum stiffness of 2 - 5 N/m the dynamics of the umbilical cord are very uncertain. A microgravity isolation mount should be robust enough to take this uncertainty into account.

Beyond the basic isolation requirements, there are also certain characteristics that are desirable for a microgravity facility and its mount. Any piece of working space hardware should have graceful failure characteristics; it should be able to perform to a certain degree if something should partially or fully fail. There are always the ever-present concerns regarding the demands this isolation system puts on the platform as well. Space and mass are always expensive commodities in a space venture. Power usage and production costs are also a major concern. All of the above topics should be considered when deciding upon an isolation system.

2.4.2 A Single Degree of Freedom Model

When analyzing a multi-degree of freedom problem much insight can be gained by investigating a representative model that captures most or all of the major issues involved. This is no exception. A single degree of freedom model will be introduced which will guide the reader through a fair portion of the isolation method choice and ensuing design until the multidimensional factors become apparent. A multi-degree of freedom model for the three DOF lab experiment will be introduced at a later point to address the issues that may become apparent when designing a mount that will have to work in six degrees of freedom while in orbit. The system can be simplified and visualized as two masses (the payload and the platform) connected by a spring (the mount). Since the platform (approximately 200,000 kg) is extremely massive compared to the payload (100 kg), and the disturbance is specified in terms of the acceleration of the mounting interface with the basebody, it can be looked upon as a rigid wall undergoing imposed motion (see Figure 2.7 a)). We now have a simple single degree of freedom model that can be compared to our isolation specification.

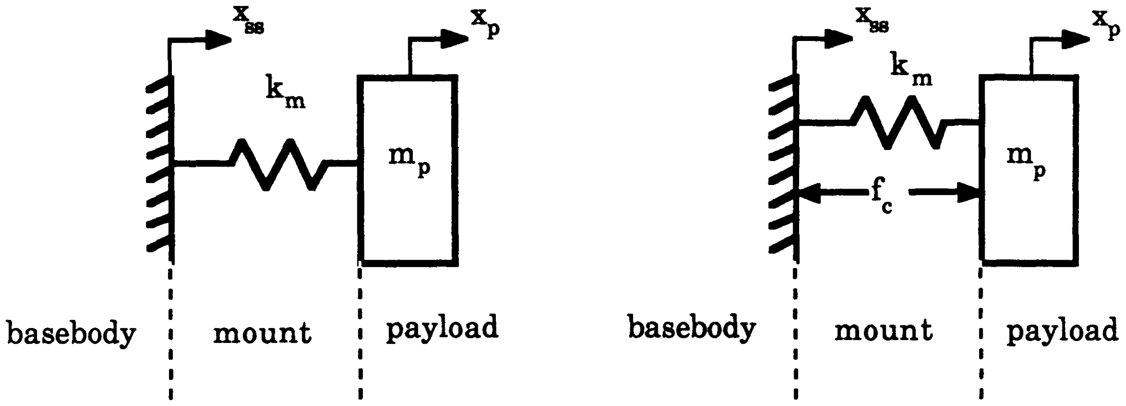

a) Actuator not modelled

b) Actuator modelled

m_p	Payload mass	x_{ss}	Basebody (space station) disturbance displacement
k_m	Mount stiffness	f_c	Control force (from actuator)
x_p	Payload displacment		

Figure 2.7: The payload/basebody system modeled as a mass attached to a rigid wall by an active spring: a) actuator not modeled b) actuator modeled.

In summary, the system can be modeled as a mass, a spring, and a rigid wall. The mass is the 100 kg microgravity facility; the spring is the 2 - 5 N/m umbilical cord/mount; and the rigid wall introduces the acceleration disturbance prescribed by Figure 2.6 a). The equation which describes the motion of this system is

$$m_p\ddot{x}_p + k_u x_p = k_u x_{ss} \tag{2.4.2.1}$$

which when transformed into the Laplace domain is

$$(ms^2 + k_u)X_p = k_u X_{ss} \tag{2.4.2.2}$$

and then the following transmissibility function from basebody displacement to payload displacement can be derived

$$\frac{X_p(s)}{X_{ss}(s)} = G(s) = \frac{k_u}{ms^2 + k_u}. \qquad (2.4.2.3)$$

This is also the acceleration transmissibility function because adding a multiplicative s^2 term in both the numerator and the denominator is a multiplication by unity. The previously mentioned physical parameters of the system can then substituted into this equation and plotted on top of the isolation specification (Figure 2.8 a)). The nominal microgravity facility mass of 100 kg is used for m_p as well as the minimum umbilical cord stiffness of 2 N/m. We can see that to meet the specification, further measures are needed in the range from 0.01 to approximately 1 Hz. If a passive system was to have the desired corner frequency of under 0.01 Hz, the mount would have to have a spring stiffness of under 0.4 N/m, which is extremely soft. A typical helical telephone cord has a stiffness of 10 to 20 N/m. The same resonant frequency can be achieved with a payload which has the mass of a garbage truck and is attached to the space station with this telephone cord. An actuation system that provides cancelling forces determined by a controller with feedback from sensors is needed only if the mount stiffness is greater than that necessary, 0.4 N/m, to keep the

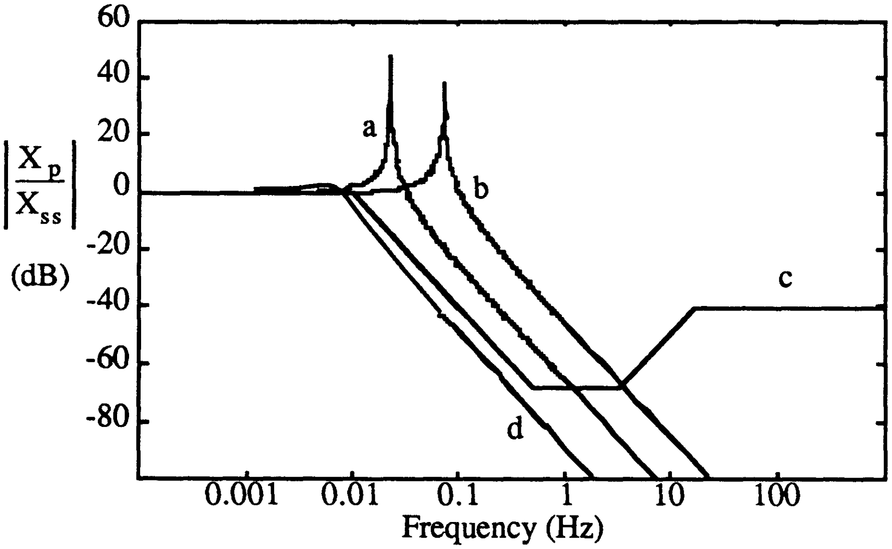

Figure 2.8: Isolation performance of the mount: a) without any active enhancement, b) with active mount turned off, c) required performance, and d) with active mount turned on.

resonant frequency below 0.01 Hz.

The actuator is modeled as being in parallel to the umbilical cord or mount spring (see Figure 2.7 b)). The first two equations in the previous section then become

$$m_p\ddot{x}_p + k_m x_p = k_m x_{ss} + f_c \qquad (2.4.2.4)$$

$$(ms^2 + k_m)X_p = k_m X_{ss} + F_c \qquad (2.4.2.5)$$

where k_m is the composite mount stiffness of the umbilical cord stiffness, k_u, and the actuator stiffness, k_a. Since acceleration is the specified performance metric, a control force should in some way be based upon it. The Laplace domain transfer function, K(s), between the accelerometer and the control force can be introduced into the above equation by substituting in $F_c(s) = -K(s)s^2X_p(s)$, where $s^2X_p(s)$ the acceleration of the payload. The equation is then rearranged so that a transfer function from $X_{ss}(s)$ to $X_p(s)$ is produced. It is also shown in its block diagram form in Figure 2.9.

$$X_p(s)=\frac{k_m}{s^2[m_p + K(s)]+k_m}X_{ss}(s) \qquad (2.4.2.6)$$

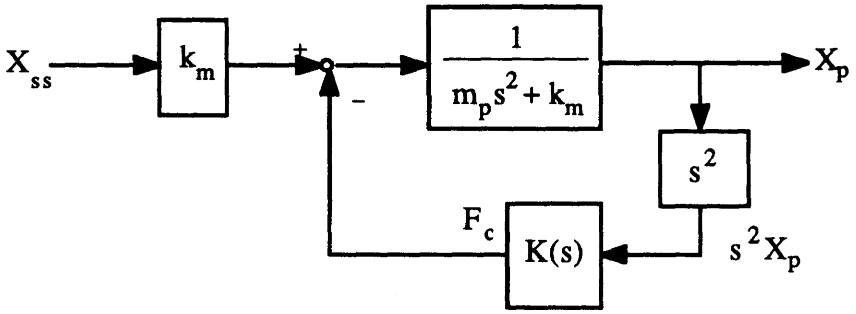

Figure 2.9: Control loop for acceleration feedback control

The choice of compensator is made easily when one looks at the denominator of the above transfer function. Since the compensator only enters into this equation as an additive term in the s^2 coefficient along with the mass of the payload, then if the compensator is real and positive, the effective mass of the system can be increased so that the system resonant frequency is below 0.01 Hz (Figure 2.8 b)). This is output feedback with constant gain. The resonant frequency of the system becomes $\sqrt{k_m/(m_p + K_c)}$, where K_c is the gain of the compensator. As the gain of the compensator is increased, the resonant frequency of the system can be lowered. This can also be visualized by looking at the open loop root locus of the system (Figure 2.10 a)).

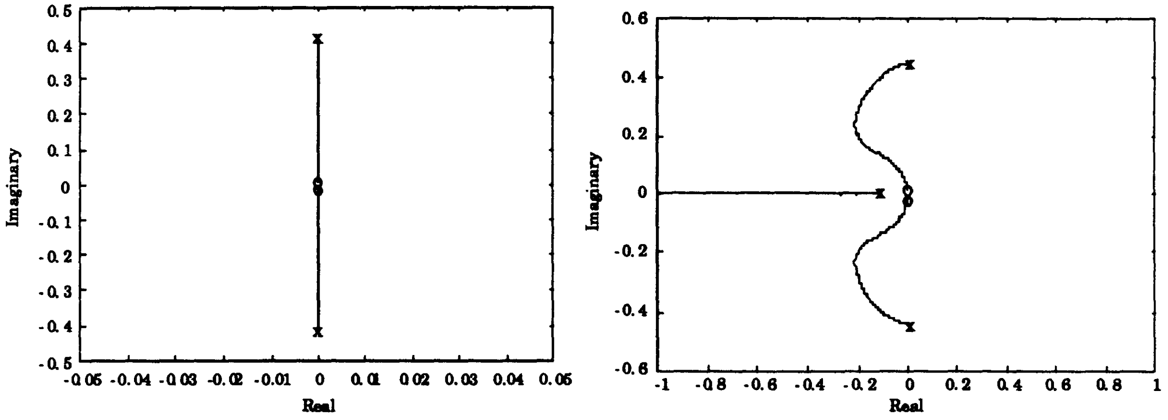

a) Gain feedback of acceleration b) Lag compensation

Figure 2.10: Root locus of the single degree of freedom spring mass system.

This basic control concept is that of a semi-active soft mount. The high frequency isolation characteristics of a soft spring are exploited and active isolation is only used in the frequency range of interest. This approach of using actively enhanced passive microgravity isolation has already been taken on Earth with a commercially available isolation table called EVIS (Electronic Vibration Isolation System) produced by the Newport Corporation.[24] The table surface sits on elastomeric supports and the whole system has passive resonant frequency of around 15 Hz. This corner frequency is effectively lowered to approximately 1 Hz using the proprietary sensing and isolation hardware that is at these supports. It is claimed that this system keeps vertical and horizontal accelerations of the table to as low as 3 μg rms, limited by servo noise.

For the purposes of the space based microgravity isolation problem, the frequency range of active enhancement can be seen in Figure 2.8 b). Isolation is necessary at frequencies as low as 0.01 Hz and possibly as high as 10 Hz depending on the composite stiffness of the mount. The sensors must achieve their desired resolutions within this frequency range. The topic of sensor choice will be discussed in a later section. However, it should be reiterated here that the acceleration of the payload should be measured with a resolution of a fraction of a μg in the crucial frequency range for μg isolation to be successful.

From the diagrams it should be apparent that additional damping may be needed to keep the system stable and prevent the amplification of the acceleration disturbance at the new resonant frequency of the system. If

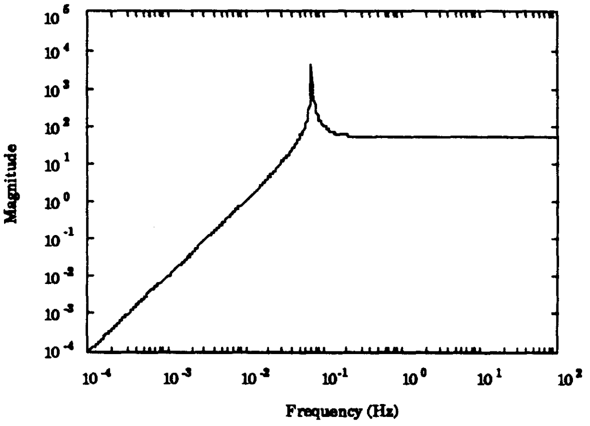

a) Gain feedback

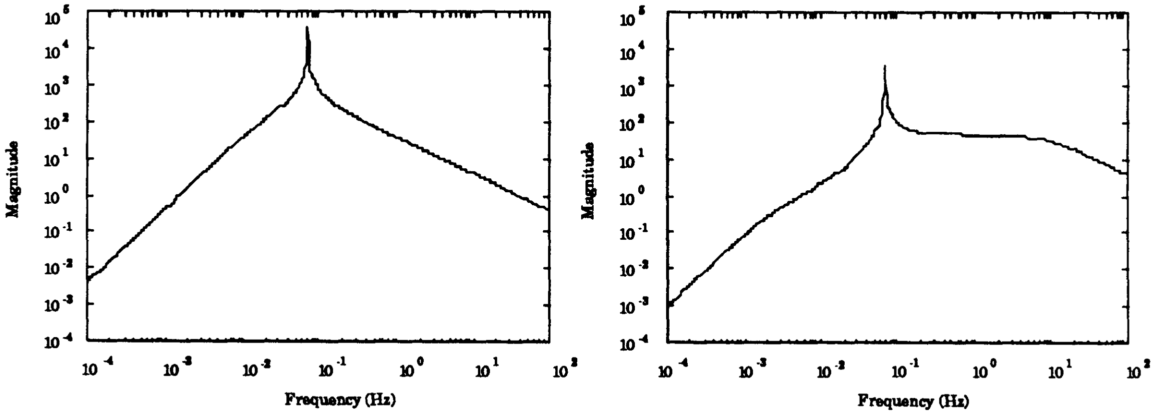

b) Lag compensation c) Lag-lead / lag compensation

Figure 2.11: Loop transfer function of the single degree of freedom spring mass system with different types of compensation: a) gain feedback of acceleration, b) lag compensation, and c) lag-lead / lag compensation.

one looks at the root locus diagram one can see that the addition of a real pole in the feedback loop will add damping (Figure 2.10 b)). At frequencies above the uncompensated resonance, it will satisfy the loop transfer function straight line bode plot guideline that the loop transfer function should crossover the 0 dB line (unity gain) with a slope of ± 1 dB/dB in order to keep the phase margin above 45 degrees (Figure 2.11 b)). In this single DOF model the loop transfer function is $K(s)G(s)/k_m$. If additional damping is desired and the low frequency crossover is to be conditioned by the same single pole compensator, the frequency of this pole must be at least three orders of magnitude lower. This may not be necessary because the first pole seems to have adequate damping. In either case, the compensator is now no longer a constant gain compensator and leads to a much higher loop gain in the control bandwidth. Another choice of compensator is more likely since it may be difficult to maintain the necessary controller gain characteristics and at the same time control undesirable roll-off characteristics. If a lag/lead compensator is chosen to condition the low frequency crossover and provide the necessary damping, high frequency lag compensation can provide a stable high frequency roll-off (Figure 2.11 c)). This compensator also represents a practical implementation of a constant gain controller. Filters either side of the critical control bandwidth attenuate any undesirable signals that could affect performance. The transfer function of this compensator expressed in the Laplace domain is

$$K(s) = K_c \frac{(s + b)}{(s + a)(s + c)} \qquad (2.4.2.7)$$

and the resulting closed loop transfer function, plotted in Figure 2.12, is

$$H(s) = \frac{k_m s^2 + k_m(a + c)s + k_m ac}{m_p s^4 + [m_p(a + c) + K_c]s^3 + (m_p ac + K_c b)s^2 + k_m} \qquad (2.4.2.8)$$

where $a < b < \sqrt{k_m/m_p} < c$.

It is also prudent to note that in order for the system to be properly modeled, the uncertainty in the dynamics of the umbilical cord must be accounted for. In order for this to be achieved in the active mount dynamics, these uncertainties can be buried or overwhelmed by an active mount that is stiffer than the umbilical cord itself. An approximate factor of three relating the mount stiffness to umbilical cord stiffness was determined as sufficient by Jones et al.[4] For a mount with an effective spring stiffness of 7.1 N/m it was experimentally determined that an umbilical cord of 2 to 3 N/m, was acceptable. Since the umbilical cord may be as stiff as 5 N/m, a total mount stiffness of 15 N/m is desirable. To allow for error margin from design to actual stiffness and because it is an order of magnitude above the minimum stiffness of 2 N/m, 20 N/m was chosen as the target mount stiffness.

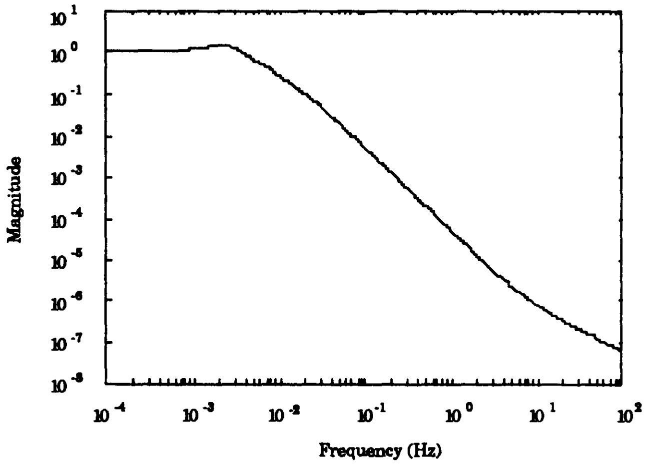

Figure 2.12: Closed loop transfer function with the lag-lead / lag compensator.

2.5 Vibration Isolation Hardware

There are many ways of achieving disturbance attenuation. Various terrestrial methods have been proposed, built, and, in a much smaller number, even applied to space based applications. The two main categories are passive and active. The merits of each type are discussed in Appendix A and the need to use active isolation is confirmed. Piezoelectric actuators are described here in the text and the reasons for choosing polymer piezoelectric material follow.

2.5.1 Piezoelectric Actuators

There are two types of piezoelectric actuators: ceramics and polymers. Both work under the same principle: a physically induced strain produces an electric charge and vice versa. The range of their actuation is constrained by their strain limits. The ceramic is stiff and brittle and thus a hard-mount. The polymer is soft enough to produce a soft spring structure. They have two very different applications.

The ceramic can produce large forces but only at small strain levels. There is a trade-off between actuator size and displacement. Displacements both angular and linear can be controlled to fine increments. When configured in stacks, an object can be positioned accurately over small ranges. This actuator becomes another vernier stage on top of a coarse actuator.[25]

The polymer can provide smaller forces but allow relatively large displacements with small strain when used in a bimorph format. The bimorph format is where two pieces of piezoelectric sheets are attached, one on top of the other. One contracts while the other expands causing the combined actuator to bend much like a bimetallic thermostat. If configured in shelled nodal fashion as conceived at JPL, known as the Softmounted Inertially Reacting PoiNTing System - SIRPNT, it can act as a soft spring for vibration isolation and provide low bandwidth coarse pointing actuation.[14-16] Please refer to Chapter 3, where the PVDF laminated actuator is discussed in detail, to get a more precise description of the principles involved. The high bandwidth fine pointing in this concept is provided by a small CMG located on the payload (Figure 2.13). Force capability of the polymer mount studied has been calculated at 0.44 N axial and 0.74 N lateral with a torque of 0.23 Nm. Deflections of 0.75 m axial, 1.2 m lateral and angles of 87 degrees have also been predicted for sub micro-radian control on a 3 meter long mount. This can also act as an umbilical cord to the orbiting payload as long as the supply lines to the payload do not overwhelm the stiffness of the soft spring mount. The stiffness of the SIRPNT piezoelectric polymer mount is approximately equal to that determined previously as the minimum necessary for soft mounting a 4000 kg payload.

The piezoelectric polymer approach is a method of vibration isolation that seems to be more than capable of fulfilling the requirements of the microgravity vibration isolation problem. It also offers the possibility of doing so with extra desired features. The PVDF actuator can potentially allow for greater displacements than current magnetic mounts and has the added benefit that if the control system fails, there still a high degree of isolation provided by the soft PVDF arc springs. Piezoelectric polymer actuator technology is at a relatively undeveloped stage and is certainly worth more detailed study and an attempted terrestrial demonstration of its capabilities.

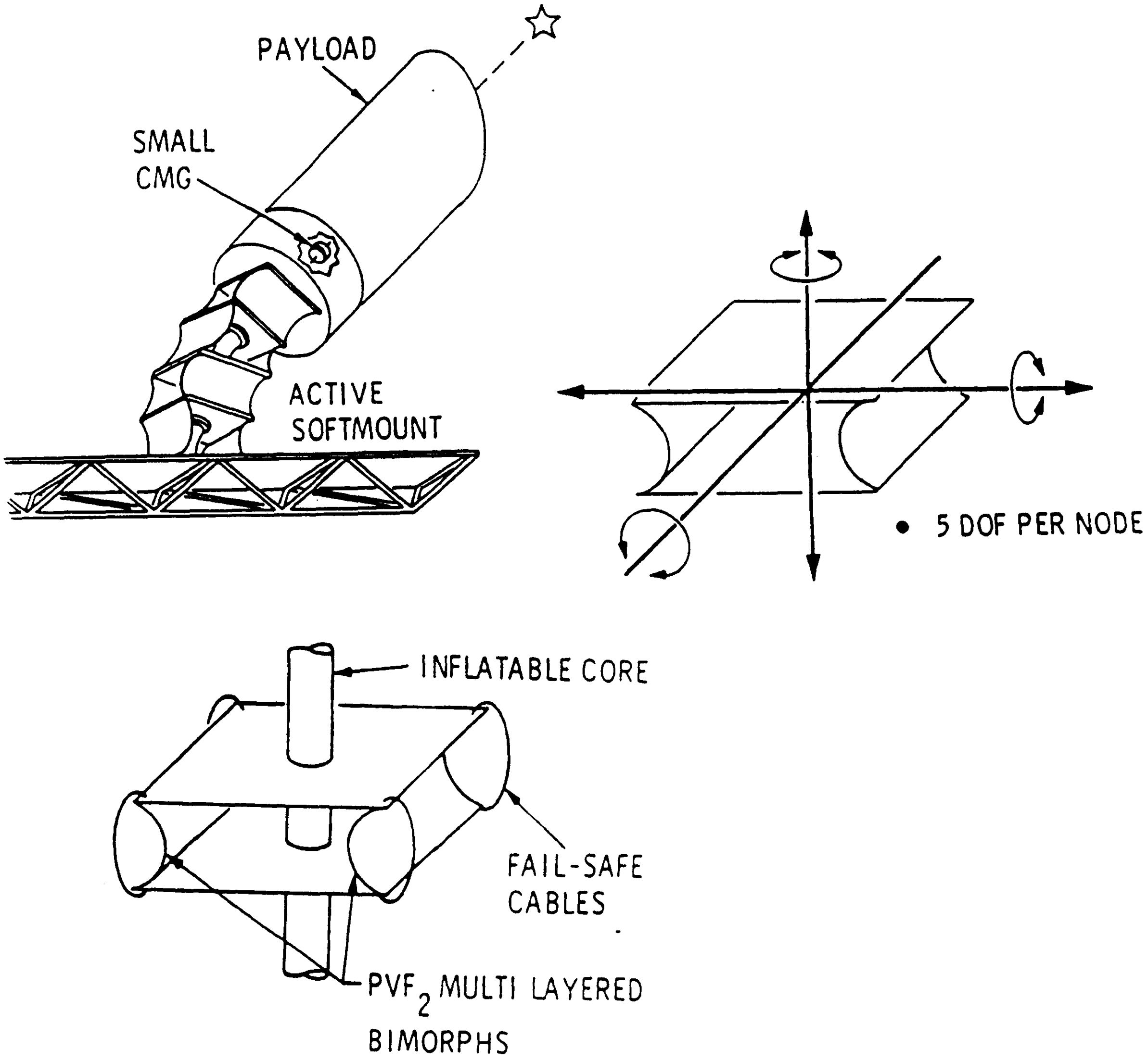

Figure 2.13: SIRPNT polymer piezoelectric design concept

2.6 Summary

This chapter has outlined the physical requirements and limitations of a 100 kg. space based LEO microgravity vibration isolation facility. It also defines the general approach taken toward the design of a workable demonstration. The mount must isolate the payload according to a prescribed basebody acceleration disturbance spectrum shown in Figure 2.6. This isolation specification requires that the mount accommodate a payload travel of at least ± 2.5 mm relative to the basebody. Since the umbilical cord functions of the mount dictate a minimum stiffness for the mount too great for purely passive isolation, 2 - 5 N/m, active control is necessary. A typical regulator approach is taken to the control design and the compensator is essentially that of constant gain feedback of acceleration with a few additions to take into account potential undesirable behavior of the system outside its control bandwidth of 0.01 to 1 Hz.. It must also be taken into account that the umbilical cord part of the mount has uncertain dynamics and, in order for the control approach to work, its uncertainties must be buried by the dynamics of the remainder of the mount, the actuator. This results in a target composite mount stiffness of around 20 N/m. Piezoelectric polymer laminated arc actuators were chosen for development for several reasons: their theoretical ability to perform the aforementioned mission, the possibility of providing a greater range of motion than magnetic mount options, and their ability to provide a fair amount of passive isolation even in the event of a control system failure. There is also the need to perform a physical demonstration of these capabilities as an alternative to magnetic mount technology which has already essentially been proven capable for this the mission (although not yet flown).

Chapter 3

The Piezoelectric Laminated Polymer Film Actuator

3.1 Overview

This chapter will cover the basics of a piezoelectric laminated polymer film arc actuator, from theory to manufacture. The equations describing the dynamics of a piezoelectric arc are derived as well as those for an actuator configuration known as a node. A node consists of two arcs which are placed back-to-back between the two surfaces to be isolated. Various types of arc end mounting conditions and multiple arc configuration options are discussed. The chapter then finishes with a description of the manufacturing procedure for a laminated PVDF film arc. Included in that section are some issues which effect the mount design. This chapter is a basic toolbox for designing a PVDF laminated arc mount.

3.2 Basic Concepts of the Piezoelectric Laminated Polymer Film Arc

A piezoelectric material is one which produces an electric charge when mechanically strained or produces mechanical strain when an electric field is applied across its electrodes.[8] The raw material is comprised of small portions that are electrically polarized in different directions. When a large enough electric field is applied across the material, the polarities are forced to line up. After this polarization, when a voltage less than the depoling voltage is applied across the electrodes in the poling direction, an electric field results ($E=V/t$) and the material will strain. If the material is a thin plate (see Figure 3.1) and the polarization is in the thickness, 3, direction, the major dimension changes will be in the plane of the plate, the 1 or 2 directions. The piezoelectric constant, d_{31} or d_{32} (the first subscript refers to the direction of polarization and the second to the axis of the resulting strain) relates electric field to induced strain. In the case of PVDF, some properties of which are listed in Appendix C, the d_{31} is an order of magnitude greater than the d_{32}. This means that when a voltage is applied through the thickness of the plate most of the noticeable strain will take place in the 1 direction.

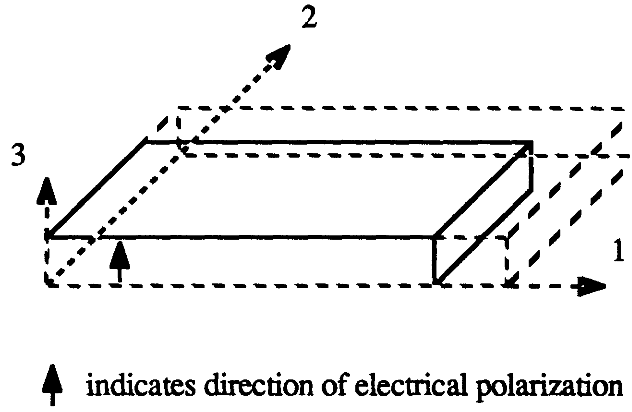

Figure 3.1: Induced strain in a piezoelectric plate due to an applied voltage

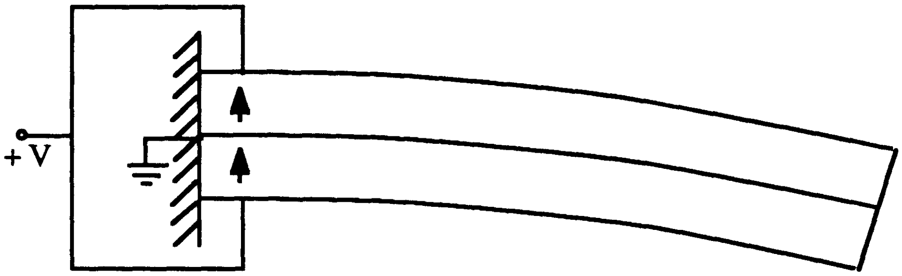

Figure 3.2: Bending of 2 layer laminated piezoelectric sheet due to an applied voltage.

If two plates or sheets are affixed parallel to each other so that they strain in opposite directions when a voltage is applied, the corresponding unit will experience a bending moment and bend much like the way a bimetallic strip bends in response to thermal strains (see Figure 3.2). If the unit is a cantilevered beam with an applied voltage, the bending strain and moment produce a tip displacement.

$$M_p = Ebh_L d_{31} V \tag{3.2.1}$$

$$\delta_x = \frac{3d_{31}L2}{4h_L}V \qquad (3.2.2)$$

M_p is the piezoelectric bending moment, b is the width of the laminate (2 direction), h_L is the layer thickness, E is the Young's Modulus (2 x 10^9 N/m^2), the piezoelectric constant, d_{31}, is 23 x 10^{-12} strain per V/m, V is the applied voltage, L is the length of the beam and δ_x is the tip displacement.

If more than one pair of layers are glued together, a multimorph has been assembled. If they are configured so that all the layers on one side of the neutral axis expand while the others contract, it too will bend (see Figure 3.3). A multimorph is useful because there is a limit to the strength of the electric field that can be applied across a piezoelectric material without it depoling. Consequently, the same electric field can be achieved by applying a smaller voltage across a large number of thinner layers. The resulting moment is

$$M_p = Ebh_L n_B{}^2 d_{31}V \qquad (3.2.3)$$

where n_B is the number of pairs of PVDF layers in the laminate.

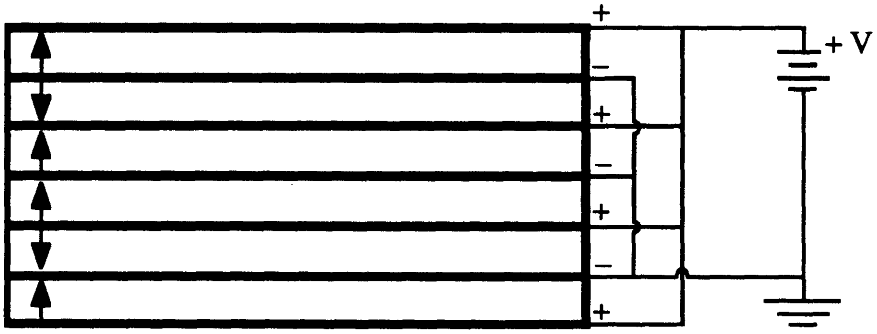

Figure 3.3: Configuration of layer polarity and electrical connections for the bending of a multimorph

When a multimorph is laid up on a mold so that its equilibrium shape is that of an arc, the electrically induced moment will change the radius of curvature (see Figure 3.4 a)). Thus when a voltage is applied to a semicircular piezoelectric laminated arc, the direction of its tip displacement is now approximately in line with the chord drawn between the arc ends. The semicircular arc also acts like a spring when mechanically compressed in this direction. This actuator now resembles an active spring. When two arcs are placed together as shown in Figure 3.4 b), the side to side motion caused by each arc folding or unfolding can be eliminated because the arcs are constrained to move together. If both arcs expand at the same time, the node will either move freely (producing a displacement) or provide a force when the movement is opposed. This is a version of the node developed by Sirlin and Laskin.[15] The dimensions or forces of the node can be commanded so that the isolation specifications are met and the only force between the payload and the basebody is that of the stationkeeping bias force.

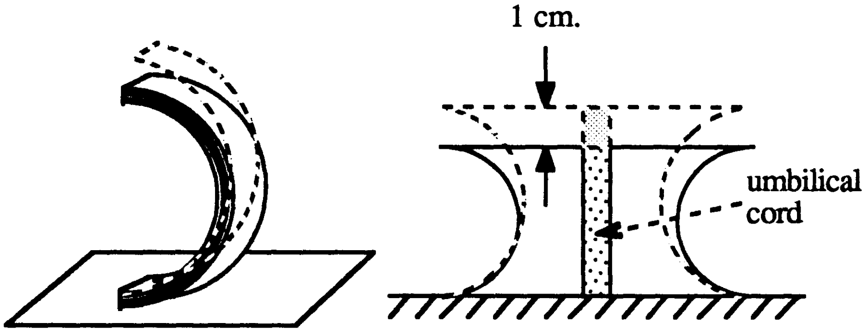

Figure 3.4: The PVDF laminated actuator: a) A laminated piezoelectric arc and b) a piezoelectric node.

3.3 Arc Equations

The method of derivation of the piezoelectric actuator equations in the following sections is that suggested by Sirlin and Laskin.[15] The first section derives the mechanical stiffness of a PVDF film arc and the second derives the equations necessary to determine the actuation capabilities of the piezoelectric film arc. These two sections set up the basic equations necessary to analyze any configuration of semicircular piezoelectric arcs between the payload and the platform. The method used to analyze this type of arc is also directly applicable to actuators of different arc angle or shape. This is not the only way of deriving equations for this use. Another method, one which produces non-linear equations, minimizes the strain energy in a beam with respect to its radius of curvature. It is described in Appendix D. When linearized about its equilibrium point, this method is no more effective than the method developed in this chapter, but gives an order of magnitude check on the characteristics predicted for the arcs. Sirlin and Laskin chose a type of actuator grouping, or configuration, called a node (Figure 3.4 b)). Its stiffness and actuation relations were used as a way of sizing the actuators that would be manufactured for the actual microgravity experiment.

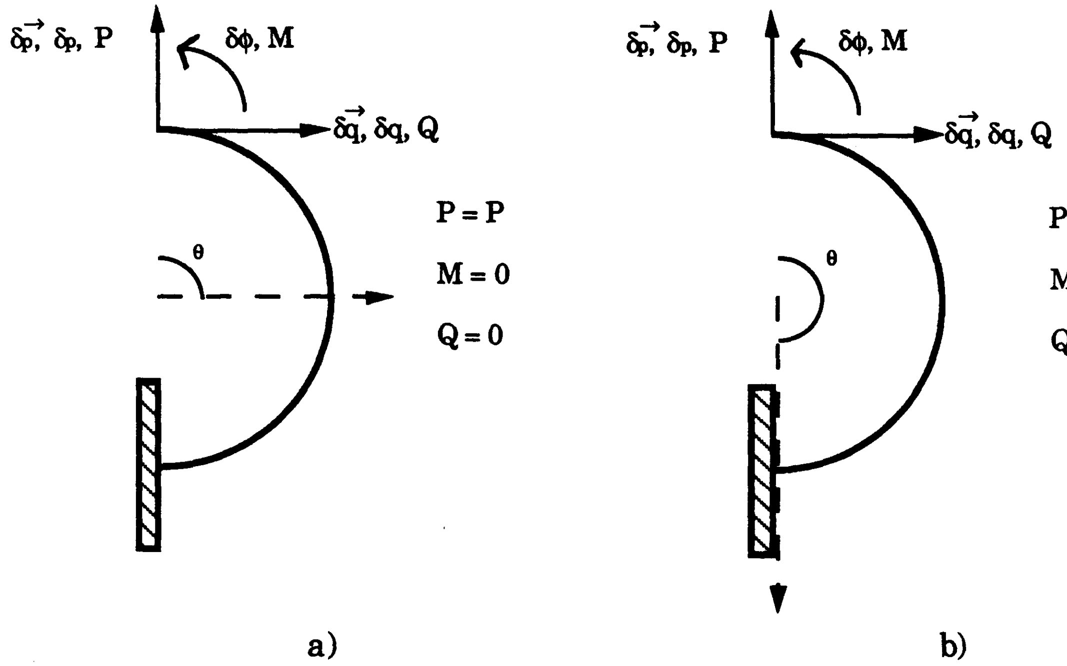

a) b)

Figure 3.5: Diagrams of some types of models for which Castigliano's Theorem is used to determine the tip displacement at the free end of a curved arc. It is clamped at one end and subject to forces at the free end. a) $\vec{\delta_p}$ direction (vertical) force and displacement. b) $\vec{\delta_q}$ direction (horizontal) force and $\vec{\delta_p}$ direction displacement

3.3.1 Mechanical

Since three coordinates (δ_q,δ_p,δ_ϕ) are necessary to describe the planar translation and rotation of the tip of one of these arcs relative to its equilibrium position and there is a force or a torque (Q,P,M) to correspond to each of the coordinate directions, the stiffness or compliance matrix which relates these six variables will have three rows and columns. The elements of this matrix can be derived by using Castigliano's Theorem as suggested by Sirlin and Laskin.[15] Castigliano's Theorem states that "the partial derivative of the total internal strain energy with respect to any external force yields the displacement under the point of application of that force in the direction of the force".[26] When applied to an arc like the one shown in Figure 3.5 a) where one end is clamped and the other end is free to move, the tip displacements mentioned above are directional magnitudes of the displacement vector, $\vec{\delta}_{\mathbf{a}}$, of the free tip of the beam. The components of this vector in the $\vec{\delta}_{\mathbf{q}}$,$\vec{\delta}_{\mathbf{p}}$, and $\vec{\delta}_{\phi}$ directions are contained in the column matrix $\boldsymbol{\delta}_{\mathbf{a}}$, and the components of the forcing vector $\vec{\mathbf{F}}$ are in the column matrix **F**.

$$\boldsymbol{\delta}_{\mathbf{a}} = \left[\ \delta_q \ \ \delta_p \ \ \delta_\phi\ \right]^T \tag{3.3.1.1}$$

$$\mathbf{F} = \left[\ Q \ \ P \ \ M\ \right]^T \tag{3.3.1.2}$$

For an example of how this theorem is applied it is useful to look at the effect a force P has on the displacement in the $\vec{\delta}_{\mathbf{p}}$ direction. Using simple beam theory, the bending moment, M, caused by this force at any point along the beam is

$$M = PR\cos\theta \tag{3.3.1.3}$$

where R is the radius of the arc and θ is the angle that a line drawn radially from the center of the arc to the point on the circumference would make with the horizontal.[26,27] The strain energy, U, in a beam due to bending is

$$U = \int_{0}^{l} \frac{M^2}{2EI} dx \qquad (3.3.1.4)$$

where
l = circumferential length of the arc
dx = incremental circumferential distance
I = the area moment of inertia of a beam cross-section
$= \frac{bh^3}{12}$ for a rectangular cross-section
b = beam width
h = total beam thickness

and the displacement of the tip of the beam in the direction of interest is the partial derivative of the bending energy with respect to the force in that direction.

$$\delta_p = \frac{\partial U}{\partial P} = \frac{\partial}{\partial P} \int_{0}^{l} \frac{M^2}{2EI} dx = \int_{0}^{l} \frac{M \frac{\partial M}{\partial P}}{2EI} dx \qquad (3.3.1.5)$$

The displacement can either be obtained by working out the integral in Eq. 3.3.1.4 and then computing the partial derivative or by determining the integral in Eq. 3.3.1.5 . First, since the moment is expressed in terms of the angle θ, Eqs. 3.3.1.4 and 3.3.1.5 must be transformed to these variables using the conversion $dx = Rd\theta$. This leaves us with

$$U = \int_{-\pi/2}^{+\pi/2} \frac{M^2}{2EI} R d\theta, \quad \text{and} \qquad (3.3.1.6)$$

$$\delta_p = \frac{\partial U}{\partial P} = \frac{\partial}{\partial P}\int_{-\pi/2}^{+\pi/2} \frac{M^2}{2EI} R d\theta = \int_{-\pi/2}^{+\pi/2} \frac{M\frac{\partial M}{\partial P}}{2EI} R d\theta \qquad (3.3.1.7)$$

If Eq. 3.3.1.3 is substituted into Eq. 3.3.1.6, the bending energy becomes

$$U = \frac{R^3}{2EI}\int_{-\pi/2}^{+\pi/2} P^2 \cos^2\theta d\theta \qquad (3.3.1.8)$$

which upon calculation is

$$U = \frac{\pi}{4}\frac{R^3}{EI}P^2 \qquad (3.3.1.9)$$

This results in the displacement-force relation below, when its partial derivative with respect to the force in the displacement direction is taken. It is also the same result that would have been calculated if Eq. 3.3.1.7 had been worked on directly.

$$\delta_p = \frac{\partial U}{\partial P} = \frac{\pi}{2}\frac{R^3}{EI}P \qquad (3.3.1.10)$$

Forces and torques can also produce rotational and translational displacements in degrees of freedom other than the one in which the force or torque is applied. This will now be explored for a displacement in the same $\vec{\delta_p}$ direction but with a force imposed in the $\vec{\delta_q}$ direction. For this case a slightly different definition of the angle θ is used as shown in Figure 3.5 b). Since the displacement in question is in the $\vec{\delta_p}$ direction, the moment equation must have a term with P in it so that the partial derivative $\frac{\partial U}{\partial P}$ is non-zero. A fictional force P is added into the moment equation (Eq.

3.3.1.11) and carried through the math. Its true value of zero is substituted back in at the end but a non-zero displacement results. The moment relation is

$$M = PR\sin\theta + QR(1 + \cos\theta) \qquad (3.3.1.11)$$

When this is substituted into Eq. 3.3.1.4 and the $dx = Rd\theta$ substitution is made, the following strain energy and displacement result.

$$U = \frac{R^3}{2EI}\int_0^\pi (2PQ\sin\theta + P^2\sin^2\theta + Q^2(1 + \cos\theta)^2)d\theta \qquad (3.3.1.12)$$

$$U = \frac{R^3}{EI}(2PQ + \frac{\pi}{4}P2 + \frac{3\pi}{4}) \qquad (3.3.1.13)$$

$$\delta_p = \frac{2R^3}{EI}Q \qquad (3.3.1.14)$$

A less complicated integral often results when the the partial derivative is moved inside the integral to provide a direct calculation of the displacement-force relation. The integral for the relation corresponding to this example is

$$\delta_p = \int_0^\pi \frac{M\frac{\partial M}{\partial P}}{2EI}Rd\theta = \frac{R^3}{EI}\int_0^\pi (P\sin^2\theta + Q(1 + \cos\theta)\sin\theta)d\theta \qquad (3.3.1.15)$$

The remainder of the matrix entries are calculated in the same way remembering to take the partial derivatives (∂P, ∂Q, or $\partial\phi$) with respect to the direction of the displacement. The remaining individual equations that are incorporated into the matrix equation are

$$dp = \frac{-2R2}{EI} M \qquad (3.3.1.16)$$

$$\delta_q = \frac{2R^3}{EI} P \qquad (3.3.1.17)$$

$$\delta_q = \frac{3\pi}{2} \frac{R^3}{EI} Q \qquad (3.3.1.18)$$

$$\delta_q = \frac{-2R^2}{EI} M \qquad (3.3.1.18)$$

$$\delta_\phi = \frac{-2R^3}{EI} P \qquad (3.3.1.20)$$

$$\delta_\phi = \frac{-\pi R^2}{EI} Q \qquad (3.3.1.21)$$

$$\delta_\phi = \frac{\pi R}{EI} M \qquad (3.3.1.22)$$

The equations are restated in matrix format in section 3.4 Node Equations.

3.3.2 Piezoelectric/Electrical

The same type of analysis used for mechanical strain is used for the electrically induced strain. The moment is expressed in Eq 3.2.3 and can be substituted into equations of the form of Eq. 3.3.1.7 along with the moment produced by a fictional force in the $\vec{\delta_q}$,$\vec{\delta_p}$, or $\vec{\delta_\phi}$ directions depending on which displacement is being analyzed. Once again, one should take the partial derivative with respect to the fictional force in the displacement direction as done in Eq. 3.3.1.7 for the force in ∂P in the $\vec{\delta_p}$ direction. The resulting equations are

$$\delta_p = \frac{2R^2}{EI} M_p \qquad (3.3.2.1)$$

$$\delta_q = \frac{\pi R^2}{EI} M_p \qquad (3.3.2.2)$$

$$\delta_\phi = -\frac{\pi R}{EI} M_p \qquad (3.3.2.3)$$

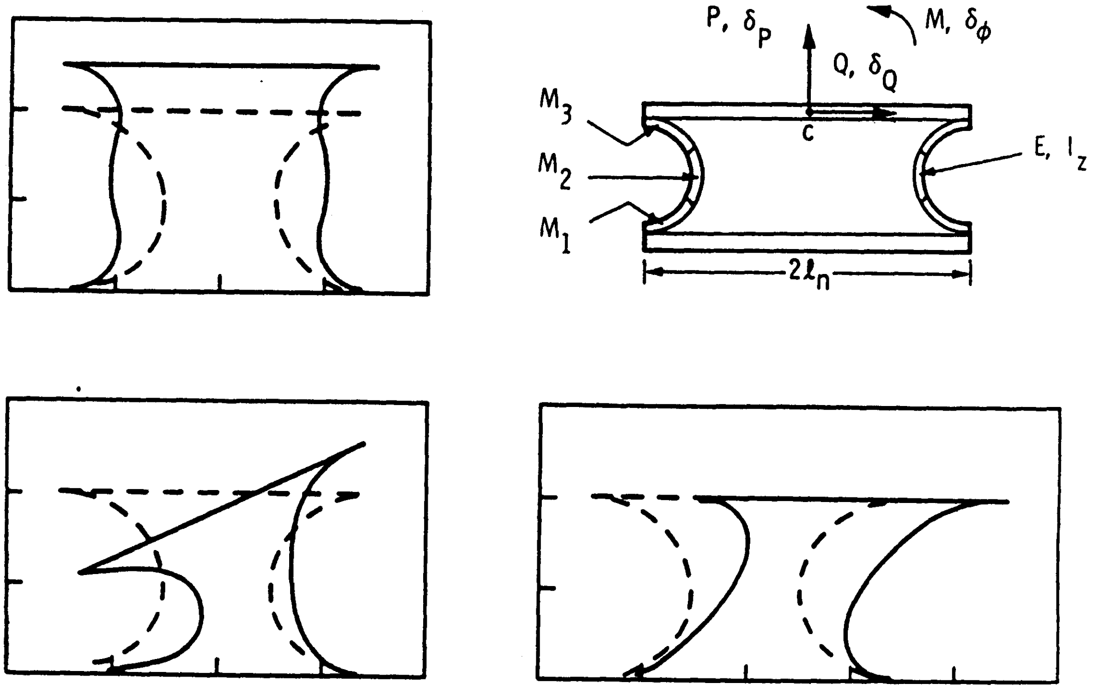

Figure 3.6: An actuator grouping called a node consisting of two piezoelectric arcs back to back. The metallization on each arc is divided into three sections to allow pure side to side and rotational motion as well as vertical

3.4 Node Equations

Sirlin and Laskin developed a model for their arc and node and it is summarized below with modifications and corrections necessary for proper analysis of the arcs used in this thesis.[15] Their arcs were electrically segmented by etching away two strips of metallization on each side of each layer. This allows the user to command the bending moment in three equally sized sections. With this added capability, a single node can be commanded to provide the purely vertical, horizontal, or rotational forcing or displacement shown in Figure 3.6. It should be noted that although the arcs addressed in this document are not segmented, this possibility does exist and may be useful in the future.

The actuation constant matrix **B** becomes a column matrix when segmentation is not used and replaces the square one introduced by Sirlin and Laskin.[15] One should make note that Sirlin and Laskin appear to have reversed the δ_p and δ_q entries for the piezoelectrically induced displacements and forces. If their equations are simplified so that there is no longer segmentation, the first two entries in the **B** matrix would be the reverse of those calculated in the previous section and presented below. The equations resulting from the above analysis for a node of two back-to-back arcs are expressed in a notation nearly identical to Sirlin and Laskin is shown below. This system now resembles a wall-spring-mass like the one expressed in the single degree of freedom model discussed in chapter 2. The payload or mass to be isolated sits on top of the active spring which is the PVDF two arc node.

For arc a:

$$\delta_a = \mathbf{A}_a \mathbf{F}_a + \mathbf{B}_a u_a \tag{3.4.1}$$

where $\delta_a = [\delta_{q_a}\ \delta_{p_a}\ \delta_{\phi_a}]^T$, $\quad \mathbf{F}_a = [Q_a\ P_a\ M_a]^T$, $\quad u_a = M_{c_a}$,

$$\mathbf{A}_a = \frac{R}{EI_z}\begin{bmatrix} \frac{3\pi R^2}{2} & 2R^2 & -\pi R \\ 2R^2 & \frac{\pi R^2}{2} & -2R \\ -\pi R & -2R & \pi \end{bmatrix}, \qquad \mathbf{B}_a = \frac{R}{EI_z}\begin{bmatrix} \pi R \\ 2R \\ -\pi \end{bmatrix},$$

$$u_a = M_c, \qquad I_z = \frac{bh^3}{12}, \text{ and } \qquad h = 2nBhL = \begin{matrix}\text{arc}\\ \text{thickness.}\end{matrix}$$

For a node composed of two arcs a and b, the relations must be made with respect to a payload reference point c. In this case it is a point equidistant between the mounting points of arcs a and b to the payload and represents its anticipated center of gravity. The relations below are for this reference point c.

$$\mathbf{F}_c = [Q_c \, P_c \, M_c]^T = \mathbf{K}_n \delta_c + \mathbf{B}_a \mathbf{u} \tag{3.4.2}$$

where,

$$\begin{aligned} \mathbf{K}_n &= \mathbf{G}_a{}^T \mathbf{K}_a \mathbf{G}_a + \mathbf{G}_b{}^T \mathbf{Q} \mathbf{K}_a \mathbf{Q} \mathbf{G}_b \\ \mathbf{K}_a &= \mathbf{A}\mathrm{a}^{-1}, \quad \mathbf{u} = [u_a \; u_b]^T, \\ \mathbf{B}_n &= -[\mathbf{G}_a{}^T \mathbf{K}_a \mathbf{B}_a \;\; \mathbf{G}_b{}^T \mathbf{Q} \mathbf{K}_a \mathbf{Q} \mathbf{B}_b], \end{aligned}$$

$$\mathbf{Q} = \begin{bmatrix} 1 & 0 & 0 \\ 0 & -1 & 0 \\ 0 & 0 & 1 \end{bmatrix}, \quad \mathbf{G}_a = \begin{bmatrix} 1 & 0 & 0 \\ 0 & 1 & -l_n \\ 0 & 0 & 1 \end{bmatrix}, \quad \mathbf{G}_b = \begin{bmatrix} 1 & 0 & 0 \\ 0 & 1 & l_n \\ 0 & 0 & 1 \end{bmatrix},$$

and, l_n = distance between the umbilical cord and an arc clamping point.

This is derived by taking each arc to be clamped at both ends, one to the wall of the basebody and the other to the payload casing, and transforming the relations for arc a using the transformation matrix **Q** to obtain the relations for arc b. The transformation matrices $\mathbf{G}_a$ and $\mathbf{G}_b$ transform the forces and moments so that they are expressed in terms of their influence at the reference point c. Effective spring and actuation constants for this mount can be calculated.

With a general method available to analyze piezoelectric laminated arcs (the use of Castigliano's Theorem and the concept of the node), a mount design composed of a configuration of many piezoelectric film arcs can be attempted. Other types, designs or shapes of piezoelectric film arcs may also use this method of analysis. Whatever design is chosen, it must adhere to the requirements derived in Chapter 2. It should also be noted that when an arc is connected to any surface mounting device the location of the connection (the mounting point) should be displaced some distance away from each surface so that when the arc is in compression it touches only the mounting assembly and not the surface it is attached to. As can be seen in Figure 3.7, this type of contact will avoid adverse effects on the validity of the above modelling.

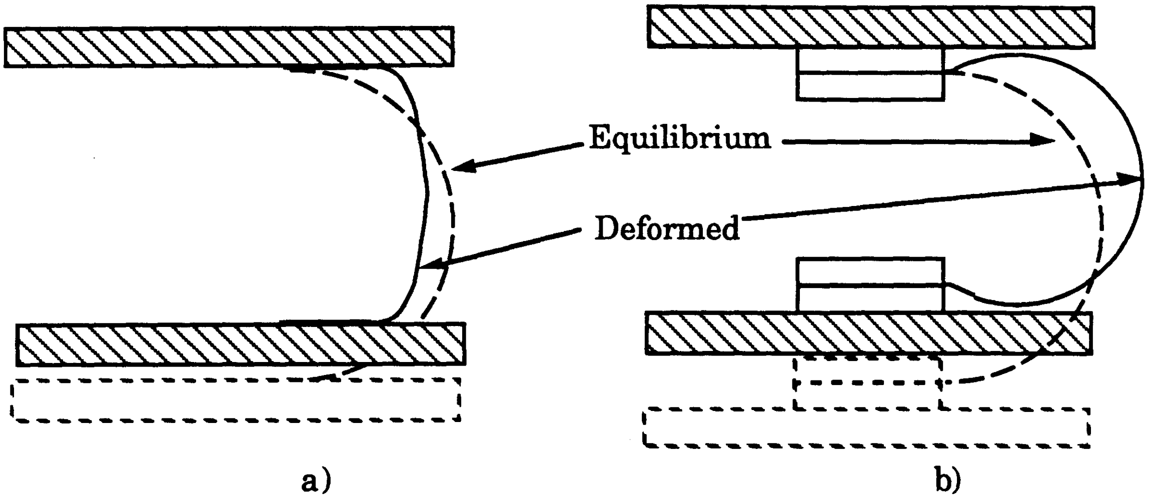

Figure 3.7: Solution to avoiding the undesirable effect of not giving enough space between the point of contact of the arc with the mounting assembly and the surface to which the mounting assembly is attached: a) the undesirable effect, and b) the solution.

3.5 Multi-Axis Concepts

Now that an arc model for a single axis problem has been formulated, it should be noted that a flight qualified microgravity isolation mount would have to work in 6 degrees of freedom (3 translation and 3 rotation). With only two electrical inputs for each node only two degrees of freedom of the payload can be controlled at one time. If the two arcs are commanded to expand or contract in unison the *vertical* ,$\vec{\delta_p}$, or can be controlled. If the two arcs are given opposing commands the *horizontal*, $\vec{\delta_q}$, and rotational, $\vec{\delta_\phi}$, motions are excited. When the arc expands or contracts there is horizontal, vertical and rotational motion of the tip. If the two matched back-to-back arcs are given the same signal the horizontal and rotational factors subtract. When the two arcs are given the opposite signal these two degrees of freedom add. In order to control all three degrees of freedom at once, at least one more arc must be added. In order to keep the motion in the horizontal direction similar to that of the vertical, one can give the payload a more realistic representation in the form of a box and add another node on an adjacent side as shown in Figure 3.8. The local vertical motions of this mode control the horizontal motions of the system as a whole. The differential commands of both of the nodes can be used to control the rotational motion. This type of configuration will control the motion of a payload in one plane. One must also remember to transform the forces and moments described at the point equidistant on the line between the two node arcs to that of the desired payload reference point. Because it may not be readily apparent, it should be pointed out that this transformation can introduce a moment at this new location due to the change in moment arm. If there is no moment acting about the old reference point, the force will then produce a moment about the new point.

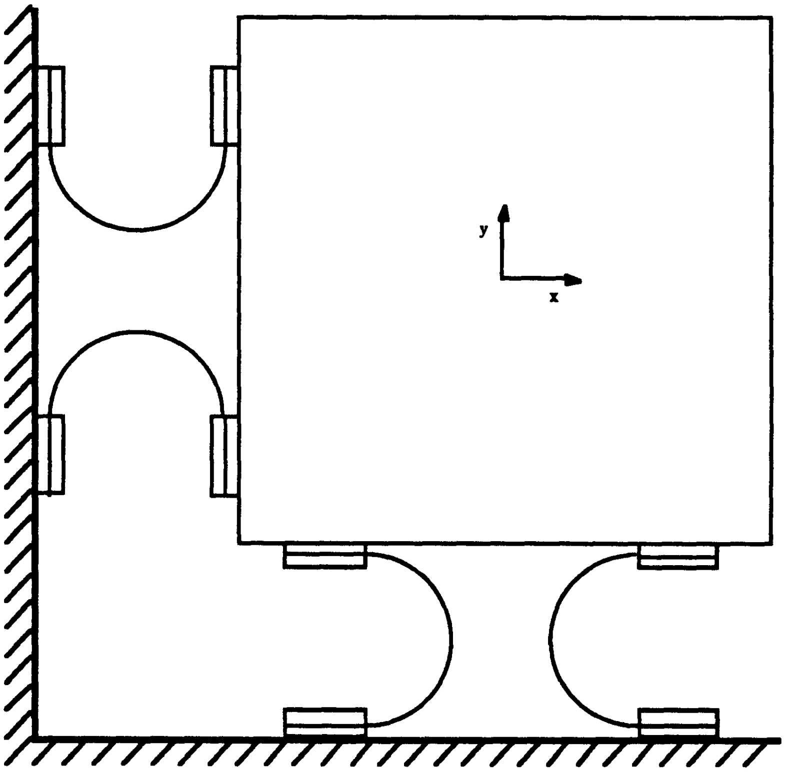

Figure 3.8: Three degree of freedom, two node PVDF arc configuration to control a box (square) payload.

In a six DOF space based application, the actuators will have to be soft in the third translational axis as well (out of the plane). Although the arcs mentioned above are too stiff in this third out-of-the-paper axis, two nodes can be stacked on top of each other to produce the desired results. If the second node is rotated by 90 degrees about the $\vec{\delta_p}$ axis, its $\vec{\delta_q}$ axis is now in the out-of-the-paper axis and its the stiffness in this direction is now sufficiently soft. This is also another step in the direction of the SIRPNT approach of Sirlin and Laskin.[15] Another option is to further alter the shape of the actuator so that the actuator itself is sufficiently soft in all three axes without the addition of another node. In this case the actuator arcs could be similar to the arcs in the previous section except that they would be tapered at each end. An actual analysis has not been conducted for this type of actuator and is only offered as a possible solution. In any case, there must be at least one arc per degree of freedom to be controlled. One way to configure these arcs for a six DOF mount is evident when the payload or mass to be isolated is shaped like a box. It is convenient to place a node on at least three of the sides of the box. The translational motions can be controlled by the arcs in each node working in unison and the rotations by the arcs working 180 degrees out of phase. If the payload is not the shape of a box, the mount can either employ a different and quite possibly more complicated dynamic analysis or mounting extensions can be provided to simulate the box conditions so that the type of analysis performed in this document is sufficient.

A six DOF experiment is very difficult to perform in the one g environment of the Earth's surface and is not necessary for a proof of concept of the PVDF film actuator. In fact, this type of experiment would unnecessarily complicate the problem of developing the type of technology necessary to implement this type of solution. A three DOF experiment is a more reasonable approach for attempting to see how this concept fares. One axis experiments can be attempted and the issues of what happens when applied to more degrees of freedom can be addressed. Multi-axis isolation can also be performed. The experimental set up described later was devised with nonsegmented nodes intended to control the motion within a single plane, two translation directions and one rotation direction. A minimum of two nodes, four arcs, are needed to perform the planar 3 DOF control experiment. The following PVDF actuator was designed using a single modified Sirlin and Laskin node (no segmentation) and is described in Table 3.1.

Table 3.1: Specifications of a clamped node using Sirlin's method

Characteristic	Value
layer thickness	30 μm
glue layer thickness	2 μm
number of layers	6
total thickness	192 μm
width	0.05 m
metallized width	0.047 m
radius	0.04 m
number of arcs	4
maximum voltage	840 V
force (@ V=800)	0.2 N
displacement (V=800)	0.011 m
mechanical spring stiffness (including umbilical cord)	20 N/m

3.6 Actuator Boundary/Mounting Conditions

Until now, a clamped end condition has been the only type of boundary or end condition discussed for actuator arc mounting. A greater range of motion can be produced for a given voltage on the same arc if the end of an arc is allowed to rotate. The arc is less restricted and stays closer to a circular arc shape over a greater range of motion. When the arc is clamped, there is a lot of bending in a particular direction at its root and similar bending in the opposite direction in the arc middle. The shape of the arc quickly deviates far enough from being a circular arc so that the equations discussed above are no longer valid. This deviation stiffens the arc enough so that a node will only produce displacements one quarter of those predicted (see Chapter 5, Experimental Results). When the arc end is hinged, the additional concentrated bending diminishes. These hinges also have an added bonus of simplifying the mathematics to a certain degree. There is no longer a moment applied at the hinge and the tip angle is irrelevant except perhaps as an indication of where the actuator arc is within the assumed linear range of its operation point. There are several ways of implementing this type of hinge. The types investigated in this document are shown in Figure 3.9.

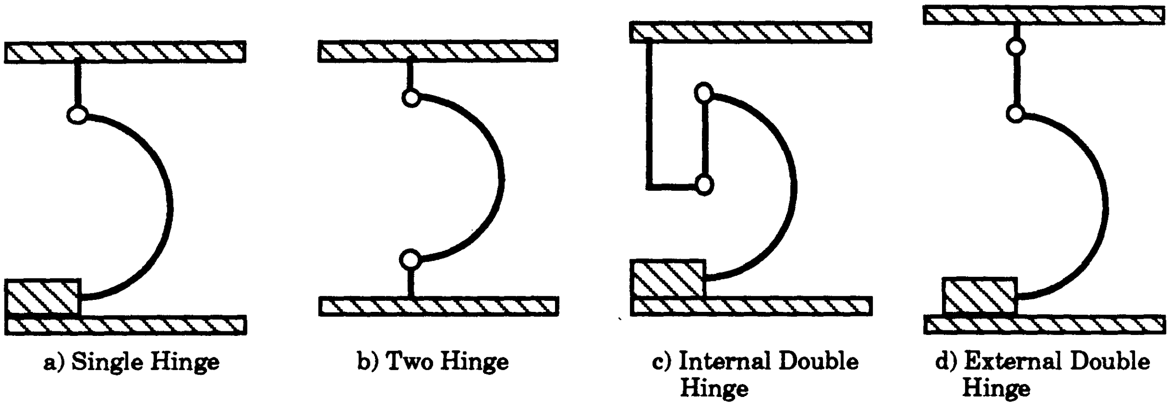
a) Single Hinge
b) Two Hinge
c) Internal Double Hinge
d) External Double Hinge

Figure 3.9: Four types of actuator mounting configurations using hinged end conditions: a) clamped-hinged (single hinge), b) hinged-hinged (two hinge), c) clamped-double hinged type I (internal double hinge), and d) clamped-double hinged type II (external double hinge).

The first type of hinged mounting configuration discussed in this document is that where one of the clamped end conditions is replaced by a hinged one, the single hinge arc as in Figure 3.9 a). It simplifies the equations somewhat for the reasons discussed in the previous paragraph. If the actuator force is desired at the end that is hinged, the 3 x 3 compliance matrix presented earlier in the chapter (Eq. 3.4.1) becomes a 2 x 2 matrix by eliminating the entries that are related to the tip angle and applied moment. The rotational motion is still controlled by differentially applied voltages to the two arcs and the horizontal motion is still excited and uncontrollable without another actuator. In order to control this horizontal motion, a second node can be attached on one of the payload's adjacent sides as shown in Figure 3.8 for the clamped only mounting conditions described earlier in the chapter. The node equations that differ are shown below.

$$\delta a = [\delta qa\ \delta pa]^T, \qquad \mathbf{F}a = [Qa\ Pa]^T$$

$$\mathbf{A}_a = \frac{R}{EIz}\begin{bmatrix} \frac{3\pi R^2}{2} & 2R^2 \\ 2R^2 & \frac{\pi R^2}{2} \end{bmatrix}, \qquad \mathbf{B}_a = \frac{R}{EIz}\begin{bmatrix} 2R \\ \pi R \end{bmatrix}, \tag{3.6.1}$$

$$\mathbf{Q} = \begin{bmatrix} 1 & 0 \\ 0 & -1 \end{bmatrix}, \qquad \mathbf{G}_a = \begin{bmatrix} 1 & 0 & 0 \\ 0 & 1 & -l_n \end{bmatrix}, \qquad \mathbf{G}_b = \begin{bmatrix} 1 & 0 & 0 \\ 0 & 1 & l_n \end{bmatrix},$$

The above configuration still suffers from concentrated root bending at the mounting point on the rigid wall. The next logical step is to place hinges at both ends. This is the two hinge arc and is shown in Figure 3.9 b) and also in a node format in Figure 3.10. This also simplifies the mathematics even further. Both arc and node have negligible lateral stiffness thus eliminating the need to analyze the forces and displacements in this direction. The compliance matrix for a single arc relative to its tip motion is reduced to a single scalar. This is the first compliance derived in section 3.3 (Eq. 3.3.1.10). With the payload mass end of the node/spring free to move side to side another node is needed in this axis to control this motion. Notice in Figure 3.10 that in the differential excitation mode, there is horizontal motion anywhere on the payload not on the point along a line between the mounting locations of the two arcs and equidistant from them. Physically, this method suffers from the challenge of constructing a zero torsional stiffness electrical connection across the base hinge that is capable of delivering 800 Volts to the actuator. Another challenge is constructing a reliable electrical connection to each arc layer so that the combined mass and inertia is small enough to have negligible effects on the internal dynamics of the actuator. It is not desirable for it to have any internal dynamics noticeable in the control bandwidth of 0.01 to 5 Hz. as they would then have to be included in the control problem model. The first internal mode of each of these arcs was estimated by calculating the vibrational frequencies of standard beams and found to be satisfactory. This result has been experimentally verified.

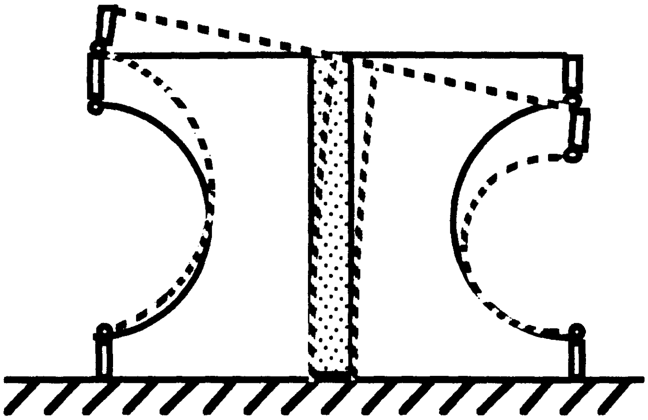

Figure 3.10: A node comprised of arcs mounted by hinges at each end with the arcs given opposite commands.

The characteristics of the two hinge actuator arc can be reproduced by placing a double hinge at the payload side of the arc with a link between the two hinges as shown in Figure 3.9 c) and d). This configuration achieves the single-dimension-stiffness-only by allowing the tip of the arc to move laterally relatively freely. Any forces transmitted to the payload in the lateral direction would be swamped by those of a second node attached on an adjacent side. One issue that should not be ignored is that the internal vibration mode of this arc can be approximated by looking at the vibrational frequencies of a clamped-free beam. This is what turned out to be the downfall of the deployment this type of actuator configuration in the experiment described in the next chapter. The first internal mode of the actuator of the arc chosen for manufacture was inside the control bandwidth.

The actuator configurations discussed here are by no means the only possible solutions. The actuators need not even be in the shape of an arc. The possibility of hinging the end of a beam, arc, or any other shaped actuator allows room for many creative ideas. The ones discussed here are those which were the most developed at the time of the finalization of the experimental design.

3.7 Circular Arc Length Actuators of Angles Other Than 180 Degrees

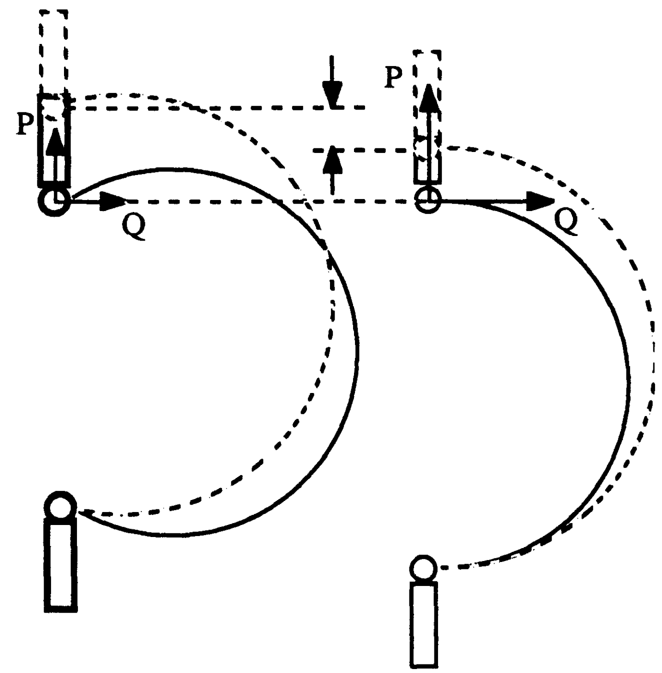

Figure 3.11: Displacements of hinged circular arcs. Arcs with arc angles of more than 180 degrees can move further.

This type of actuator has not been extensively tested but offers yet another option of a physical parameter that can be varied to obtain the appropriate actuator. If the arc angle is greater than 180 degrees, the range of motion is increased over the 180 degree arc (Figure 3.11). The equations used in the analysis of this physical variation also proved a useful starting point for the equations necessary for the gross static verification of the actuator properties (see Chapter 5, Experimental Results).

The equations for this greater angle arc are derived once again using Castigliano's Theorem for a two hinge mounting configuration.

$$P = \frac{EI}{R^3[\psi(\frac{1}{2} + \cos^2\frac{\psi}{2}) + \frac{\sin\psi}{2} + 4\cos\frac{\psi}{2}(1 - \sin\frac{\psi}{2})]}\delta_P \qquad (3.7.1)$$

where ψ is the arc angle of the arclength of the circular arc when at its equilibrium position. Table 3.2 lists the characteristics of an arc of the same width, thickness, and number of layers as the fully clamped node in Table 3.1. Notice the greater force and displacement capability.

Table 3.2: Specifications of a two arc node with hinged end connections.

Characteristic	Value
PVDF layer thickness	30 μm
glue layer thickness	2 μm
number of layers	6
total thickness	192 μm
width	0.05 m
metallized width	0.047 m
radius	0.0254 m
number of arcs	4
maximum voltage	840 V
maximum force (V=800, δ_p= 0)	0.5 N
maximum displacement (V=800)	0.023 m
Ψ (arc angle)	$3\pi/2$
mechanical stiffness (including umbilical cord)	20 N/m

3.8 Manufacturing Procedure

Once the actuator dimensions have been determined, hardware may be manufactured. The Pennwalt Corporation is the supplier of the Polyvinylidene Difluoride (PVDF) film and produces it in sheets or rolls 9 μm, 28 μm, 52 μm, and 110 μm thick with a thin layer of metallization already applied to both sides. The 3-axis polarity and 1-axis directions are marked on the film when it is delivered. Each actuator layer is cut making sure that the 1-axis direction is along the length of the arc layer (the desired strain direction) and that the 3-axis polarity direction is marked. If the actuator is to be clamped at an end it should be cut a little longer than the active actuator dimensions so that there is extra material for the clamping and lead attachment. At the high voltages required for an effective PVDF actuator, up to 30 Volts (AC)/μm of actuator thickness or 840 Volts for 28 μm film, there is just as a large potential difference between it and any grounded surface. This large potential can easily cause an arcing of electricity through or around any material, including air, separating the two. This can result in the melting or burning of a hole in the PVDF layers and usually renders the actuator useless or difficult to repair. Arcing around the actuator edges can be curtailed if the borders of each sheet have 1 or 2 mm of the metallization etched away from the edge.[28] This problem is more readily seen if one visualizes layers placed on top of each other with the edges not exactly lined up as shown in Figure 3.12. The etching is accomplished by using a standard circuit board etchant dependent on what material is used for the metallized surface on the PVDF layer. Archer brand ferric chloride was used here for the less than 1 μm thick sputtered nickel aluminum metallization.

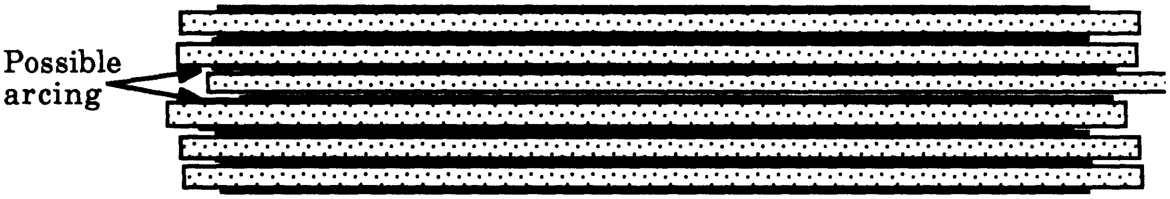

Figure 3.12: Illustration showing how a slight mis-alignment of the layer edges necessitates a 1 to 2 mm border on each PVDF layer with the metallization etched off.

The arc is glued together while on a cylindrical form. The first layer is taped down by its edges onto this mold and wiped free of contaminants. Contaminants such at oils from the human hand or any grease can disrupt the integrity of the glue layer; so it is recommended that plastic surgical gloves be used during the lay up procedure. Also recommended is the use of degreaser and ethanol for removing these substances. Small particles must also be removed from the surface of the film for the same reasons as above and, because the particles that are thicker than the glue layer, will leave an impression which shows through on the surface of the actuator.

This will probably result in excessive additional stress and strain in the vicinity of the particle and may fatigue the film and lead to the arcing of electricity at these flaws. It is recommended to perform the whole procedure inside a ventilated laboratory hood to keep the presence of these particles to a minimum. The same should be done to the bottom of the layer to be affixed on top of the incomplete arc resting on the mold. To get a thin glue layer a two part epoxy is used. Hardener is applied to one side and resin to the other. The surfaces are then wiped so that only a thin film remains before they are pressed together. Care should be taken to make sure that any foreign matter is removed and that any air bubbles are forced out to the edge. This top layer should then be taped down so that it remains in place while subsequent layers are added and the epoxy is not yet cured. The process must be repeated until the whole laminate is in place. When the curing time is completed, the arc can be released from the jig. The adhesive used was a methacrylate epoxy called 5 Minute Epoxy, a product of the Devcon Corporation. Best results were observed when the actuator was left to dry overnight. At the time of the writing of this document the average adhesive thickness achieved is as low as 2 μm per glue layer, determined by measuring the thickness of a whole actuator before and after its lay up. The achievement of producing this thin a layer is due purely to becoming more proficient at the glueing technique. Original attempts produced glue layers that were 15 μm thick. Thinner glue layers can probably be obtained by using a less viscous epoxy with a longer cure time. RBC 3215 epoxy is recommended by the Pennwalt Corporation, manufacturer of the PVDF film.

Now that the laminate is complete it should be electrically hooked up to the driving amplifiers. Initial attempts using conductive epoxy or electrical tape to affix the leads were successful; but after a period of time the electrical arcing mentioned earlier in this section occurred. This was usually a result of arcing near the outer edges of the lead and its mechanical bond or at gaps in the metallization or conductive epoxy caused by fatigue, stress concentration, or improper manufacture. In order to avoid long term fatigue in the metallization near the lead area, the following electrical connection method is suggested.[29] Copper tape with conductive adhesive should be attached to the lead area and then the resulting relatively jagged lead attachment assembly and the surrounding surface should be smoothed over with the application of silver ink. In addition to helping the fatigue problem, this prevents any electrical arcing from occurring around the edges of the copper tape stripping away or burning a hole through the metallization. Soldering should not be attempted on PVDF film because the temperatures involved will degrade the piezoelectric properties of the polymer. Fortunately, any wire can be soldered to the copper tape BEFORE it is affixed to the PVDF. All mechanical/electrical connections should be enhanced by the use of silver ink.

3.9 Corrections Due to Glue Layer and Etching

The above analysis, although good for general design purposes, does not include corrections for a finite glue layer thickness or for reduced active piezoelectric area due to etching around the edges of each layer. Reductions in performance are inevitable. Since the modulus of elasticity of the methacrylate epoxy is of the same order of magnitude as that of the PVDF (2 GPa), the total thickness that is measured, or predicted thickness based on an anticipated glue layer thickness, h_G, is usually sufficient for use with the PVDF modulus as the modulus for both. The thickness used for determining the moment of inertia of the cross-section of the actuator is now

$$h = 2n_B h_L + (2n_B - 1)h_G \tag{3.9.1}$$

If a more accurate moment of inertia is needed an area weighted moment of inertia can be calculated.

The actuator width that should be used for the electrically controlled piezoelectric properties is that of the metallization width, b_m. This should be used in place of the total actuator width, b, as shown in Eq. 3.2.3. Corrections to this induced moment should also be made for the thickness of the glue layer. Although the glue layer stiffens up the mechanical properties, it makes up for some of this difference by shifting the moment arm of each layer further out from the neutral axis. This results in an increase in moment as shown below.

$$M_c = Eb_m(h_L + h_G)d_{31}V \tag{3.9.2}$$

The main effect will be to reduce the displacement capability of the arc because the glue layer is not active.

3.10 Summary

This chapter contains the necessary tools for designing a piezoelectric PVDF laminated film actuator arc. These tools are used when designing any actuator configuration. The actuator configuration used for the three degree of freedom experiment/mount in this thesis is described in the following chapter.

Chapter 4

Experimental Issues and Design

4.1 Overview

This chapter describes the specifics of the three degree of freedom (DOF) experiment performed in the laboratory. The first section talks about the actual experimental hardware. This includes the reasons for choosing critical pieces of equipment and for choosing specific actuator mounting and location configurations. Once this is complete, the equations of motion are derived and the basic characteristics of the system are calculated for use as a guideline for the expected experimental performance.

4.2 Three-Axis Laboratory Demonstration

As stated in the previous chapter, the demonstration vehicle for the use of piezoelectric laminated film actuators for microgravity vibration isolation is that of a planar three DOF experiment. This motion is limited to that of a single plane because any plane that is not the local earth surface horizontal will have a certain fraction of full earth gravity as a bias acceleration, the level of which is dependant on the angle the plane makes with the horizontal. The setup shown in Figure 4.1 consists of two boxes. An inner box represents the processing facility and its nominal 100 kg mass. It fits inside a larger, or outer, box that is sized to fit inside the space of a space shuttle middeck locker. The motion of this outer box represents the motion of the spacecraft structure at the location of the microgravity facility mount. The inner box is given a generous 3 inches of clearance from the outer box on all sides to allow room for the PVDF actuators. The actuator configuration used, six single hinge actuators which make up three nodes on three sides of the inner box, takes into consideration all of the requirements specified in Chapter 2. An additional design consideration is the proper simulation of the microgravity dynamic environment present in low earth orbit for the frequency range of interest, 0.01 Hz. to 5 Hz. Any structural or dynamic suspension modes not associated with the microgravity isolation problem should be kept outside of this frequency range; or if this is impractical they should at least be accounted for. There is no universally accepted method for simulating this planar microgravity environment and consequently it is a major design issue. Some of the problems inherent in these issues are discussed by Gerhold in the analysis of his experimental design of a potential microgravity mount that uses air jets as the actuator.[7]

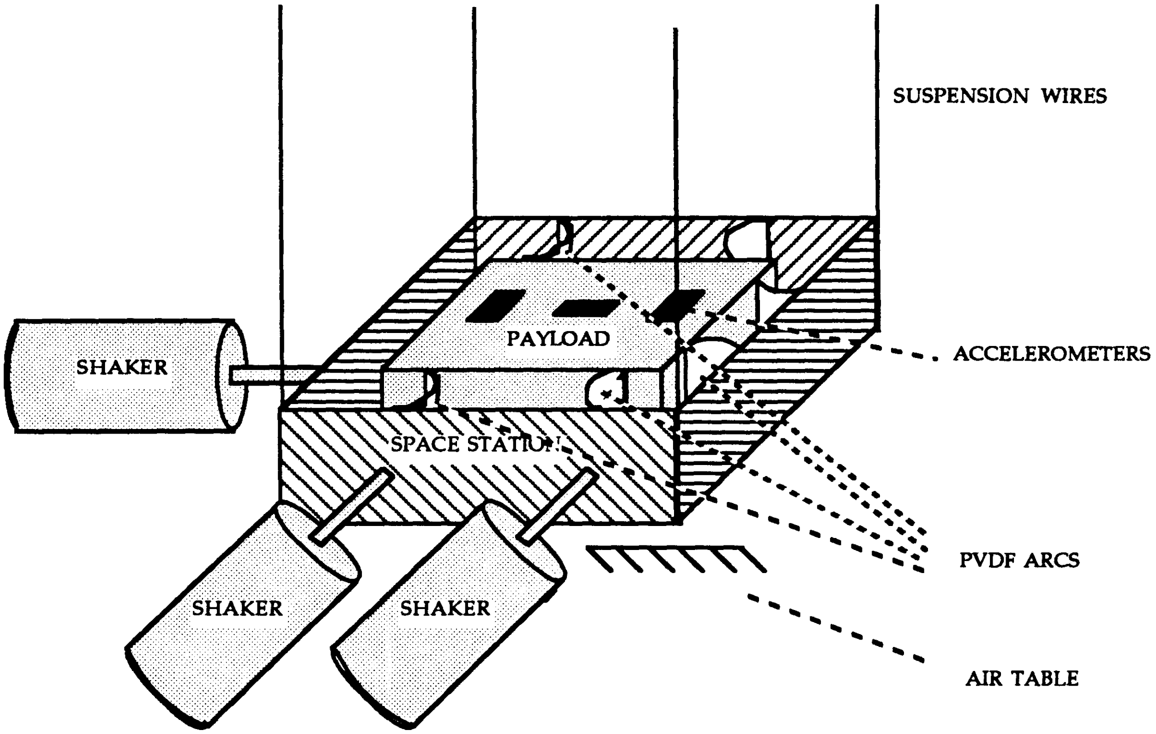

Figure 4.1: Three degree of freedom test set up

4.2.1 The Outer Box (Space Station)

The outer box represents the basebody side of the microgravity isolation mount. It is constructed of 60 mil sheet aluminum folded and assembled into a 20 inch x 17 inch x 14 inch box, the same size as a space shuttle mid-deck locker. There is no top or bottom to allow the internal placement, inspection, and modification of the payload (inner box), actuators, sensors, and payload suspension, even during an experimental run. Windows are also cut out of the sides of the box to allow more complete observation and the installation of any actuator mounting configuration/device without having to remake the entire box. The mounting devices are attached to clear lexan sheets that can be bolted into matching holes around the edges of the windows in the outer box. This metal outer box then hangs on four, meter long piano wire stands attached to the four upper corners of the box and its motion is excited by three electromagnetic shakers. The other end of the piano wire is on scaffolding bolted to the laboratory wall. The Ling Model 420 shakers are capable of commanding 0.95 cm displacement and are attached to the outer box by means of a thin metal rod called a *stinger*. Three are situated around the outer box as shown in Figure 4.1 so that motion can be commanded in both translational degrees of freedom and the lone rotational one. Since a shaker must command movement in one direction but must not oppose the motion commanded by another shaker, the stingers must provide a stiff connection to the outer box in the shaker and stinger axial directions and still be long and thus mechanically soft enough to allow side-to-side motion. A four inch long 70 mil diameter aluminum rod is sufficient for the job. It does not buckle under the loads applied by the shaker and does not have any internal vibrational modes within the control bandwidth. The displacement of the outer box at the attachment point of the stinger will essentially be the same as that of the moving head of the shaker. In order to monitor this displacement, another rod, this time threaded, is attached to the shaker head with an LVDT displacement transducer core at the other end. This core moves inside the LVDT housing changing its internal magnetic field producing a signal that is observed and stored using either a Nicolet 2090 oscilloscope or a Tektronix 2630 four channel Fourier analyzer supported by an IBM AT personal computer.

The above ensemble of equipment is used to simulate the motion of the space station structure at the mounting point of the microgravity facility. The shakers are electronically driven by a Wavetek model 21 signal generator, or one resident in the Fourier Analyzer. Both of the generated signals are amplified by Crown DC-300A Series II dual channel amplifiers. The shaker heads are large inductive coils that move in the magnetic field of a large permanent magnet. When current flows through the coil the internal magnetic field is altered, producing a force on the coil/head. The movement of the head is restrained by a flexure system that acts like a spring. Since the resonant frequency of the experimental set up on top of this spring is above 10 Hz., the magnetic force inside the shaker produces a shaker head displacement that is related to it with the inverse of the spring constant as a constant of proportionality. This ability to command the displacement of the outer box also means the ability to command its second derivative, or acceleration. The outer box can be commanded to produce the desired displacement and acceleration disturbance characteristics without the interference of any undesirable equipment dynamics to be accounted for in the control problem.

4.2.2 The Inner Box (Payload)

The inner box must be capable of holding 100 kg., be rigid in the frequency range of interest, and provide suitable mounting locations for the sensors and actuators to be used in the experiment. In order to allow sufficient room for the actuators, three inches of clearance is given between the inner and outer boxes on all sides resulting in an 11 inch x 14 inch x 8 inch inner box. This box is made out of the same material and fashion as the outer box except it has a bottom in order to hold the 100 kg of mass and only one window cut out of a side of the box. This window is to allow for easy internal observation during an experiment and easy addition or removal of inner box mass. It also reflects the probable need in the actual flight hardware for a side without actuators that allows astronauts to inspect the microgravity facility. Actuator attachment is thus permitted on three sides only. Holes are drilled into these sides of the box to allow the attachment of the actuator mounting devices for the PVDF arcs, thus allowing the desired mounting conditions. The Sundstrand QA-1400 accelerometers, the choice, location, and orientation of which is detailed in the next section, are mounted in separate custom mounting blocks on three different metal strips along the top of the box (Figure 4.2). The leads to these accelerometers represent the minimum umbilical cord needed by the payload and are draped between the tops of the two boxes so that the effective stiffness is less than 2 N/m.

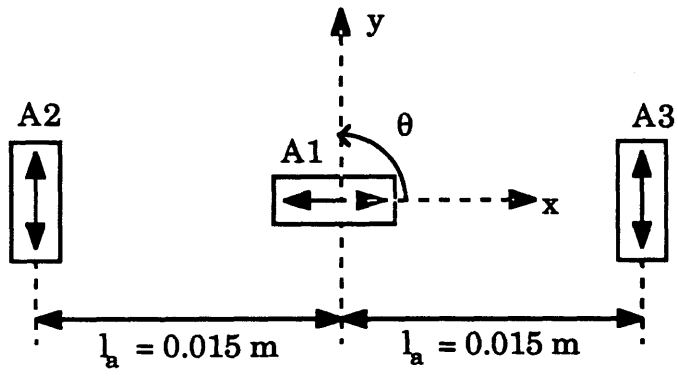

$$\ddot{x} = A1$$

$$\ddot{y} = (A2 + A3) / 2$$

$$\ddot{\theta} = (A3 - A2) / 2 \cdot l_a$$

Figure 4.2: Accelerometer placement configuration on the inner box with the equations used for calculating the acceleration of the payload relative to its geometric center of body

4.2.3 Payload Performance Sensors

The Sundstrand Q-Flex series accelerometers produced by Sundstrand Data Control, Inc. of Redmond, WA are the most sensitive commercially available accelerometers appropriate for the low frequency requirements of the microgravity experiment. Although the specifications listed in the brochures quote a resolution of less than 1 μg, they also specify 5 to 10 μg rms noise in the range of 0 to 10 Hz.. This is also the frequency range of our experiment and is thus unacceptable. Preliminary consultation with Sundstrand also indicated that these accelerometers would not be appropriate for the microgravity application. This prompted detailed research into developing a home built sensor, of force or acceleration, of sufficient sensitivity. A force transducer can measure the force transmitted to the inner box through the actuators and the acceleration can be calculated if the mass or inertia of the inner box is known. Accelerometers are usually force transducers that measure the force transmitted to a known proof mass; and since the largest proof mass available for use on the payload is the total payload itself, a force transducer was the focus of the design project. The most promising of these designs devised for this experiment were *soft* force transducers. Soft transducers are classified here as those not stiff enough to keep the internal dynamics of the unit above the upper limit of the control bandwidth. The resulting dynamics and control problem became more complicated. Upon consultation with Sundstrand at a later date, it was discovered that a *typical* QA-1400 or QA-2000 accelerometer has the noise profile described in Figure 4.3.[30-32] This is better than the specification quoted in the brochure and sufficient for a microgravity experiment. Resolution to less than 0.1 μg is possible depending on the noise floor of specific units involved and the laboratory environment. The signals from the QA-1400 accelerometers used in the set up are conditioned using Micromeasurements 2120 strain gage conditioners specially modified to provide the necessary gain for the signals and zero out any bias acceleration resulting from the slight but invariant tilting of each accelerometer. Force transducers are still a valid method of performing this type of experiment and the information learned while investigating this technology is by no means useless. The main points of this topic are discussed in Appendix B.

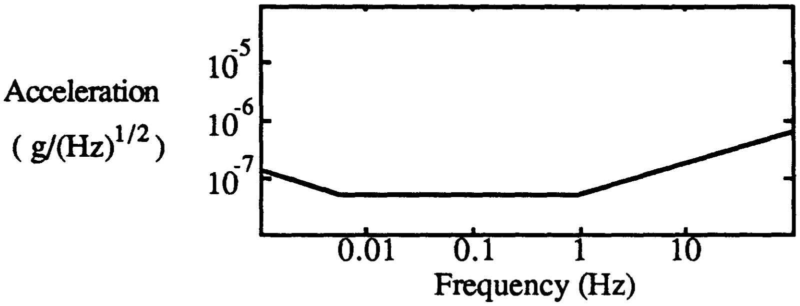

Figure 4.3: Acceleration noise profile of a typical QA-1400 or QA-2000 accelerometer.

Another factor to consider is the thermal characteristics of the accelerometer. The bias value can change as much as 1 μg/deg K and the scale factor can change as much as 1 part in 10,000 per deg K. Since the measured accelerations did not exceed a dynamic range of 4 orders of magnitude, this second specification was not of any consequence. The accelerometers appear to be sufficiently thermally insulated so that: 1) the time constant of any temperature change is large enough so that the frequency of this disturbance below 0.01 Hz, or 2) it reduces the amplitude to a level not detected. This type of precaution has not proved itself necessary but must be addressed nonetheless. Data of sufficient quality is taken at night to achieve the desired quality and resolution.

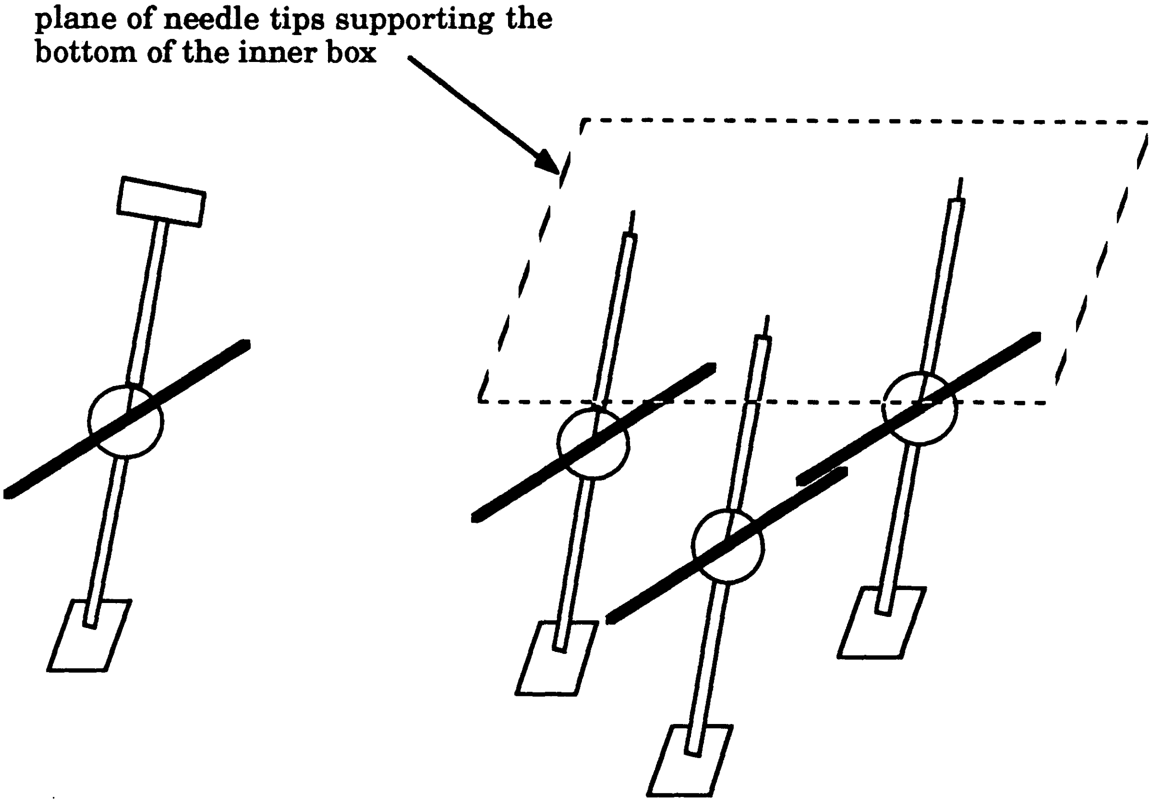

a) Single pendulum b) Complete system

Figure 4.4: Inverted/non-inverted pendulum suspension system: a) single pendulum, b) complete system.

4.2.4 Inner Box (Payload) Suspension

The inner box suspension must be able to hold 100 kg and behave like an unrestrained mass between the frequencies of 0.01 Hz and 5 Hz. Simple mathematics show that if the box is hung by a wire pendulum suspension, the wire must be at least 2.5 km long. One way in which a pendular suspension might achieve a resonant frequency below 0.01 Hz in the lab is if a coupled inverted/non-inverted pendulum suspension system is used instead. In this system a regular and an inverted pendulum are coupled (Figure 4.4) so that the composite center of gravity of the system is marginally below its pivot point. The system is marginally stable. The stability of this type of system can be visualized in a root locus like diagram with the location of the center of gravity as the varied parameter that produces the locus of the roots of the characteristic equation. See Figure 4.5. The system begins with a stable center of gravity well below the pivot point the system and has a certain resonant frequency. When the center of gravity is moved higher and thus closer to the pivot point, the resonant frequency becomes smaller in magnitude and the poles of the system migrate toward the origin until the center of gravity is above the pivot point and wants to rotate towards its stable equilibrium below the pivot point. In this case the poles of the system are now on the positive and negative real axes of the complex plane. This type of suspension system was attempted with a steel rod which extended approximately one half of a meter either side of the pivot point. The pivot point was a steel needle point resting on top of the side of a razor blade. Unfortunately, it was difficult to consistently balance the pendulum system so that the period of oscillation was below 10 seconds. Periods of greater than 100 seconds were occasionally achieved when the inner box was rigidly fixed to the top end of a single rod but the inner box is constrained to tilt with the pendulum. The gravitational acceleration on the surface of the earth then influences the accelerometers and shows up in the experimental data. Since the pendulum could tilt on the order of 0.01 radians in an experiment, a false acceleration reading of 0.01 g's could be observed. This is 10000 times the desired isolation level and is not only not negligible but is also overwhelming when attempting microgravity isolation. This effect indicates that the box should also have its own pivot point on the top of the pendulum. Three of these pendula must be used so the box has three points of contact about which it can rotate to that keep it in a horizontal plane. When suspension balancing was performed on the three pendulum system other modes of pendulum instability appeared. A rotational mode about the vertical axis was very sensitive to nonuniformity between the each of the pendula and the dexterity of the experimenter. Mount frequencies of a little less than 0.1 Hz. were the best results achieved. This method was abandoned when a successful air table suspension was manufactured and when it was discovered that the distance the pendulum center of gravity has to be below the pivot point was approximately the minimum diameter of circular area of steel necessary to hold up the payload mass without material compressive failure. The ability to get the frequency of the above inverted pendulum system mount below 0.01 Hz was contingent upon favorable crushing dynamics of the steel needlepoint and the ability to manufacture and balance three identical pendula. This method may still be viable if harder pivot materials are used; however, the air table solution below is more practical.

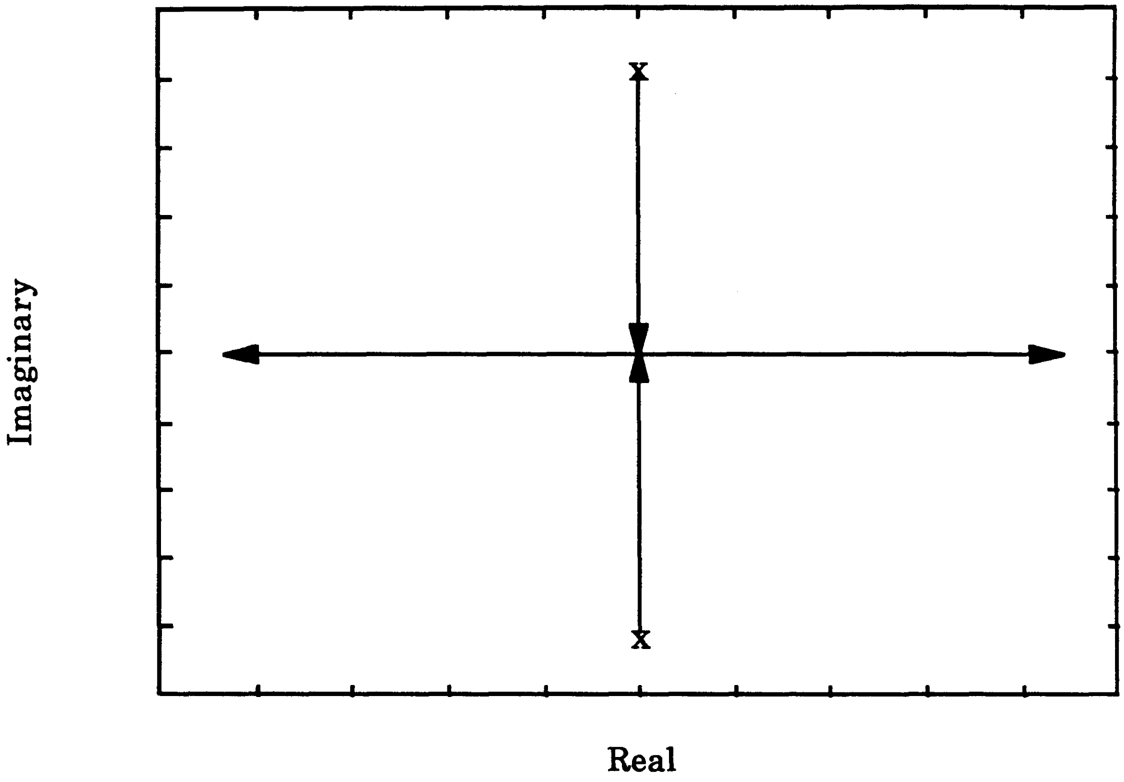

Figure 4.5: locus of the roots of the characteristic equation of the coupled pendulum system as the center of gravity is shifted from below the pivot point to above it.

An air table is a much simpler to build and easier to balance suspension system than the pendulum system described above. The inner box rests on top of an aluminum plate, or puck, that has a flat lower surface. This plate in turn rests on top on a slightly larger flat aluminum plate with a hole in the middle to allow the flow pressurized air. Since the payload will not move much (less than 0.5 cm without active isolation) and the puck is 11 inches by 14 inches, it was decided that it was unlikely that there would be any observed dynamics that would effect the control experiment. None were observed. The table is leveled before each run by turning the three levelling screws upon which the air table surface rests. These screws are in turn screwed into a third aluminum plate that rests upon sturdy table legs. When the air is turned on (from either an air compressor or a tank of compressed nitrogen) and the pressure underneath the puck gets to a sufficient magnitude, it floats on a thin layer of air. This isolates the puck from the horizontal motion of the air table. The air pressure can be turned up almost arbitrarily high producing a thicker air film. This allows for more turbulence and possible puck rotation about a horizontal axis giving undesirable readings on the payload accelerometers. If the air pressure level feeding the table is kept to a sufficient level (1 to 2 psi for a 10 kg puck) the accelerometer noise level can be kept to a μg or less. Since the table is relatively flat there are no observed restoring or destabilizing forces which create system oscillation modes at frequencies above 0.01 Hz. The air table meets the three degree of freedom suspension requirements.

4.2.5 Umbilical Cord and Piezo Actuation

Attached between the inner box and the outer box are the PVDF actuators and the sensor leads which simulate the umbilical cord and mount dynamics. Theoretically only three actuators are needed to control three degrees of freedom of motion but a total of six PVDF arcs are used here to provide redundancy, force balancing, and simplicity of control scheme visualization. One node is attached to each of the three available sides of the inner box. Each node can act in its local vertical or p-direction to control the translational degrees of freedom and the two nodes that are situated on opposite sides of the box can act in a differential mode to counter rotational accelerations. Although a node working in its differential mode couples with some local horizontal or q-direction motion, two nodes on opposite sides of the payload will have horizontal effects that can nearly cancel each other out. Also, six arcs of the type discussed in the following paragraph were needed to produce the desired mount stiffness/resonant frequency.

The experiment dimensions discussed earlier in this chapter were first determined using the preliminary actuator sizing in Chapter 3 (see Table 3.1) and supported by the verification of the gross characteristics of single piezoelectric film arcs discussed in Chapter 5. Further experimentation (again Chapter 5) performed after the construction of the two boxes necessitated a change in the originally envisioned 4 arc, 2 node system. When it was discovered that the arcs lay flat on the mounting surface when in compression, thus changing the stiffness characteristics and resulting displacement, it was decided to move the mounting locations away from the mounting surfaces. Spacers are placed in between the outer box and the lexan mounting windows to allow an extra inch between the windows and the inner box. It was also decided to use single hinge arcs (clamped at the spacecraft end and hinged at the payload end) to produce large enough displacements from the actuators (also discussed in Chapters 2 and 5). All of the considerations resulted in the actuator mounting device shown in Figure 4.6. The arc is clamped in between two lexan blocks one of which is affixed to the lexan window on the outer box. Nylon screws apply the clamping pressure between the blocks. The block that is attached to the lexan sheet is 1/2 inch thick to provide the desired spacing. The clamp is also lined with a soft viscoelastic material called Poron to reduce the chances of the development of any mechanical flaws that can lead to the arcing of electricity that can burn holes into an actuator and render it useless. The soft lining reduces the stress at any pressure points caused by sharp edges inadvertently produced while attaching the electrical leads to the piezoelectric arcs. This soft material also reduces the stress and strain concentration resulting from the bending of the arc at the root thus reducing the fatigue present in the metallization and PVDF at that location. The other end is hinged with a mylar sheet that rests in a clamp attached to the inner box. This clamp has threaded holes on the plate closest to the outside box and its bolt is screwed from the inside of the box. A spring is placed around the screw and in between the box and the other plate so that the distance between the two clamps can be altered slightly to accommodate the small deviations in actuator size and other physical properties. The equations concerning the actuator configuration and the mounting device described here are addressed in section 4.3.

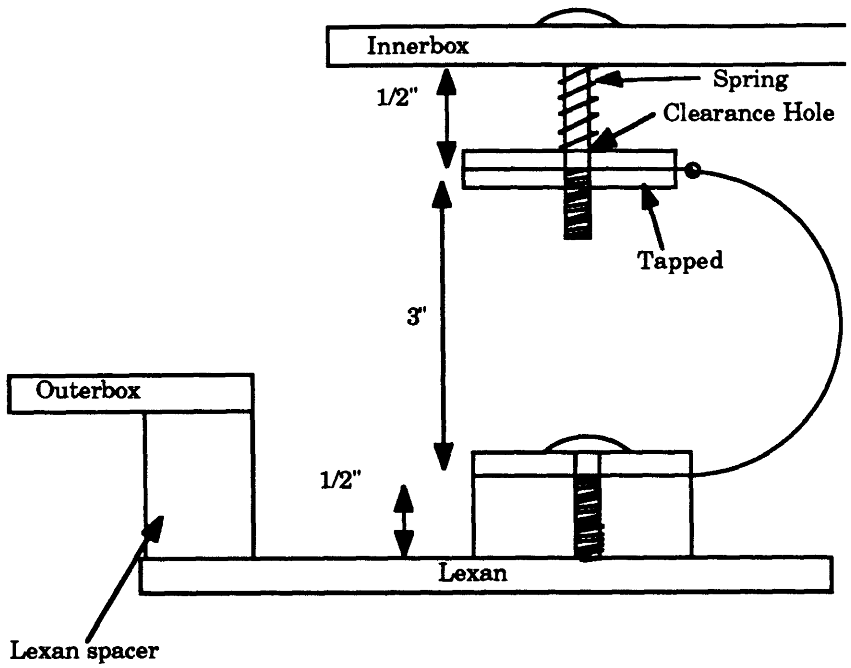

Figure 4.6: Mounting configuration of a single hinge arc in the experimental setup.

4.2.6 Controller Properties

The three accelerometers are situated so that the accelerations can be determined for each degree of freedom relative to the geometric center of the box. The sensors are mounted on three metal bars across the top of the payload box as described in section 4.2.2 with one 11 inch bar across each end of the box and one across the middle and are configured to make the desired measurements (Figure 4.2). The bar in the middle houses the accelerometer that measures the acceleration in the translational degree of freedom controlled by only one node and thus points in a direction perpendicular to the bar from now on called the x-direction. The other two accelerometers are placed 15 centimeters from the middle accelerometers. They are pointing parallel to the bars and when averaged can produce the translational acceleration in the other perpendicular direction otherwise known as the y-direction. The rotational acceleration is deduced by subtracting the two y-direction accelerometers and dividing by twice the moment arm. The equations showing this algebraic manipulation are also shown in Figure 4.2.

Although the control experiment was not completed in this research, and the solving of this problem is a matter of future research, the following is an outline of a plausible control strategy. It is mentioned here to show how the microgravity experiment and mount described and produced here can accommodate a controller. The control problem can be tackled by decoupling all three DOF through input/output transformations and controlling them separately. Modal analysis is used to identify the modal parameters from actual experimental data. Modal decoupling techniques are then exploited to determine the decoupling transformations from the actuation to the measured acceleration. Descriptions of these techniques can are discussed by Ewins and Meirovitch.[33-34] This data can be recorded using the Fourier analyzer and the experimental modal parameters can be calculated and manipulated using existing software such as the STAR modal analysis program produced by Structural Measurement Systems.[35] This type of program produces curve fits and modal parameters given the transfer function data from shaker displacement or piezoelectric arc voltage to accelerometer acceleration. Once these modal parameters are identified in terms of the inputs and outputs, normalized mass and stiffness matrices can be derived. Modal separation can then be performed producing a set of normal coordinates which have specific transformations to the original mass and stiffness matrices. The specific values for each controller are then determined for each mode using the controller specified in section 2.4.2.; although other control techniques may be used. Once again, this control approach is only one suggested to illustrate the readiness of the microgravity mount to employ a control controller and a control strategy.

4.3 Three Degree of Freedom Model

In Chapter 3 the arc equations were derived for the displacement of the tip of the arc relative to its equilibrium position assuming that the other end of the arc that is attached to the rigid wall does not move. However, the wall does move; otherwise there would be no need for isolation. The three degree of freedom experiment will consist of six arcs (three nodes) on three different sides of the actuator as shown in Figure 4.1. Since the displacement equations have been expressed in terms of the payload displacement relative to the space station wall, these equations must be expanded to include the actual displacements of both locations (see Figure 4.7). Once this is accomplished these arc end displacements can be derived from the displacement of the spacestation expressed at one reference point and the displacement of the payload at another reference point. Here the reference points are taken to be the area or geometric centers of each of the boxes of the lab experiment. In equilibrium, with no external forces, these two points sit on top of each other in the center of the experiment (Figure 4.8). Notice that the center of gravity of the inner box will not necessarily be at this reference point. It is even possible that the center of gravity of the payload may change. This section develops the three degree of freedom dynamic model capable of performing the tasks described above. It can then be used to predict the properties of the system and help design a controller when used in conjunction with experimentally measured system properties.

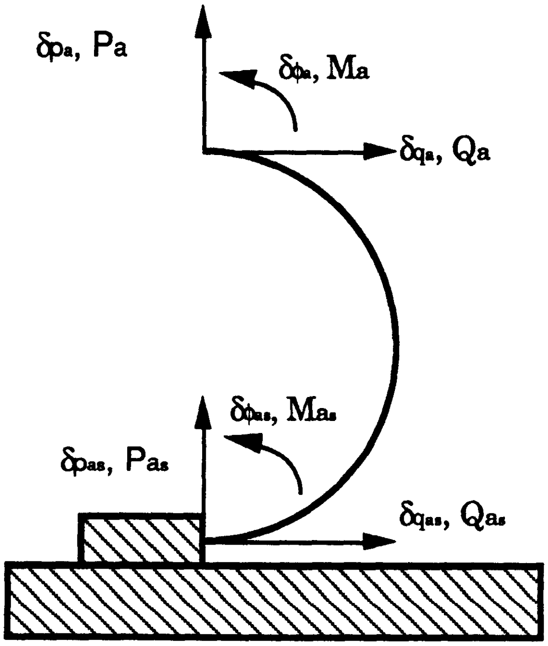

Figure 4.7: Forces acting on the payload are dependent on both the displacement of the payload and the spacecraft.

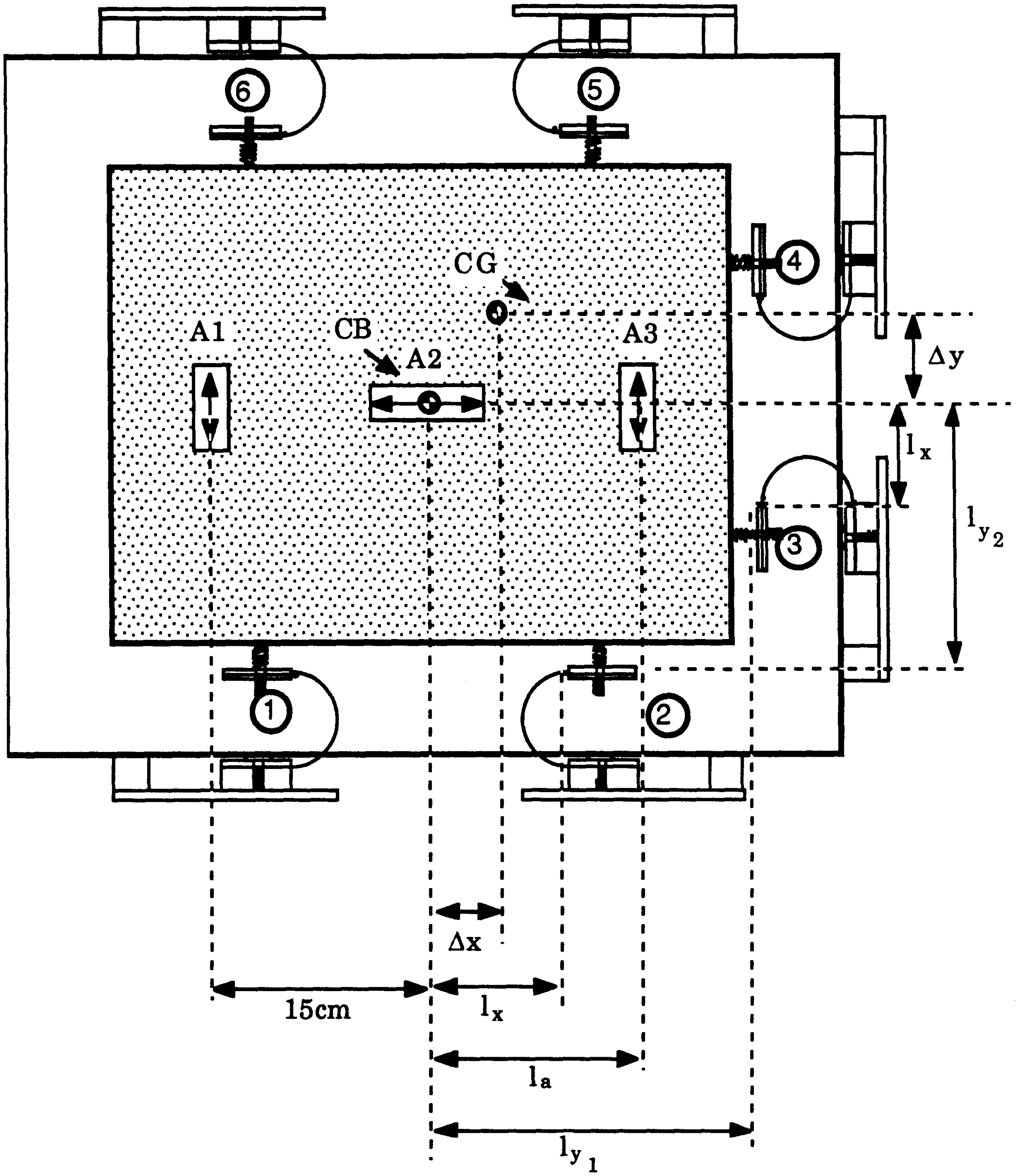

Figure 4.8: Analysis model of the six arc, three node, three DOF single plane microgravity isolation experiment

If the compliance equation expressed in Eqs. (3.6.1) is altered so that it is a stiffness equation, the force acting on the payload becomes

$$\begin{bmatrix} P_a \\ Q_a \end{bmatrix} = -\frac{EI_z}{\left(\frac{3\pi^2}{4} - 4\right)R^3} \begin{bmatrix} \frac{\pi}{2} & -2 \\ -2 & \frac{3\pi}{2} \end{bmatrix} \begin{bmatrix} \delta_p \\ \delta_q \end{bmatrix} \tag{4.3.1}$$

where $\mathbf{K_a}$ = mechanical arc stiffness = $\mathbf{A_a}^{-1} = -\frac{EI_z}{\left(\frac{3\pi^2}{4} - 4\right)R^3} \begin{bmatrix} \frac{\pi}{2} & -2 \\ -2 & \frac{3\pi}{2} \end{bmatrix}$ (4.3.2)

and $\delta a = [\delta qa \ \delta pa]^T, \qquad \mathbf{Fa} = [Qa \ Pa]^T$ (4.3.3)

Since the piezoelectric equations of chapter 2 relate a displacement to a particular voltage, the force to voltage relation can be calculated by multiplying by the above mechanical stiffness. This leaves

$$\begin{bmatrix} P_a \\ Q_a \end{bmatrix} = -\frac{Ebh_1 n_1^2 d_{31}}{\left(\frac{3\pi^2}{4} - 4\right)R} \begin{bmatrix} \frac{\pi^2}{2} - 4 \\ \pi \end{bmatrix} V \tag{4.3.4}$$

With the arc relations expressed in terms of the displacement of its local reference point it is desirable to express the whole system of equations with respect to a global reference point. This global reference point is the geometric center of the box. When the translational forces and resulting moments contributed by each arc are accounted for

$$\begin{bmatrix} F_x \\ F_y \\ M \end{bmatrix} = \begin{bmatrix} Q_1 \\ P_1 \\ Q_1 l_{y_1} - P_1 l_x \end{bmatrix} + \begin{bmatrix} -Q_2 \\ P_2 \\ -Q_2 l_{y_1} + P_2 l_x \end{bmatrix} + \begin{bmatrix} -P_3 \\ Q_3 \\ Q_3 l_{y_2} - P_3 l_x \end{bmatrix}$$

$$+ \begin{bmatrix} -P_4 \\ -Q_4 \\ -Q_4 l_{y_2} + P_4 l_x \end{bmatrix} + \begin{bmatrix} -Q_5 \\ -P_5 \\ Q_5 l_{y_1} - P_5 l_x \end{bmatrix} + \begin{bmatrix} Q_6 \\ -P_6 \\ -Q_6 l_{y_1} + P_6 l_x \end{bmatrix} \tag{4.3.5}$$

where the numerical subscripts to the local forces P and Q refer to the arc that is numbered in Figure 4.8, l_x refers to the local q direction moment arm of the local q direction force applied by the arc, and l_{y_1} and l_{y_2} refer to the local p direction moment arm of the local p direction applied forces. When this is expressed in terms of force vector matrices and transformation matrices we get

$$\mathbf{F}_p = \mathbf{G}_1\mathbf{F}_1 + \mathbf{G}_2\mathbf{F}_2 + \mathbf{G}_3\mathbf{F}_3 + \mathbf{G}_4\mathbf{F}_4 + \mathbf{G}_5\mathbf{F}_5 + \mathbf{G}_6\mathbf{F}_6 \qquad (4.3.6)$$

where $\mathbf{G}_1 = \begin{bmatrix} 1 & 0 \\ 0 & 1 \\ l_{y_1} & -l_x \end{bmatrix}$, $\mathbf{G}_2 = \begin{bmatrix} -1 & 0 \\ 0 & 1 \\ -l_{y_1} & l_x \end{bmatrix}$, $\mathbf{G}_3 = \begin{bmatrix} 0 & -1 \\ 1 & 0 \\ l_{y_2} & -l_x \end{bmatrix}$

$$,\mathbf{G}_4 = \begin{bmatrix} 0 & -1 \\ -1 & 0 \\ -l_{y_2} & l_x \end{bmatrix}, \quad \mathbf{G}_5 = \begin{bmatrix} -1 & 0 \\ 0 & -1 \\ l_{y_1} & -l_x \end{bmatrix}, \text{ and } \quad \mathbf{G}_6 = \begin{bmatrix} 1 & 0 \\ 0 & -1 \\ -l_{y_1} & l_x \end{bmatrix}$$

Now the displacements of each arc end must be related to those of the center of gravity, c. g., of the payload. The coordinates of the arc end locations have already been implied through the introduction of the moment arm distances about the box geometric center. If the small angle approximation is made for the rotational effects it is discovered that the same transformation matrices presented above also relate the arc end points to the arc center of body.

$$\delta_i = \mathbf{G}_i^{\mathrm{T}}\,\delta_{pr} \qquad i = 1,2,\ldots,6 \qquad (4.3.7)$$

If the center of body forces in Eq. 4.2.6 are transformed to be in terms of the payload center of body displacements, then

$$\begin{bmatrix} F_x \\ F_y \\ M \end{bmatrix} = \left[\sum_{i=1,6}^{1} \left[G_i K_a G_i^T \right] \right] \delta_{pr} + \left[G_1 \quad G_2 \quad G_3 \quad G_4 \quad G_5 \quad G_6 \right] K_p \begin{bmatrix} V_1 \\ V_2 \\ V_3 \\ V_4 \\ V_5 \\ V_6 \end{bmatrix} \qquad (4.3.8)$$

where, $\mathbf{V}_o = [V_1 \; V_2 \; V_3 \; V_4 \; V_5 \; V_6]^T$

The vector matrix, $\mathbf{V}_o$, of applied piezoelectric arc voltages must also be transformed to reflect the three actuator groupings discussed in the section 4.2. The actuator groupings are labelled in numerically increasing order from left to right. The two left-most actuators, each on different sides of the inner box, are the first group while the middle two actuators are the second one. The right most actuator group, number 3, is the only node electrically driven purely in its extensional mode and does so in the x-direction. The other two groups will excite the y-direction motion when they both act together and rotational motion when are driven in opposition. The superposition of both of these signals determines the actual signal sent to each group. The following transformation matrix $\mathbf{G}_v$ will perform this function.

$$\mathbf{V}_o = \mathbf{G}_v \mathbf{V} \qquad (4.3.9)$$

where $$\mathbf{G}_v = \begin{bmatrix} 0 & 1 & -1 \\ 0 & 1 & 1 \\ -1 & 0 & 0 \\ -1 & 0 & 0 \\ 0 & -1 & -1 \\ 0 & -1 & 1 \end{bmatrix}, \quad \mathbf{V} = \begin{bmatrix} V_1 \\ V_2 \\ V_3 \end{bmatrix}$$

which then transforms (4.2.8) into

$$\begin{bmatrix} F_x \\ F_y \\ M \end{bmatrix} = \left[\sum_{i=1,6}^{1} \left[G_i K_a G_i^T \right] \right] \delta_{pr} + \left[G_1 \quad G_2 \quad G_3 \quad G_4 \quad G_5 \quad G_6 \right] K_p G_v V \qquad (4.3.10)$$

When the above transformation, stiffness and actuation matrices are manipulated so that only coefficients for δ_{pr} and $\mathbf{V}$ remain, the above equation becomes

$$\mathbf{F} = \mathbf{K}_\delta \delta_{pr} + \mathbf{K}_v \mathbf{V} \qquad (4.3.11)$$

where $$\mathbf{K}_\delta = \frac{-EI_z}{\left(\frac{3\pi^2}{4} - 4\right)} \begin{bmatrix} 5\pi & 0 & 0 \\ 0 & 7\pi & \pi l_{y_2} + 4l_x \\ 0 & \pi l_{y_2} + 4l_x & 2\pi l_{y_1}^2 + \pi l_{y_2}^2 + 16 l_x l_{y_1} + 8 l_x l_{y_2} + 9\pi l_x^2 \end{bmatrix}$$

and $$\mathbf{K}_v = \frac{Ebh_1 n_1^2 d_{31}}{\left(\frac{3\pi^2}{4} - 4\right) R} \begin{bmatrix} 2\pi & 0 & 0 \\ 0 & 4\pi & 0 \\ 0 & 0 & 4\left(\pi l_x - \left(\frac{\pi^2}{2} - 4\right) l_{y_1}\right) \end{bmatrix}$$

In order to get the complete force equation for the whole system we must now transform these actuator/spring forces so that they act at the payload center of gravity. This is done by premultiplying by the transformation matrix $\mathbf{G}_{f_{cg}}$. At this point the inertia matrix, $\mathbf{M}_{cg}$, containing the mass and inertia of the payload can be introduced along with the displacement of the payload center of gravity. The dynamics of the system can now be analyzed.

$$\mathbf{M}_{cg} \ddot{\delta}_{cg} = \mathbf{G}_{f_{cg}} \mathbf{K}_\delta \delta_{pr} + \mathbf{G}_{f_{cg}} \mathbf{K}_v \mathbf{V} \qquad (4.3.12)$$

and
$$\mathbf{G}_{\mathrm{f}_{cg}} = \begin{bmatrix} 1 & 0 & 0 \\ 0 & 1 & 0 \\ \Delta y & -\Delta x & 1 \end{bmatrix}$$

This analysis is made easier when only one set of displacements is in the equations; and since there is a simple transformation between the payload center of gravity and geometric center of body, $\mathbf{G}_{\delta_{cg}}$, the whole equation can be put in terms of the directly measurable payload geometric center of body equations.

$$\mathbf{M}_{cg}\mathbf{G}_{\delta_{cg}}\ddot{\delta}_{pr} - \mathbf{G}_{\mathrm{f}_{cg}}\mathbf{K}_{\delta}\delta_{pr} = \mathbf{G}_{\mathrm{f}_{cg}}\mathbf{K}_{v}\mathbf{V} \tag{4.3.13}$$

where
$$\mathbf{G}_{\delta_{cg}} = \begin{bmatrix} 1 & 0 & -\Delta y \\ 0 & 1 & \Delta x \\ 0 & 0 & 1 \end{bmatrix}$$

and when these terms are multiplied out to produce the standard format of mass, stiffness and actuation matrices, the following form of equations results.

$$\mathbf{M}\ddot{\delta}_{pr} + \mathbf{K}\delta_{pr} = \mathbf{K}_{e}\mathbf{V} \tag{4.3.14}$$

where
$$\mathbf{K}_{e} = \frac{Ebh_l n_l^2 d_{31}}{\left(\frac{3\pi^2}{4} - 4\right)R}\begin{bmatrix} 2\pi & 0 & 0 \\ 0 & 4\pi & 0 \\ 2\pi\Delta y & -4\pi\Delta x & 4\left(\pi l_x - \left(\frac{\pi^2}{2} - 4\right)l_{y_1}\right) \end{bmatrix}$$

and
$$\mathbf{K} = \frac{-EI_z}{\left(\frac{3\pi^2}{4} - 4\right)}\begin{bmatrix} 5\pi & 0 & 0 \\ 0 & 7\pi & \pi l_{y_2} + 4l_x \\ 5\pi\Delta y & \pi l_{y_2} + 4l_x - 7\pi\Delta x & 2\pi l_{y_1}^2 + \pi l_{y_2}^2 + 16 l_x l_{y_1} + 8 l_x l_{y_2} + 9\pi l_x^2 - \Delta x\left(\pi l_{y_2} + 4l_x\right) \end{bmatrix}$$

To make the equations suitable for performing a control analysis, the relative displacement used in the above equations should be replaced by the true inner and outer box geometric center displacements. The force transmitted to the payload is determined by the relative displacement of the two bodies. If this is linearized about an equilibrium point where the inner and outer box centers are at the exact same location and second order displacement terms are ignored, the relation is simply $\delta_{pr} = \delta_{pay} - \delta_{sc}$. The subscript $_{pay}$ refers to the center of the inner box or payload and $_{sc}$ for that of the outer box or spacecraft. In this relation the payload acceleration is still absolute; so its subscript is merely changed to $_{pay}$ to reflect the new notation. This gives the final relation

$$\mathbf{M}\ddot{\delta}_{pay} + \mathbf{K}\delta_{pay} = \mathbf{K}\delta_{sc} + \mathbf{K_e V} \qquad (4.3.15)$$

4.4 Predicted Dynamic Characteristics

The above dynamics are analyzed below for the following single hinge actuator. The arc dimensions were initially chosen for arcs clamped at both ends. It was decided to continue with that arc design that was originally intended for the mount where both ends of the arc are clamped. By the time the arc mounting configuration studies were completed, it became apparent that a mount with single hinge arcs would probably be at least three times as stiff, 6 N/m, as the minimum umbilical cord stiffness, 2 N/m, envisioned by Jones et al.[4] These arcs had also been tested individually and in node form and found to have the necessary displacement capability of at least ±2.5 mm. All of the pertinent physical information is listed in Table 4.1. Verification of these properties is done by comparing the transfer functions from the shaker motion and applied piezoelectric voltage to the accelerometers. The display of these transfer functions is delayed until the presentation of the results so that they may be displayed together for comparison. Please take note that the measured transfer functions in Chapter 5 are those from each separate actuator group, not a combination of groups as derived in the previous section. This changes the transformation matrix, **Gv**, and the piezoelectric actuation matrix **Kv** to

$$\mathbf{G}_v = \begin{bmatrix} 0 & 1 & 0 \\ 0 & 0 & 1 \\ -1 & 0 & 0 \\ -1 & 0 & 0 \\ 0 & 0 & -1 \\ 0 & -1 & 0 \end{bmatrix} \tag{4.4.1}$$

$$\mathbf{K}_v = \frac{Ebh_l n_l^2 d_{31}}{\left(\frac{3\pi^2}{4} - 4\right)R} \begin{bmatrix} 2\pi & 0 & 0 \\ 0 & 2\pi & 2\pi \\ 0 & -2\left(\pi l_x - \left(\frac{\pi^2}{2} - 4\right) l_{y_1}\right) & 2\left(\pi l_x - \left(\frac{\pi^2}{2} - 4\right) l_{y_1}\right) \end{bmatrix} \tag{4.4.2}$$

4.5 Summary

This chapter has described the specifics of the three degree of freedom experiment performed in the laboratory. The hardware options and choices are discussed and the equations of motion have been derived. The experiment is capable of performing to the desired specifications and the specific mount performance characteristics have been specified. All that remains is to successfully verify the dynamics discussed in detail in Chapters 2, 3, and 4 and achieve microgravity isolation.

Table 4.1: Measured experiment dimensions and predicted mount capabilities with glue layer corrections

Quantity	Symbol	Value
Mass, inner box	m_p	7 kg
Estimated moment of inertia	I	0.12 kg/m^2
Average arc radius	R	0.038 m
Avg. PVDF layer thickness	h_l	31 µm
Avg. glue layer thickness	A_{gl}	3 µm
Local q-direction moment arm for each arc	l_x	0.085 m
Local p-direction moment arm for arcs 1, 2, 5, and 6	l_{y_1}	0.155 m
Local p-direction moment arm for arcs 3 and 4	l_{y_2}	0.195 m
Radial displacement of accelerometers 2 and 3 from the center of body	l_a	0.15 m
X direction stiffness	–	6.5 N/m
Y direction stiffness	–	9.1 N/m
X direction displacement capability	–	4.6 mm
Y direction displacement capability	–	6.4 mm
X direction force capability (up to 800v max.)	–	36 µN/V
Y direction force capability (up to 800v max.)	–	72 µN/V

Chapter 5

Experimental Results

5.1 Overview

This chapter details the confirmation of the gross PVDF film arc characteristics and its ability to perform the microgravity vibration isolation specified in Chapter 2. The first section will go over the confirmation of the single arc characteristics, both mechanical and piezoelectric. This will be followed by simple experiments performed on single nodes with various mounting schemes to verify the nodal characteristics discussed in Chapter 3. These results determined the type of actuator configuration and mounting schemes used in the three DOF experiment designed outlined and analyzed in Chapter 4. The chapter then closes by discussing the results of the three degree of freedom experimentation that was performed.

5.2 PVDF Film Arc Properties Verification

The main observation from this group of experiments is that the predictability of the single arc properties is very dependent on slight variations in the shape of the arc in its static equilibrium position without any applied voltage. The verification of the mechanical stiffness was performed by clamping a single arc to a flat surface so that the tip of the arc is directly above the clamped end as shown is Figure 5.1. Various masses (varying thicknesses of 3M Post-It Pads cut down to size to fit on the tip of the arc, using the adhesive to avoid slipping off) were placed on the tip of the actuator. Gravity provides a downward force on the tip of the arc. For each mass, the horizontal and vertical displacements of the tip from its equilibrium position were recorded by reading off the displacements from a grid printed on a transparency and affixed to clear lexan. The gross actuator shape was also recorded by noting not only the position of the tip of the arc but its highest point, or top, as well. The locations of these points were recorded and the changes in displacement were calculated by subtracting out the equilibrium position. The electrically induced displacement measurements and calculations were performed in a similar manner.

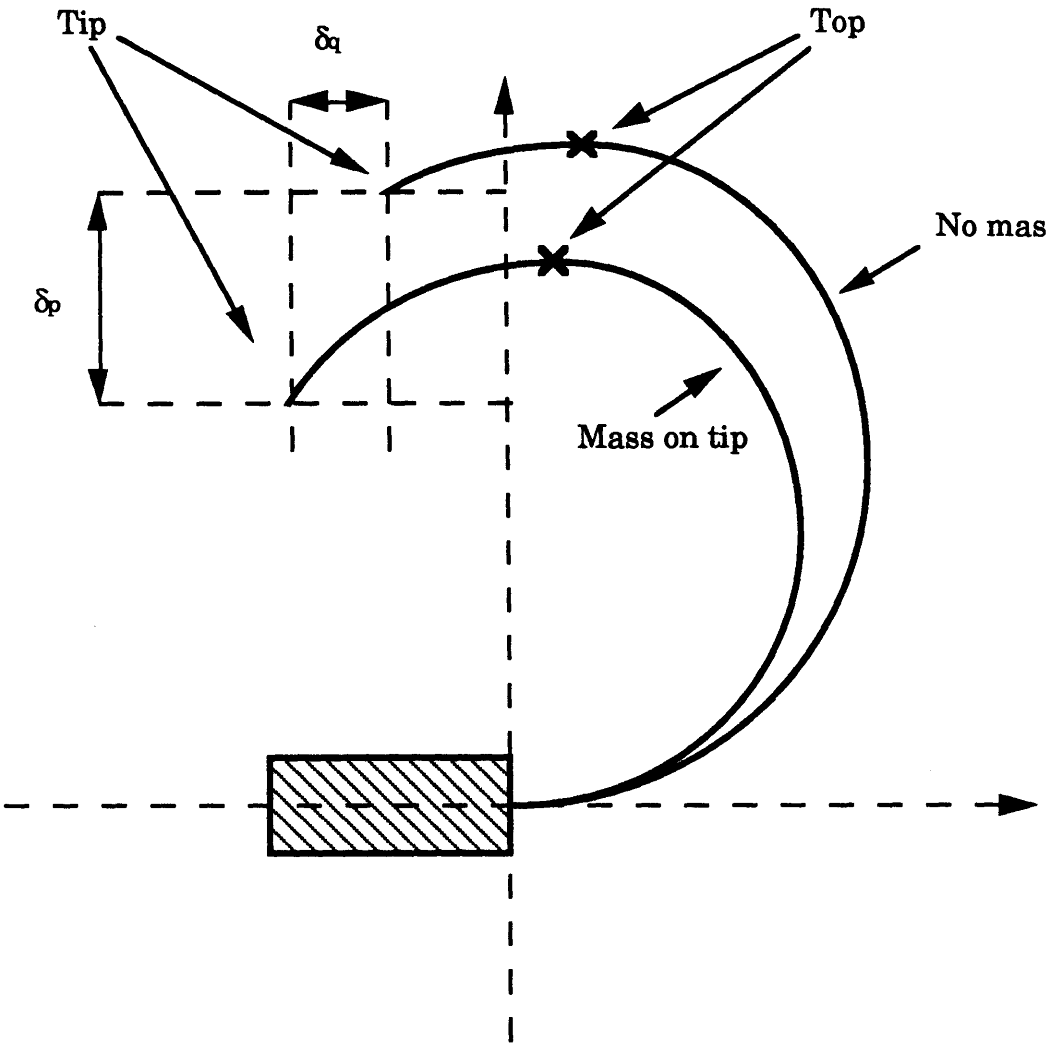

Figure 5.1: Experimental set up for verifying the physical characteristics of a single PVDF arc. Measured quantities are also indicated

It was discovered that the displacements were very sensitive to the equilibrium position or operating point of the arc. Since these arcs were placed in an upright position, not only would gravity provide a force on the weights affixed to the arc tip, gravity would also provide a distributed force along the length of the arc. This force distorts the shape slightly so that arcs are no longer semicircles. The arcs bend over so that their shape is not as close to being of a circular shape as before; but more importantly, the arc angle of the actuator has increased to greater than π radians. In some cases, additional strain was introduced into the arcs during the cure process. This produced arcs already deformed in this fashion. When the layers are taped to be held down onto the mold, extra strain is introduced to that layer. If these strains are of high enough magnitude and do not balance each other out, the additional bending moment will alter the equilibrium arc radius and angle. Since the gross shape of the actuator is recorded by way of the location of the tip and top of the arc, adjusted stiffness coefficients can be calculated and verified using Castigliano's Method as described in Chapter 3. Another necessary alteration to this verification analysis is the division of the applied forces into their radial and circumferential components. They are defined by the deduced center of the arc and the location of the arc tip when in its static equilibrium position. The method described below is an extension of the type of analysis used in Section 3.7 to characterize a two hinge arc of angle greater than π and the original type of arc analyzed by Sirlin and Laskin. The p-direction is now defined as the vector starting at the center of the arc, pointing radially outwards through the tip of the actuator. The q-direction is perpendicular to that and is thus the circumferential direction. The moment equations for the p- and q-direction forces are

p-direction: $$M = -PR\sin\theta \qquad (5.2.1)$$

q-direction: $$M = -QR(1 - \cos\theta) \qquad (5.2.2)$$

and the piezoelectrically induced moment is still the same as in Chapter 3. Using the method demonstrated in Chapter 3, including the fictional forces when necessary, the compliance equations that describe the arc become

$$\delta_p = \frac{PR^3}{EI}\left(\frac{\Psi}{2} - \frac{\sin 2\Psi}{4}\right) \qquad (5.2.3)$$

$$\delta_p = \frac{QR^3}{EI}\left(\frac{5}{4} - \cos\Psi - \frac{\cos 2\Psi}{4}\right) \qquad (5.2.4)$$

$$\delta_q = \frac{PR^3}{EI}\left(\frac{5}{4} - \cos\Psi - \frac{\cos 2\Psi}{4}\right) \tag{5.2.5}$$

$$\delta_q = \frac{QR^3}{EI}\left(\frac{3\Psi}{2} - 2\sin\Psi + \frac{\sin 2\Psi}{4}\right) \tag{5.2.6}$$

$$\delta_p = \frac{MR^2}{EI}(1 - \cos\Psi) \tag{5.2.7}$$

$$\delta_q = \frac{MR^2}{EI}(\Psi - \sin\Psi) \tag{5.2.8}$$

Ψ is once again the angle of the actuator arc length. Table 5.1 shows a comparison between the measured and predicted slopes of the curves relating the x- and y-direction tip displacements to the downward force due to added tip mass. Note that the slopes, or spring constants, here are taken about the zero displacement point. This is also known as the static equilibrium, or operating, point. Due to the crude method of measurement, the slope values calculated from data have about 10 % accuracy. It is difficult to obtain accurately the slope of the curve about its equilibrium point with only a few points. It should be stated that the arcs and arc numbers shown here correspond to the order in which the arcs were made. They start from the first one that was made, before the correct manufacturing procedure had yet to be devised. Arcs of sufficient piezoelectric performance quality were not produced until the fifth actuator. These numbers do not correspond to the arc numbers that are used in the three DOF experiment theoretical analysis. Figures 5.2 are graphical representations of this data and the two prediction methods. The results of the displacements due to a mechanically applied applied force are fairly accurate. The method developed in this section is much more accurate than that of the original method with an assumed semicircular arc shape. Slight intermediate improvements can be made on the original method by adopting one of the two philosophies (radial and circumferential definition of forcing or arc shape slightly deformed from a semicircle) separately to try and simplify the verification mathematics. Suitable results were not obtained, however, until the complete conversion to the new method was made.

Table 5.1: Comparison of methods used to verify the arc properties

Arc # (N/m)	Predicted Stiffness (N/m)				Measured Stiffness			
range	with shape correction		without shape correction		operating point ± 10%		whole ± 5%	
	K_h	K_v	K_h	K_v	K_h	K_v	K_h	K_v
1	1.28	1.38	1.60	2.04	1.36	1.26	1.42	1.19
2	1.50	1.78	1.66	2.12	1.29	1.52	1.30	1.15
3	0.54	0.64	0.79	0.62	0.58	0.61	0.35	0.58

The electrically induced properties of the piezoelectric arcs are not as accurately predicted. Although the horizontal displacement predictions due to an applied voltage are fairly accurate, the vertical displacements are not. The displacement-voltage relation is also noticeably nonlinear and hysteresis was observed. It is worth pointing out that the displacement-voltage relations are significantly closer to being linear away from the operating point of each actuator. For the vertical tip this is when the actuator contracts and has an effective arc angle of greater than π radians. For the horizontal tip displacement this is when the arc expands and has arc angle of less than π radians. This is a property that can be taken advantage of when designing arcs for a specific control problem. The good news is that the displacements are greater than those predicted. Although the shape corrected method of prediction developed in this chapter is not very accurate for the piezoelectric properties, it still better than the original one. Nevertheless, a more accurate method of the piezoelectric properties of a PVDF arc is desirable.

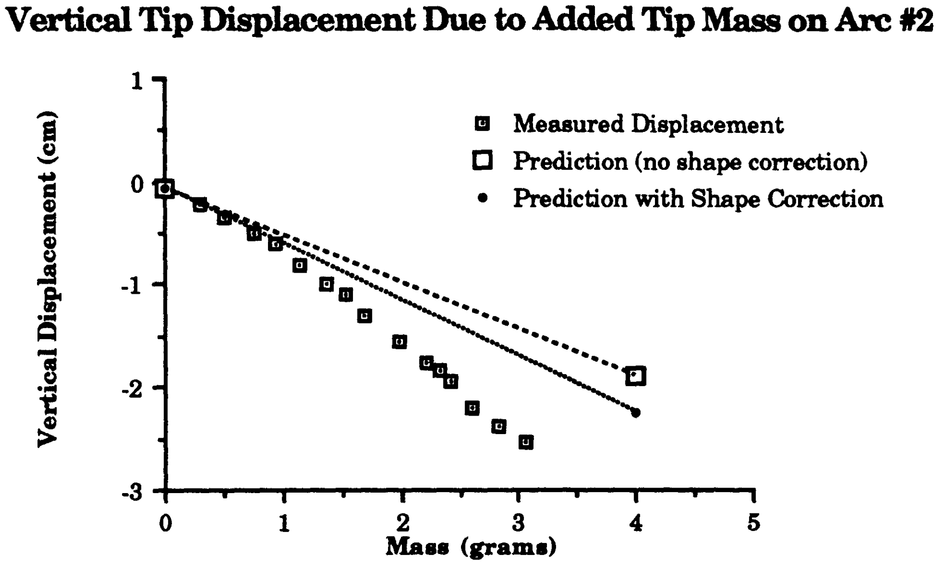
Vertical Tip Displacement Due to Added Tip Mass on Arc #2

a) Vertical displacement

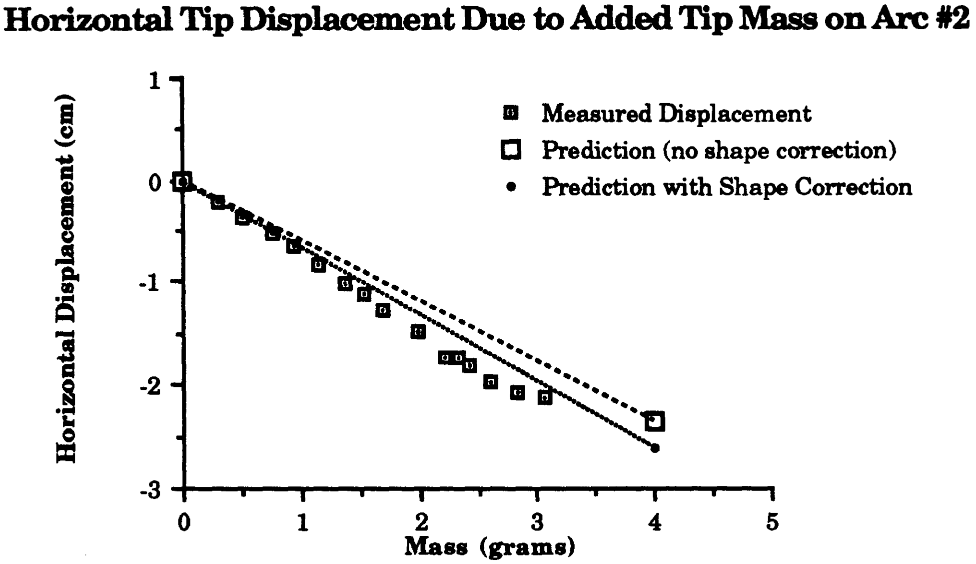
Horizontal Tip Displacement Due to Added Tip Mass on Arc #2

b) Horizontal displacement

Figure 5.2: The force-displacement relation predictions by the two methods of arc property verification plotted with some experimental data: a) Vertical displacement, and b) Horizontal displacement.

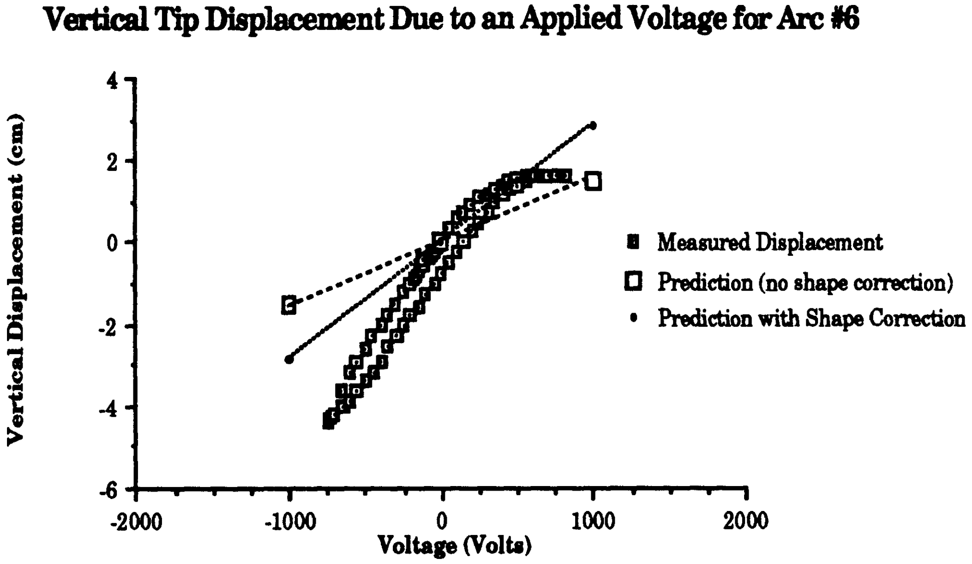

a) Vertical displacement

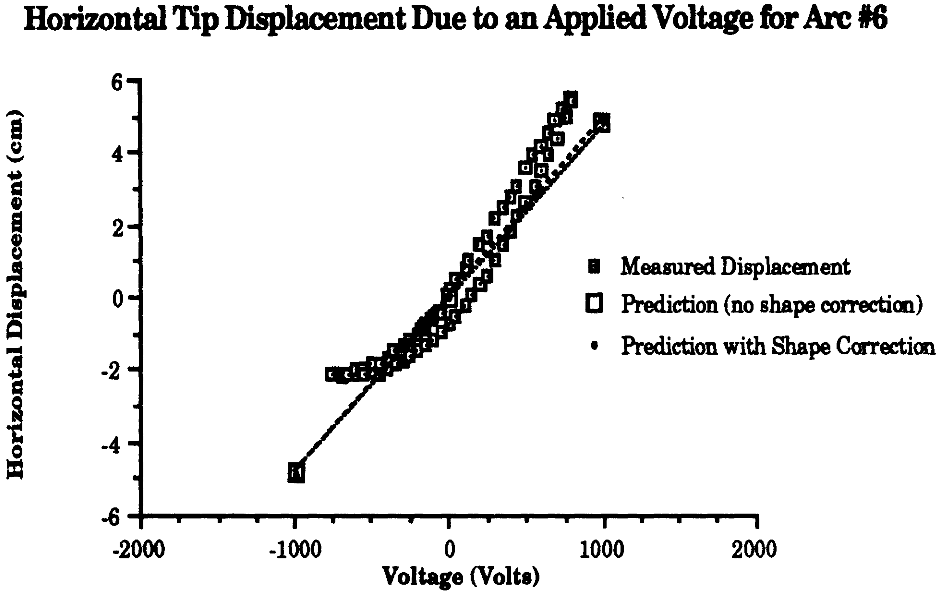

b) Horizontal displacement

Figure 5.3: The voltage-displacement relation predictions by the two methods of arc property verification plotted with some experimental data: a) Vertical displacement, and b) Horizontal displacement.

5.3 Actuator Grouping/Mounting Configuration Experimentation

A lot has already been said in the previous chapter about the experimentation conducted on node performance and the determination of its optimal mounting conditions. It is summarized here to solidify the reasons for taking the experimental design approach mentioned in Chapter 4. After the above single arc results, where the piezoelectrically excited arc obtained greater deflection levels than expected, the expectations of the ability to achieve or surpass nodal displacement levels predicted for the Sirlin and Laskin mounting conditions were high. Displacements of slightly over ± 1 cm were predicted but those of only + 3 mm and -2 mm were observed. The ensuing investigation resulted in the different types of mounting conditions that were introduced in Chapter 3, namely the use of a hinged end condition.

The node displacements were measured in two fashions. Initially, the set up was much the same as that of the single arc. The node was clamped so that the arcs were in a vertical position back to back. A light thin lexan sheet was placed across the top; and the arcs were clamped to the plate using cellophane tape. The same grid used for the single arc displacements was used to measure those of the node. It was under these conditions that the + 3 mm and - 2 mm displacements were observed. It was visually observed that, when displaced from the equilibrium point, the arcs were no longer of a circular arc shape. Since the clamped end conditions force the arc ends to have the zero slope and the distance between the two end points changes, the semicircular arc approximation quickly becomes inaccurate (Figure 5.4). Also, while in compression, the ends of the arcs just outside the clamps, known as the roots, will want to bend away from the radial center of the actuator. This is not possible when the PVDF arc is clamped directly to a flat surface. The root of the arc can only bend in one direction. The flat surface prevents the outward bending and stiffens the node. This explains the reduced displacement achieved when under compression.

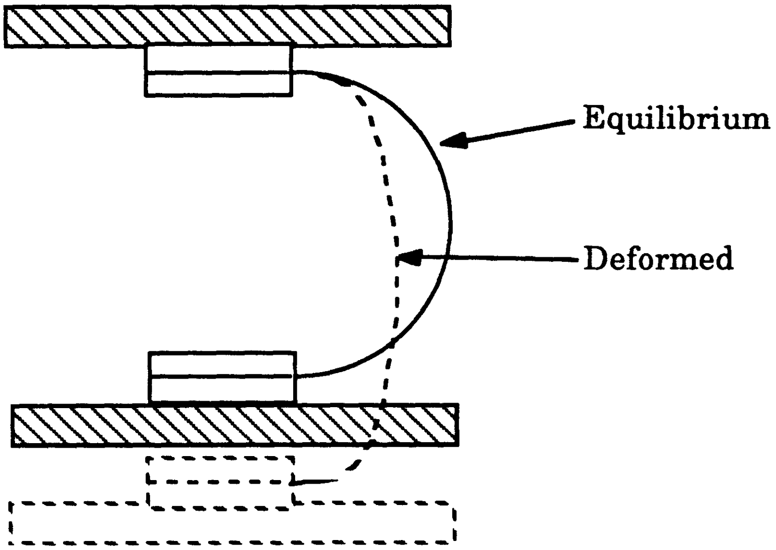

Figure 5.4: Clamped end conditions for the semicircular arc result in large deviations from the assumed circular arc shape at relatively small displacement levels.

Concern that the weight of the lexan sheet was compressing the arc excessively, making it stiffer, led to a horizontal node testing set up. The clamp was affixed to a heavy lexan plate and rotated so that the arc is operating in the horizontal plane. The other node end was affixed to another plate, this time hung on meter long piano wire to allow horizontal motion. The same stiffening effects were observed. In order to counter the compression stiffening effect described in the previous paragraph, the actuator tip was affixed to a stiffened piece of paper that was clamped to the lexan sheet. The paper was folded over twice so that the arc could be clamped to the paper at the fold and be displaced from the flat surface. Displacement increased to over ± 5 mm. Upon observation it was discovered that the extra displacement was due to the hinging of the paper at the fold near the actuator tip. This prompted the development of the truly hinged actuator described in the previous chapters. The hinge is shown in Figure 5.5. It consists of two pieces of thread. The thread is affixed perpendicular to the edge of the end of the arc, one on each side and at the same location. The two pieces of thread are then affixed to the opposite sides of the sheet of material it is to be hinged with. This hinge has been sufficient for the tests performed to date. Two hinges at the end of the actuator arc ensure that the arc end will rotate about an axis defined by the line between the two hinges. This is comparable to having multiple hinges on a door so that it swings open into the room and does not fall over while rotating on a single hinge point. In our tests the material the arc is hinged to is a thin sheet of mylar. This mylar sheet is then mounted in a clamp. With the addition of a lexan block between the flat mounting surface and the clamp, the mounting points of the PVDF arcs are displaced from the mounting surfaces. The arcs are free to bend or rotate without any interference from the mounting surfaces.

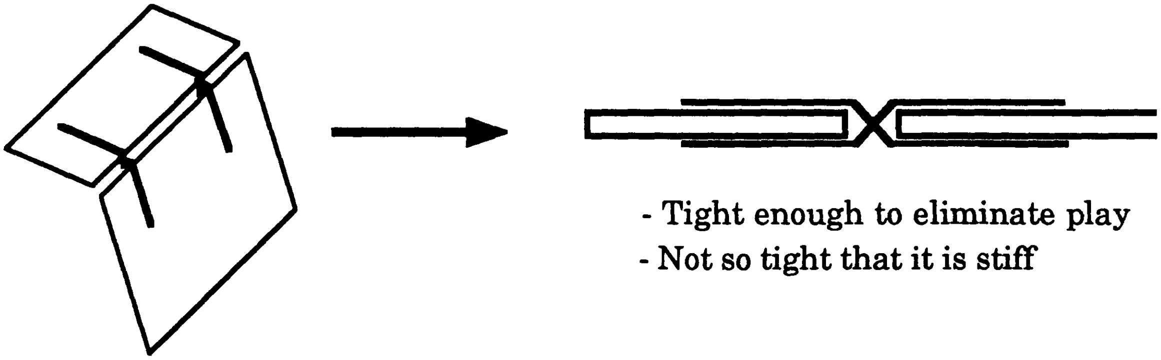

- Tight enough to eliminate play
- Not so tight that it is stiff

Figure 5.5: The hinged end condition for a PVDF arc.

All of the hinged mounting configurations discussed in Chapter 3 were implemented to some degree. With hinges on one end, displacements of ± 0.75 cm were achieved. If hinges and arcs of arc angle greater than π radians are used, the actuator can potentially be closer to being linear. One double hinged actuator with an arc radius of 2.5 inches and arc angle of $3\pi/2$ radians was attempted and displacements of approximately 1 cm were observed; but this smaller two hinge configuration was abandoned because of the massive, relative to the local arc mass, lead connection material on the active section of the arc. This extra mass should be accounted for in the equations because it has the potential to introduce internal actuator modes in the desired control bandwidth. The durability and quality of the electrical connections is also very much in question. In order to take full advantage of the piezoelectric properties of the PVDF Film, it must be possible to apply 800 volts across the arc layers via the single strand enamel coated copper wire used as leads. If regular wire leads are used, the mounting condition of the arc begins to have a noticeable torsional stiffness, possibly negating the effects of the hinge. The double hinge actuator's development is a direct result of these concerns. It allows essentially free rotational and lateral motion of the payload about its end. Another mylar sheet is placed in between the arc end and the mylar sheet clamped to the payload. It is hinged to both the arc and the clamped sheet of mylar at opposite ends. This middle sheet acts as a link. Displacements comparable to that of the two hinge arc, the arc hinged at both arc ends, were demonstrated. A node using the same arcs was assembled utilizing these mounting conditions. Displacements of greater than ± 1.5 cm resulted. This is closer to the magnitudes promised by the original clamped-clamped analysis. Unfortunately, since the tip of the double hinge arc is partially free to move in two degrees of freedom, the arc acts like a clamped-free beam and its first internal bending mode was observed to be under 5 Hz. It was decided to go with a mount of six single hinge actuator arcs of the original arc dimensions since the necessary displacement (2.5 mm) had already been demonstrated and it was deduced that the three node configuration outlined in Chapter 4 be of sufficient stiffness. The minimum allowable mount stiffness is actually a little over three times umbilical stiffness of 2 N/m. This is not the 20 N/m target described earlier but sufficient for the problem as described by Jones et al.[4] The displacements will be less than the 0.75 cm observed for a single node because the x-direction node will have to push against the two nodes on the adjacent sides controlling the rotation and y-direction translation. A single hinge arc should satisfy the minimum stiffness and displacement requirements for the six arc three degree of freedom system.

5.4 Three Degree of Freedom Experimental Results

The three DOF experimental results were quite successful. The response transfer functions to both the mechanical and piezoelectrical excitations were predicted with a fair amount of accuracy. Transfer functions were measured by using the Fourier analyzer. A random sinusoidal output signal was produced by the analyzer software and the signal was amplified to an appropriate level before reaching the experiment and driving the specific excitation unit. When the shakers, which move the outer box and thus simulate the motion of the spacecraft, are driven, the signal goes through the Crown amplifiers and the level of excitation is adjusted so that the range of motion is approximately the ± 2.5 mm motion limit specified in Chapter 2. When the piezoelectric polymer arcs are driven, the signal is amplified by the Kepco amplifiers which have a gain of 100. This gain is necessary in order to achieve the maximum voltage allowed by the PVDF arcs, 30 volts per μm of layer thickness. For 28 μm film this is 840 volts. Since there was a lot of noise transmitted to the accelerometers above 8 Hz, all signals seen by the analyzer were conditioned using a low pass filter with a corner frequency of 6 Hz to prevent the magnitude of these high frequency signals swamping out the low frequency data of interest. The Fourier analyzer analyzes both the accelerometer output and signal generator output signals to determine a transfer function for the frequency range chosen. The measured transfer functions from excitation to sensor output are plotted and then placed in matrix format for the next three pages. The predicted transfer functions were produced using the final measured experimental physical dimensions in Table 4.1 and are plotted on the same graphs to allow easy comparison between theory and practice. Please make note that the shaker and accelerometer displacements and accelerations are not the same as those of the outer or inner boxes as expressed in their x, y, and θ degrees of freedom. The transfer functions here were predicted using additional transformations to obtain the body motion at the accelerometer and the stinger locations. The accelerometer transformation from the payload motion can be seen as part of Figure 4.2.

Figure 5.6 shows the acceleration of each accelerometer caused the by the acceleration of a particular shaker head. The measured transfer functions bear good resemblance to the predicted ones; and, once again, the mechanical properties of the arcs can be predicted fairly reliably. The only noticeable difference is that the y-direction translation and the rotation degrees of modes have a 0.03 Hz shift upwards in frequency. This implies that the mount may be stiffer in these directions than anticipated. Unfortunately, acceptable experimental data was not achieved below 0.1 Hz. This is indicated by the sample coherence graphs in Figure 5.9. Coherence

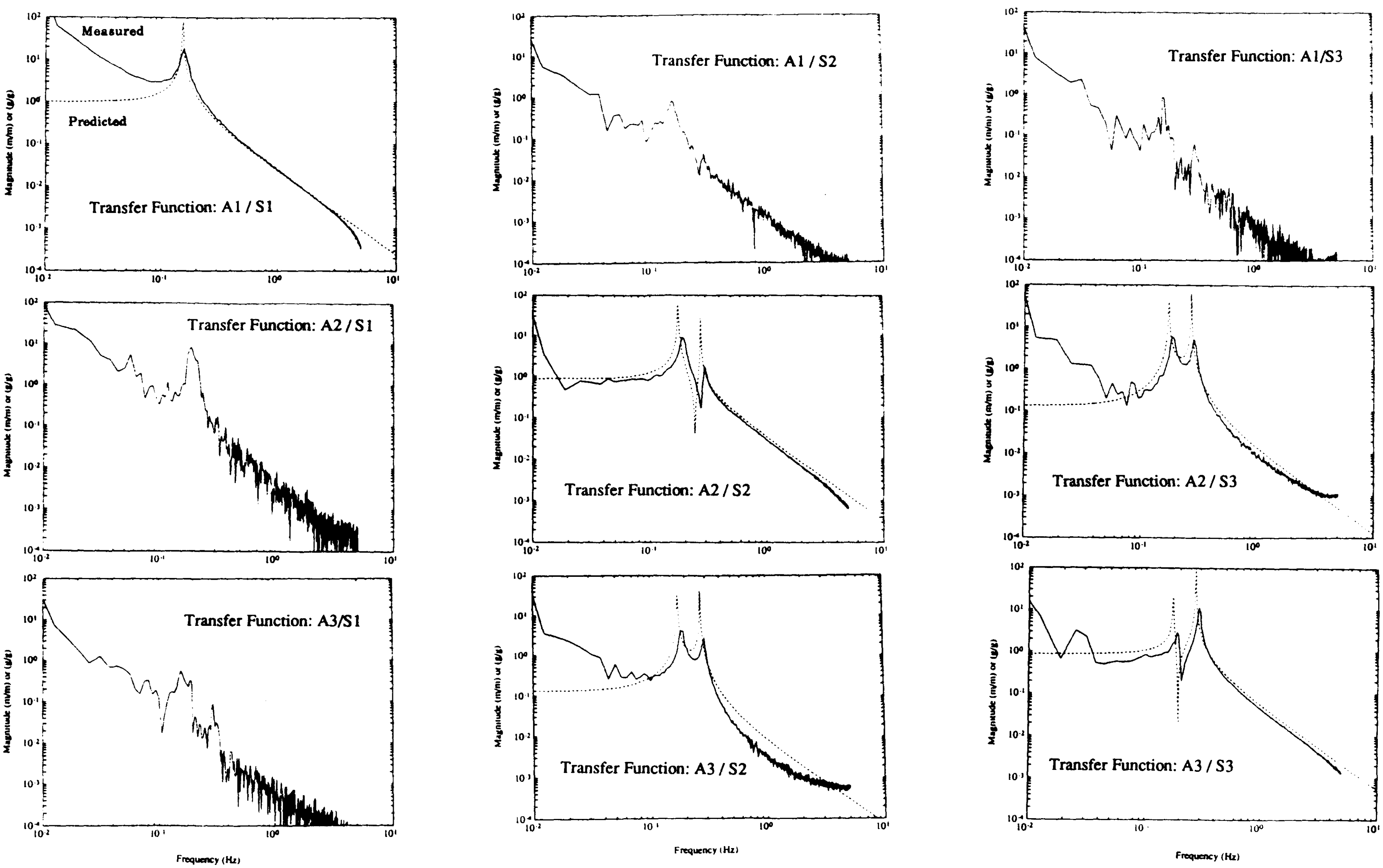

Figure 5.6: Matrix of transmissibilty transfer functions: Shaker head motion to accelerometer motion.

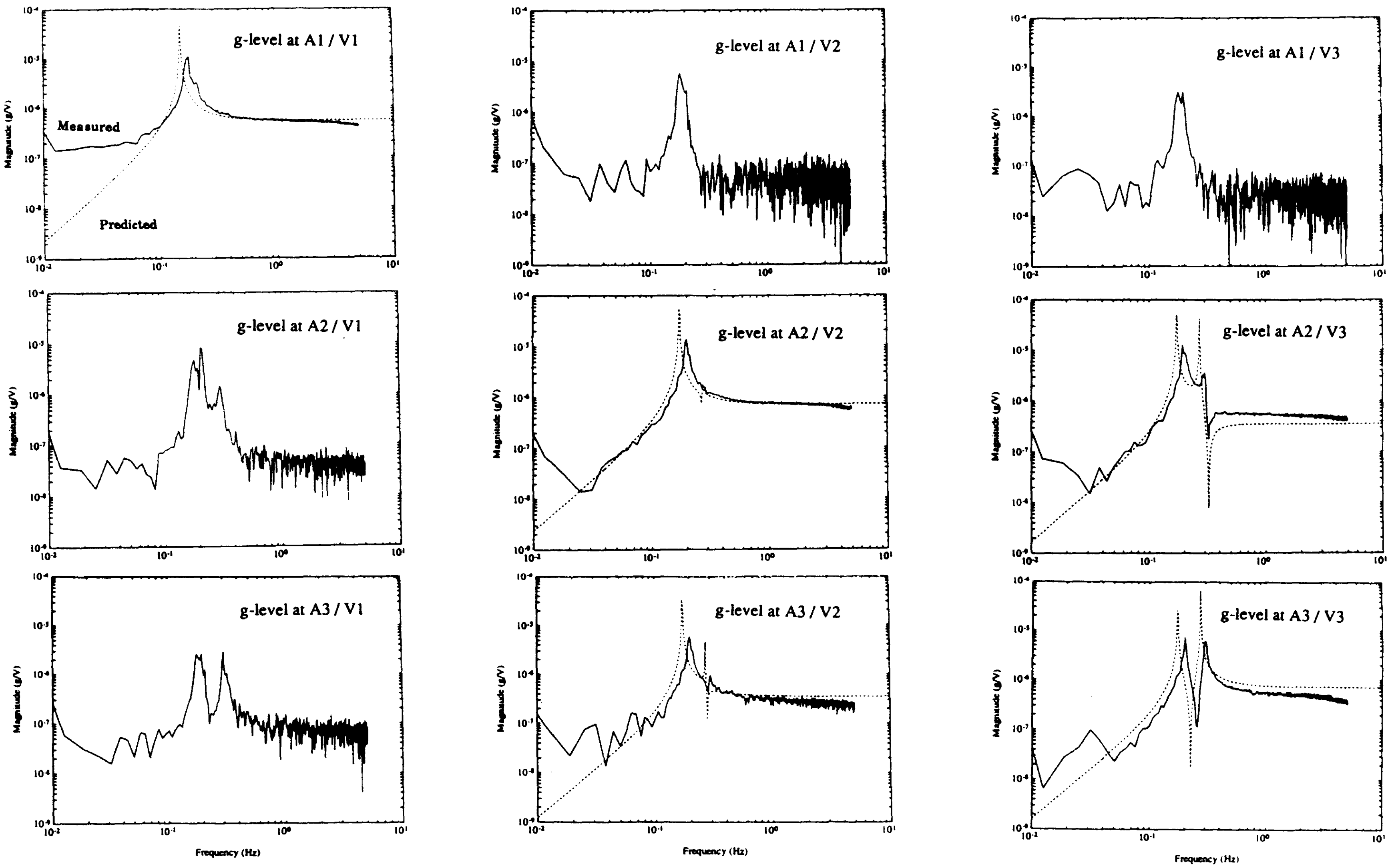

Figure 5.7: Matrix of transfer functions: Actuator group applied voltages to accelerometer acceleration in g's.

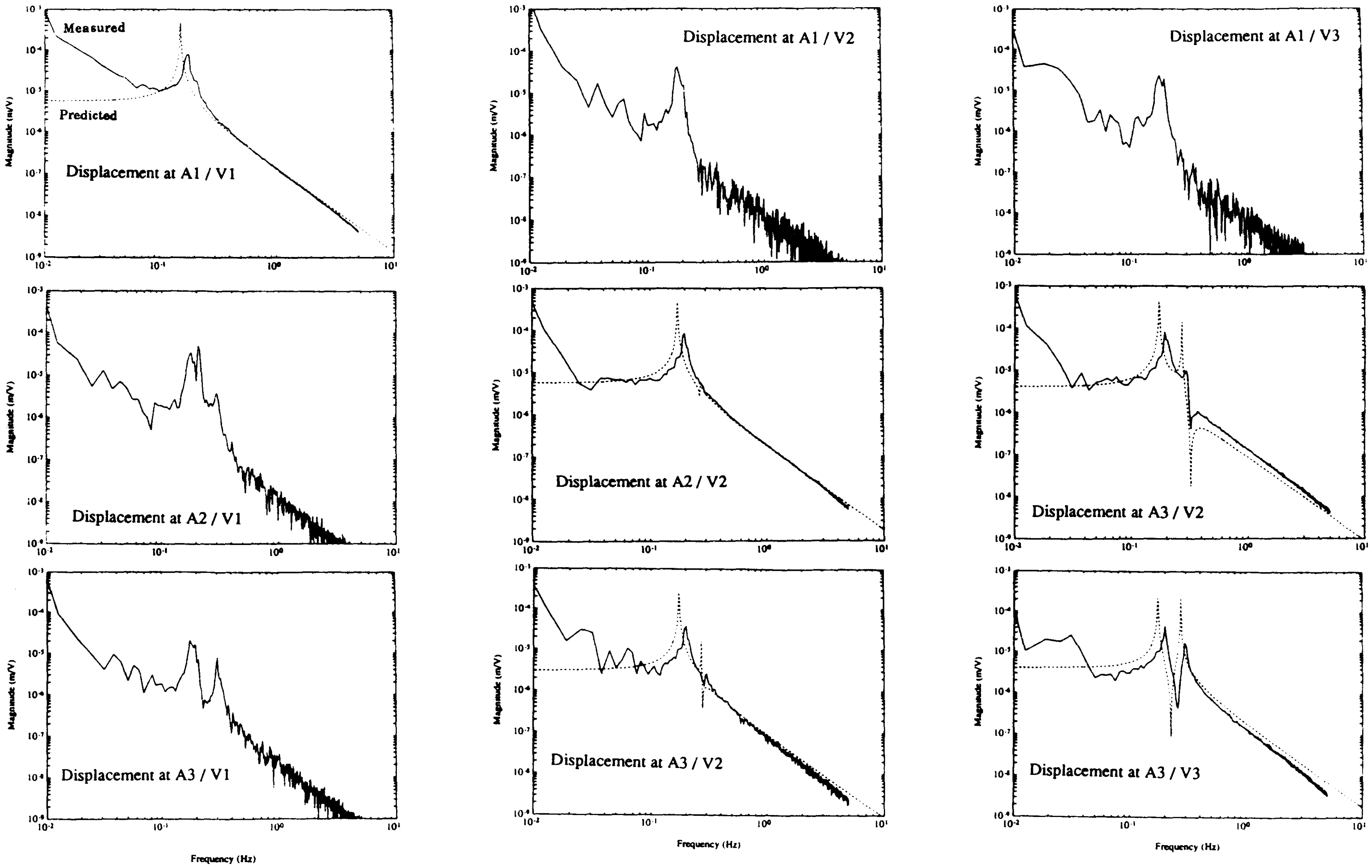

Figure 5.8: Matrix of transfer functions: Actuator group applied voltages to accelerometer displacement.

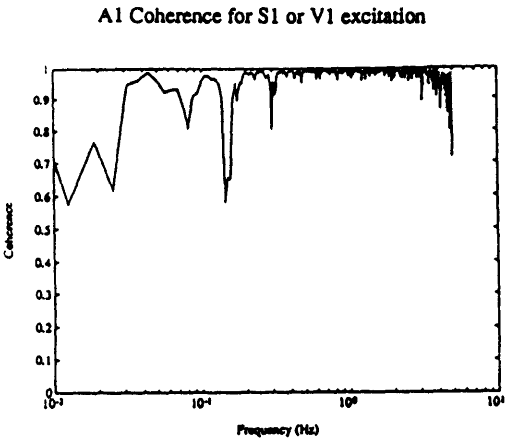
A1 Coherence for S1 or V1 excitation

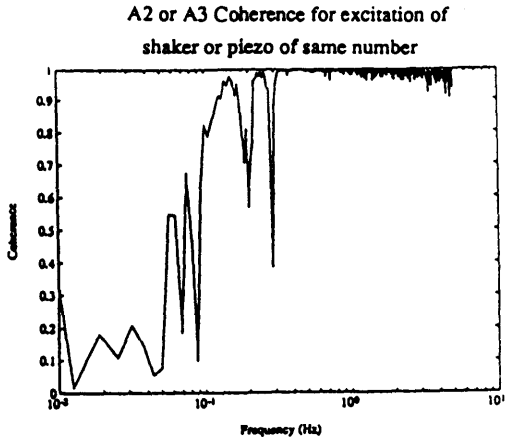
A2 or A3 Coherence for excitation of shaker or piezo of same number

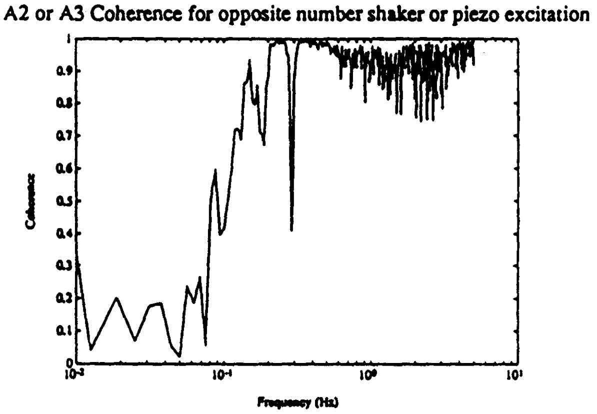
A2 or A3 Coherence for opposite number shaker or piezo excitation

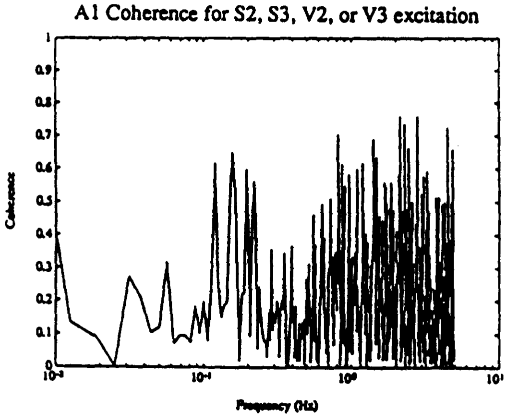
A1 Coherence for S2, S3, V2, or V3 excitation

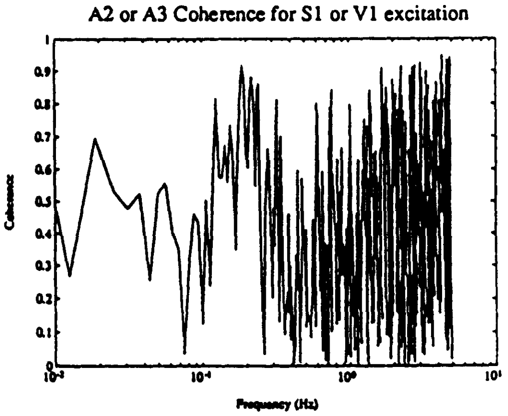
A2 or A3 Coherence for S1 or V1 excitation

Figure 5.9: Typical measured coherence functions.

is an indication of whether the response is caused by the excitation.[33] A coherence of 1.0 indicates perfect causality between excitation and response. A coherence of 0.0 indicates no causality. A good rule of thumb for quality of data is given by Ewins where he states that a coherence of above 0.9 is necessary to indicate a direct one to one relationship between the excitation and the response. As can be seen in the graphs of the measured transfer functions, the noise floor of the experiment is only an order of magnitude or two below the transfer function at higher frequencies. This noise dominates below 0.1 Hz. These curves also show that near resonance, the coupling between the x-direction DOF and the other two DOFs may be too large to ignore in the actual control implementation. Physically this coupling is probably caused by nonuniformity in the manufacture of the actuator arcs and possibly their mounting locations. The exact cause or causes of apparently insufficient acceleration resolution at low frequencies is unknown. It is suspected that either the specific accelerometer units used in this experiment do not resolve to a sufficient level (a calculated risk taken early in the experimental design) or more likely that data is being swamped out by the accelerometer output outside the 0.01 Hz to 0.1 Hz band. Lab disturbances, probably air currents, produced accelerometer excitation usually the equivalent of slightly under a milli-g. This makes resolution below a μg extremely difficult. The air table also had to be balanced after every couple of experimental runs in order to keep the inner box and the puck centered on the air table. This suggests dimensional instability either in the air table, the desk upon which it rests, or the building. Although the frequency of this instability is essentially static (lower than 0.01 Hz), the bias level of acceleration caused by the tilting of the table, and thus accelerometers, can be enough to swamp out sub μg variations. If the tilt is enough to move the inner box more than ± 2.5 mm, this translates to a tilt angle on the order of a couple of milliradians. This produces a bias acceleration of a couple of milli-g. The analyzer does not have a high pass filter capable of suppressing signals below 0.01 Hz, thus making it hard to resolve below a μg. The experiment already pushes the low frequency limit of the analyzer. So it can not be used to characterize the noise below 0.01 Hz. The next stage of experimentation to be conducted beyond that described in this document should address this issue of insufficient low frequency resolution. Until the low frequency accelerometer resolution problem in the lab is solved, good data with the full 100 kg mass is impractical to achieve. It was not attempted because the resulting resonant frequency would be below 0.1 Hz. The total mass, 7 kg, of the empty box and the puck was used instead. This brought the modal frequencies above 0.1 Hz. It should also be noted that when the air table was not balanced so as to keep the inner box within 0.5 cm of the center of the air table, the resonant frequencies of the system shifted. This shows that the actuators are once again extremely sensitive to their equilibrium shape. This should not be a problem in orbit since the 100 kg facility only moves a 10 N/m spring 0.1 mm while under the influence of a μg.

The piezoelectrically induced response compared surprisingly well given the mediocre performance in predicting the voltage-displacement relation for the tip of a single clamped arc. The matrix of transfer functions from applied voltage to accelerometer acceleration are shown in Figure 5.7. The accelerometer location displacements are also deduced by dividing the above transfer functions by the frequency, in radians, squared. They are shown in Figure 5.8. The predicted response in the x-direction, measured by accelerometer 1, is actually fairly accurate except for an eigen-frequency shift of approximately 0.03 Hz. The high frequency asymptote of the induced acceleration for an applied voltage in this direction appears to be ± 0.5 μg/V, a hair under the predicted value. The low frequency asymptote appears as if it would follow the predicted curve if acceptable data under 0.1 Hz were available. The displacement implied by these asymptotes and the application of 800 V is a little under ± 5 mm.

The y-direction accelerometer responses of accelerometers 2 and 3 to the piezoelectric excitation also fared very well. This time the frequencies did not perceptibly shift to a higher magnitude when compared to the purely mechanical excitation. The response to the left most arc pair, piezoelectric arc voltage, V2, was of slightly lower magnitude than expected. A low frequency displacement asymptote of ± 6 μm/V was expected at accelerometer 2 while ± 3 μm/V was expected at accelerometer 3. Displacements of approximately ± 4.5 μm/V and ± 2 μm/V, respectively, were observed. At 800 Volts the contribution of V2 averages out to ± 2.4 mm at the box center. This displacement is consistent with the high frequency acceleration asymptotes of about ± 0.6 μg/V and ± 0.3 μg/V. If these accelerations are converted into m/s^2, multiplied by the total mass of the inner box and puck, forces of approximately ± 42 μN/V and ± 20 μN/V result. Since at high frequencies an applied force produces a moment about the center of gravity, there is a positive acceleration on one side of the box and a negative one one the other side; and if the center of gravity is close to the center of body, the translational acceleration at both locations is the difference of the two accelerations divided by two. The force at 800 V, 0.016 N, when applied to a spring of mount equivalent stiffness produces displacements of approximately ± 2.4 mm. For the middle piezoelectric arc grouping, V3, the displacement is more difficult to ascertain due to the closeness in magnitude of the high frequency accelerations transmitted to each accelerometer. It seems to be about ± 1.5 mm when the low frequency displacement per volt asymptotes are noted and transformed to the center of body of the box. Together, the two sets should be capable of allowing the necessary displacement requirement, ± 2.5 mm, of the inner box in the y-direction. Although these transfer functions roughly predict a displacement in excess of the ± 2.5 mm required in each direction, the actual distance will be smaller due to the non-linear characteristics exhibited by these piezoelectric arcs in the previously in this chapter. In order to verify that the achievable displacement is at least ± 2.5 mm, 800 V was applied to the arcs at frequency of no more than 0.01 Hz. The full range of motion was measured with a ruler and observed to be a little over 5 mm, or ± 2.5 mm. Unfortunately, the accuracy of this value is not guaranteed because of the inner box resonant frequency motion excited by the lab noise was probably half of that in magnitude. This excitation also prevents a sufficiently accurate point by point data recording of the displacement of the inner box for a specific applied voltage. A displacement voltage relation like the that demonstrated for a single arc is at present unattainable. The two main intermediate conclusions are that the ± 2.5 mm displacement requirement appears to be barely satisfied and the displacement to voltage relation is most likely non-linear, although the characteristic bending of the resonant peak was only observed in accelerometer 1 and thus the x-direction.

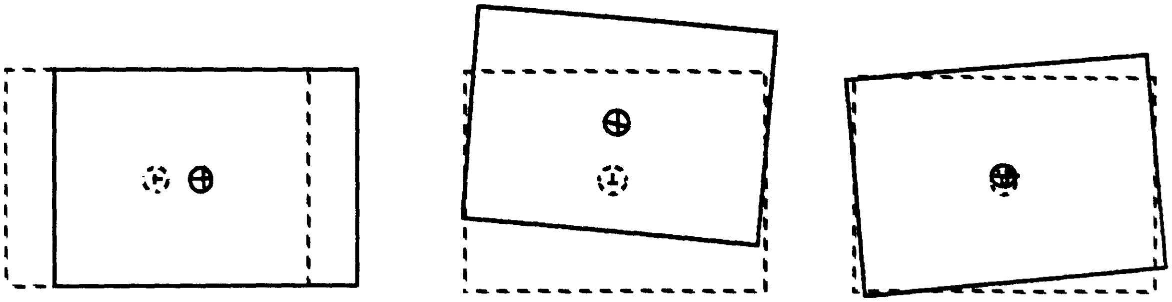

a) Mode 1 b) Mode 2 c) Mode 3

Figure 5.10: Mode shapes of the inner box motion.

The apparent pole-zero cancellations evident when V2 is excited can be explained by determining the effective pivot points of the inner box at each resonant mode. To aid in the visualization of this problem, the mode shapes at the mount resonances are shown in Figure 5.10. If all mount arcs are identical, the right side, or positive x-direction, of the mount is stiffer in the vertical, or y-, direction, than the left side. This results in a low frequency rotational pivot point 0.5 m to the right of the center of body for mode 2, the first of the two coupled modes. This is the source of the coupling between the angular and y translation motions. If the leftmost arc pair is stiffened, this pivot point moves further to the right until the system is balanced in the y-direction motion and there is no coupling or pivot point. At frequencies above the first of the two coupled resonant modes, the second mode will tend to dominate and the pivot point moves along the x-axis to a new location. In the case of identical arcs, it is 3.5 cm to the LEFT of the center of body of the inner box. The fact that the pivot point moves to the left of the center of body is counter intuitive, but nonetheless true. If the leftmost actuator is stiffened, the system is closer to being balanced in the y-direction motion and the pivot point moves toward the center of body. At frequencies beyond the last resonance, the motion of the inner box becomes that of a freely floating mass that translates and rotates about its center of gravity. Since neither accelerometer response has a peak at the frequency of the second of the two coupled modes, the second pivot point must have moved near to the net pivot point resulting from the forces of actuator group

2. This actuator group has been deployed in such a manner that it can not excite this last mode. This is why the second resonant peak does not show up in the responses when actuator group number 2 is excited. If the node had been conceived in a front-to-front format, the horizontal movements of each arc would add to the rotational motion of the system. Instead they subtract from it and the result puts the effective pivot point closer to the system center of body and the modal pivot point. This may not have been predicted in the analysis because of inaccuracies in measuring the physical parameters or a stiffening of the arc in its actuation mode. A stiffer arc may have moved the pivot point to a new location. When the arcs are excited piezoelectrically, their shape changes. If voltage is applied to the arc so that it expands when unopposed, the ends will bulge out and the middle creep in for hinged end conditions. As was seen in the preliminary nodal studies, this shape change has the effect of producing a mechanically stiffer arc. If actuating an arc does make it stiffer, when the middle shaker group, V3, is excited, both pivot points will be moved slightly further left. But since neither pivot point is near the location of the rotational center of the applied force, the resonant frequencies and the zeros will not cancel each other. A zero occurs when the pivot point passes over the accelerometer location. Care must be taker to avoid these observed cancellations. In order to control a mode, an actuator must be able to excite it. Fortunately, in this experiment, another actuator group can fulfill this need.

The final measured mount characteristics are listed in Table 5.2.

Table 5.2: Summary of key characteristics of the three DOF piezoelectric arc active mount

X direction stiffness	8 N/m
Y direction stiffness	11N/m
X and Y direction displacement capabilities	> 2.5 mm
X direction force capability	34 µN/V
Y direction force capability	62 µN/V

5.5 Summary

In this chapter the properties of single arcs, nodes, and that of the experimental three DOF microgravity mount experiment were experimentally tested. The pure mechanical properties of the PVDF arcs compared well with theory. However, due to the sensitivity of the properties of an actuator to small changes in its static equilibrium shape, a more detailed analysis became necessary. Once these shape corrections were made, the mechanical properties of an actuator linearized about its equilibrium, or operating point, were very accurate. Although the piezoelectric properties for a single arc were highly nonlinear and the linearized predictions at the operating point were not very accurate, the three DOF experiment open loop characteristics compared quite favorably with prediction.

The sensitivity to changes in actuator shape is further exemplified in the experimental iteration of the node design. When the arc is clamped at both ends and deflected from its equilibrium position, the actuator quickly loses its circular arc shape. Since its arc length is essentially constant and the distance between the two mounting devices changes, a circular arc shape is quickly lost under the clamped end conditions. A hinged end condition allows the arc to stay closer to its original circular form but changes the angle of the arc length. Although the relationship does not become completely linear, the nonlinearity is not severe enough to prevent the required mount displacement from being achieved. A two hinge actuator with an angle of greater than π radians would be the ideal actuator arc. It would be fairly linear in the displacement range of interest; and since two hinges are used, the horizontal stiffness of one node would be negligible compared to the vertical stiffness of one on an adjacent side. Unfortunately problems still exist in the manufacture of an acceptable unit. The sensitivity of the PVDF arc mount to small changes in its equilibrium position also showed up in the experiment. If the equilibrium position changed 0.5 cm, changes in the resonant frequency were noticed. But since the change in location of the microgravity facility in a spacecraft should not be more than ± 0.1 mm, the equilibrium shape change should not be large enough to matter in LEO.

The final design of the PVDF active mount exhibited the minimum requirements of a microgravity mount, and surprisingly did not succumb to all of the inadequacies of the single arc piezoelectric properties modelling. A displacement of ± 2.5 mm was exhibited with a mount stiffness at least three times bigger than the minimum umbilical cord stiffness. The measured mechanical properties of the actuator were close to prediction, while the measured piezoelectric excitation levels were a little low in magnitude. The resonant frequencies were off by about 0.03 Hz but the general transfer function shapes were the same as those predicted. The only clear evidence of nonlinear behavior in the transfer function plots is the stiffening bend in the resonant peak of the x-direction response to the actuator group V3. Nonlinear behavior is also implied with the maximum displacement measured at a little over ± 2.5 mm; but the value predicted from the low and high frequency per volt asymptotes of the transfer function data translates to ± 4 mm at 800 volts. The piezoelectric node toolbox is sufficient to achieve a design with the gross characteristics of a microgravity isolation mount. Unfortunately, the measured level of excitation was not as high as that predicted. This should be taken into account when it is being used.

Chapter 6

Conclusions and Recommendations

6.1 Conclusions

This publication documents the successful physical development and implementation of a laminated polymer piezoelectric actuator and applies it to the microgravity isolation problem in the form of laminated PVDF arcs. PVDF laminated actuator hardware has been built that has the potential to provide scientists and manufacturers with the low acceleration environment needed to achieve their goals. The mount was constructed for a three DOF laboratory demonstration and adheres to the basic requirements of the microgravity mission intended for implementation on the space station as outlined in Chapter 2. The constructed mount can travel ± 2.5 mm and has a stiffness of 8 N/m in one translational direction and 11 N/m in the other. This stiffness is more than the minimum required value of three times the 2 N/m minimum stiffness of the umbilical cord that functions as a supply line for the facility. Both of these stiffnesses are extremely low. The environment in LEO provides unavoidable near-static forces and torques on a spacecraft that amount to a minimum level of a μg at frequencies near orbital rate of 10^{-4} Hz. At frequencies above 0.01 Hz anticipated man made disturbances eclipse this μg level. An envelope encasing the possible disturbances increases at a rate of 40 dB per decade of frequency until it reaches a plateau of 0.1 g. Since the mount resonant frequency for a 100 kg processing facility on the minimum umbilical cord stiffness prevents purely passive isolation, the basic single axis control approach envisioned here is that of a semi-active soft mount. The mount is kept as soft as possible and takes advantage of its active characteristics in the frequency range where further isolation is needed.

This document also presents some analysis tools for working with the design of a laminated polymer piezoelectric arc actuator. The purely mechanical arc properties show excellent adherence to the developed theory. Unfortunately, the developed piezoelectric arc theory is only good enough for an approximate design. There is significant nonlinearity and a noticeable hysteresis in the measured displacement-voltage relation for a single arc with an arc angle of π radians. The nonlinearity is due purely to the geometry of the problem and can be significantly reduced by changing total arc angle of the actuator. This angle depends on the desired direction of arc actuation. If the arc is clamped to a flat surface, an arc angle of less than π radians will give a fairly linear voltage displacement relationship in a direction parallel to this surface. If the arc has a greater angle, the perpendicular displacement will be closer to being linear. It was also noticed that the clamping of an actuator arc end severely restricts its motion. The actuator quickly deviates from an arc of circular arc shape, which stiffens the actuator. A hinged end condition was developed to solve this problem. This extended the range of motion of an actuator configuration, a node, consisting of two back-to-back actuator arcs with one end mounted to each surface. Hinged end conditions should be used whenever possible. If certain configurations of hinges are used, the lateral stiffness of the actuators can be made negligible compared to that of the vertical. If an actuator has noticeable stiffness in a degree of freedom in which it is not actuating, the mount is unnecessarily stiffened. This reduces the range of motion capability of the mount. Various combinations of clamped and hinged actuators are analyzed in Chapter 3. The analysis of the piezoelectric excitation properties of the actuators developed in this document are sufficient for approximate design purposes and serve as a general design guide to the dimensions and properties of such a system. Due to inaccuracies in the prediction of the level of piezoelectric excitation, the level of control force can not be predicted with high accuracy. This quantity can not be known until the response characteristics of final model are experimentally measured. The designer should also be careful to make sure that the mount is balanced so that there is as little coupling of motion between degrees of freedom as possible. As demonstrated in the experimental results sections, the modes of the system are much easier to characterize when coupling is absent. Arcs may also stiffen slightly when actuated. This should be taken into account if delicate balancing is to be performed. If the designer is careful, the undesirable characteristics descrubed above can be minimized through this custom actuator design.

Closely tied to the development of the PVDF arc actuator, for use in the microgravity isolation problem, is the design of the experiment needed to demonstrate it. An experimental set up was devised that mimics the microgravity environment at frequencies between 0.1 Hz and 5 Hz. The key components are the air table, upon which a puck carrying the payload rests, and the Sundstrand Q-flex accelerometers. Since the three DOF experimental set up described in Chapter 4 does not sufficiently mimic the microgravity environment at frequencies below 0.1 Hz, the properties of the PVDF actuator mount were verified using a smaller mass, approximately 7 kg, to move the modal dynamics into the frequency range where they can be measured. Unfortunately, it is not clear from where the low frequency experimental noise is coming. The experience in the search for and design of the sensors and experimental suspension chosen yields valuable related information that is reported here. If the noise turns out to be that of the accelerometers, it may be necessary to revert to soft force transducers between the actuators and the payload. The implications in making this design change are discussed in Appendix B.

Although a control experiment has not been successfully completed, the laminated piezoelectric actuator has joined the ranks of the magnetic actuator as being shown to be capable of achieving the performance requirements of an actuator in a microgravity mount.

6.2 Future Work and Recommendations

As implied in the previous paragraph, the future work of immediate necessity is that of fixing the experimental suspension so that it mimics the microgravity environment of LEO down to at least 0.01 Hz. This involves time consuming low frequency characterization of the immediate lab environment at frequencies immediately below 0.01 Hz and the construction of a high pass filter to keep accelerometer noise at lower frequencies from swamping the sub μg resolution desired. The Fourier analyzer presently in use has been pushed to its low frequency limits. Additional help is needed in the form of the previously mentioned filter or the acquisition of new data acquisition hardware which has the desired properties. Perhaps one will have to revert to sinusoidal testing. If the noise level in the accelerometer signal is not caused by some dimensional instability of the lab set up but by the accelerometer noise itself, a new accelerometer will have to be designed using the approach outlined in Appendix B.

The arcs eventually used in this experiment are by no means in the optimal shape or configuration. For example, late in the project it was noted that the Sirlin and Laskin back-to-back node does not produce as much moment as a front-to-front node. This resuled in one actuator grouping not being able to excite one of the two coupled modes. When the nodes are back-to-back, differential actuation of the two arcs provides motion in the negative x-direction when a positive angular motion is produced. This linear translation at the side of the payload becomes a rotation of the opposite direction about the payload center and is counter productive. At present, it seems that an arc of arc angle greater than π radians hinged at both ends would be best for microgravity mount as configured here. The change in arc angle produces a node of better linearity. It also allows a greater range of motion due to less restrictions and has the added characteristic of an apparently negligible horizontal spring stiffness. Each node only stiffens the mount in the degree of freedom it is controlling. Careful actuator design using these properties will yield an easier to implement and more efficient actuator. However, before the two hinge actuator arc can be implemented, the problem of successfully providing a high voltage, 800 V, electrical connection to the arcs without adding too much mass or root stiffness must be solved while simultaneously providing enough insulation to prevent electrical arcing.

An alternative approach to the laminated PVDF actuator that takes advantage of many of the above design suggestions is shown in Figure 6.1. Flat tapered laminated beams are used as the actuators. They are clamped to the mounting surfaces of the spacecraft and then attached to the payload by way of a hinged toothpick-like linkage system. The hinges act as ball joints allowing the arcs to actuate in a single chosen direction without adding stiffness in any of the others. This is comparable to the double hinge actuator. It allows for a sufficiently soft mount in all degrees of freedom, cuts down on the coupling between the different modes, and makes the equations easier to analyze than the arcs. The flat beams also take up less space to allow a greater size payload inside a given volume. In addition, the hinges are linked so that the clamped free bending modes are not excited and the internal modes of the mount are not within the control bandwidth. The problem of the electrical attachment of the actuator with hinges at both ends need not be solved here; so no new technology development is needed. This microgravity mount concept has the potential to eliminate most of the undesirable characteristics noticed in the present set up.

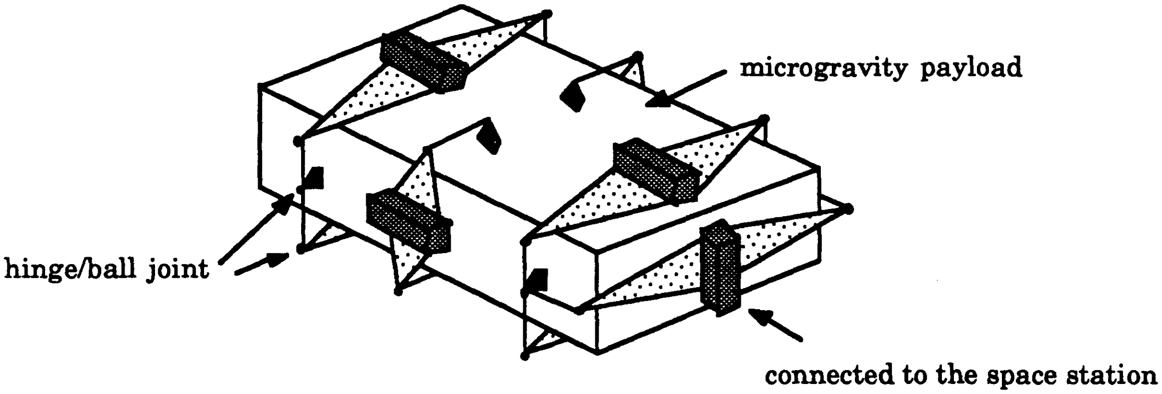

Figure 6.1: A future PVDF laminated actuator mount. Tapered beams cantilevered to the space station are used instead of arcs.

References

1 Tiby, C., and D. Langbein, "Allowable g-levels for Microgravity Payloads," Report of a study performed under ESTEC contract no. 5504/83 by Battelle Institute, Frankfurt (1985).

2 Laskin, R. A. and S. W. Sirlin, "Future Payload Isolation and Pointing System Technology," *Journal of Guidance, Control, and Dynamics*, Vol. 9, No. 4, July/August, 1986, pp. 469-477.

3 Laskin, R. A., et al., "NASA Office of Space Science and Applications Study on Space Station Attached Payload Pointing," AIAA paper 88-4105-CP, 1988.

4 Jones, D. I., A. R. Owens, and R. G. Owen, "A Microgravity Isolation Mount," *Acta Astronautica*, Vol. 15, No. 6/7, pp. 441-448, 1987.

5 Allen, Terry S. et al., "FEAMIS: A Magnetically Suspended Isolation System for Space Based Materials Processing," *Proceedings of the Annual Rocky Mountain Guidance and Control Conference*, American Astronautical Society Paper AAS 86-017, 1986, pp. 119-128.

6 Fenn, R. C., J. R. Downer, V. Gondhalekar, and B. G. Johnson, "An Active Magnetic Suspension for Space-Based Microgravity Vibration Isolation," in Active Noise and Vibration Control-1990, NCA-vol. 8, ed. G. E. Warnaka, C. Radcliffe, A. H. von Flotow, 1990, pp. 49-56

7 Gerhold, C. H., and R. Rocha, "Active Vibration Control in Microgravity Environment," paper presented at the 1987 ASME Design Technology Conferences - 11th Biennial Conference On Mechanical Vibration and Noise, DE-Vol. 4, pp. 57 - 63, September, 1987.

8 Pennwalt Corporation, "Kynar Piezo Film Technical Manual," Copyright 1987, Pennwalt Corporation.

9 de Luis, Javier, "Design and Implementation of Optimal Controllers for Intelligent Structures Using Infinite Order Structural Models,"

MIT PhD Thesis, Department of Aeronautics and Astronautics, January, 1989.

10 Anderson, E. H., D. M. Moore, J. L. Fanson, M. A. Ealey, "Development of an Active Truss Element for Control of Precision Structures," in "Optical Engineering," Volume 29, number 11, November 1990, ISSN 0091-3286, pp. 1320-1327.

11 Toda, Minoru, "Electromotional Device Using PVF2 Multilayer Bimorph," *The Transactions of the* IECE *of Japan*, Vol. E 61, No. 7, July, 1978, pp. 507-512.

12 Thomas and James E. Hubbard, "Distributed Piezoelectric-Polymer Active Vibration Control of a Cantilever Beam," *Journal of Guidance, Control, and Dynamics*, Vol. 8, No. 5, September/October, 1985, pp. 605-611.

13 Horn S. and Malind Gadre, "Active Vibration Isolation by Polymer Piezoelectret with Variable Feedback Gains," AIAA *Journal*, Vol. 26, No. 8, August, 1988, pp. 1014-1017.

14 Sirlin, Samuel W., and Robert A. Laskin, "Payload Isolation and Precision Pointing For the 1990's," *Proceedings of the Annual Rocky Mountain Guidance and Control Conference*, American Astronautical Society Paper AAS 85-010, February 1-5, 1985, pp. 39-60.

15 Sirlin, Samuel W., and Robert A. Laskin, "The Softmounted Inertially Reacting Pointing System (SIRPNT)," *Proceedings of the Annual Rocky Mountain Guidance and Control Conference*, American Astronautical Society Paper AAS 86-007,February 2-6, 1986, pp. 85-105.

16 Sirlin, S. W., "Piezoelectric Polymer-Based Isolation Mount for Articulated Pointing Systems on Large Flexible Spacecraft," AAS/AIAA Astrodynamics Specialist Conference, Paper AAS 87-456, Kalispell, Montana, August 10-13, 1987.

17 Schoen, E., and F. Seifert, "The Protein Crystallization Facility (PCF) for EURECA," *Acta Astronautica*, Vol. 15, No. 6/7, 1987, pp. 441-448.

18 Hughes, Peter C., *Spacecraft Attitude Dynamics*, John Wiley and Sons, New York, 1986, pp. 232-353.

19 Waters, L., M. Heck, and L. DeRyder, "Steady State Micro-G Environment on Space Station," AIAA paper 88-2462, 1988.

20 Pue, A. J., K. Strobehn, and J. W. Hunt, "Configuration Trade-Offs for the Space Infrared Telescope Facility Pointing Control System," AIAA article 85-1856.

21 Aubrun, J. N. , et al., "Vibration Control of Space Structures (VCOSS) VCOSS A: High- and Low-Authority Hardware Implementations," Final Report, AFWAL-TR-83-3074, Lockheed Missiles and Space Company, Sunnyvale CA, July 1983.

22 Schwaniger, A. J. Jr., W. Baily, and J. L. Tveekrem, "Orbiter Motion (Microgravity and Pointing)," 26th Aerospace Sciences Meeting, January 11-14, 1988/Reno, Nevada, AIAA paper 88-0013, 1988.

23 King, Tony, "Overview of the Microgravity Disturbance Experiment (MDE)," Viewgraph presentation, March 14, 1990, Rockwell Space Operations Co.

24 EVIS table Turechek, John H., "EVIS: the first general purpose active vibration isolation system," Newport Corporation, Fountain Valley, CA, 1986.

25 Miller, D., et. al., "The M.I.T. Multipoint Alignment Testbed: Technology Development for Optical Interferometry," paper to be presented at the SPIE 36th Annual International Symposium on Optical and Optoelectronic Applied Science and Engineering: Active and Adaptive Optical Components Conference, San Diego CA, July 21-26.

26 Nash, William A., *Schaum's Outline of Theory and Problems of Strength of Materials*, 2nd ed., McGraw-Hill Book Company, New York, 1977, pp. 291-311.

27 Crandall, S. H., N. C. Dahl, T. J. Lardner, *An Introduction to the Mechanics of Solids*, 2nd ed. with SI Units, McGraw-Hill Book Company, New York, 1978.

28 Huntington, Andrew, “Final Report on SIRPNT Lab Work, Summer 1987,” JPL Technical Memorandum, Jet Propulsion Laboratory, Pasadena, CA, September 17, 1987.

29 Chatigny, Victor, Pennwalt Corporation, Valley Forge, PA, personal communication, June 1990.

30 Peters, Rex B., "Noise PSD Measurement of a High-Performance Accelerometer with Motion Cancellation," ISA Proceedings, 1984.

31 Peters, Rex B., Principal Engineer, Sundstrand Data Control, Inc., Redmond, WA, Personal communication, May, 1990.

32 Hirsch, Kelly and Dave Patzwald, "Upgrade of Accelerometer Stability Test," EEL 478 Design Lab Report, Sundstrand Data Control, Redmond, WA, Winter, 1987.

33 Ewins, D. J., Modal Testing: Theory and Practice, Research Studies Press Ltd., Taunton [England] 1984.

34 Meirovitch, Leonard, Elements of Vibration Analysis, 2nd ed., McGraw-Hill Book Company, New York, 1986.

35 Structural Measurement Systems, "STAR Reference Manual," Structural Measurement Systems, January, 1990.

36 Rodden, H. J. et al., "Line-of-Sight Performance Improvement with Reaction-Wheel Isolation," Proceedings of the Annual Rocky Mountain Guidance and Control Conference, American Astronautical Society Paper AAS 86-005, February 2-6, 1986, pp. 71-85.

37 Davis, L. P., et al., "Hubble Space Telescope Reaction Wheel Assembly Vibration Isolation System," NASA Marshall SFC, Huntsville AL.

38 Davis, Porter, and Frank Schmitt, "A Feasibility Study to Investigate the Implementation Issues for a Low-Cost Isolation Stage for the Space Station Attached Payload Pointing System," Final Presentation and Report to JPL by Honeywell Satellite Systems Division, December 15, 1988.

39 von Bun, Friedrich O., Owen K. Garriott, and Don J. Pearson, "Nano-g Environment on the Orbiter of Space Station," *Acta Astronautica*, Vol. 17, No.5, pp. 1155-1160, 1988.

40 Reasenberg, Robert D., "Microarcsecond Astrometric Interferometry," Workshop on Optical Interferometry in Space.

41 FEAMIS, 1981 Hamilton, Brian J., "Stability of Magnetically Suspended Optics in a Vibration Environment," Pub. No. 69-1554-02-00, Sperry Flight Systems, June 1981.

42 Zaremba, J. G., "A Biaxial Fast Steering Mirror For Precision Optical Pointing Systems," AIAA 88-4108-CP, 1988.

43 Hamilton, Brian J., et al, "Pointing Mount with Active Vibration Isolation For Large Payloads," Proceedings of the Annual Rocky Mountain Guidance and Control Conference, American Astronautical Society Paper AAS 87-033, 1987, pp. 299 - 318.

44 Hamilton, Brian J., J. W. Aldrich, and Patrick J. Wolke, "Characterization of the VIPS Magnetic Force Actuator," AIAA paper 88-1988, 1988.

45 Sundstrand Data Control, Inc., "Q-Flex Accelerometers Instruction Manual," Copyright 1986, Sunstrand Corporation, pp. 1-1 - 1-5.

Appendix A

Review of Available Passive and Active Hardware

A.1 Passive

There are three basic categories of passive isolation: soft, tuned, and free. A soft passive mount allows low frequency forcing to be transmitted between two bodies while filtering out higher frequency disturbances. A tuned passive mount damps out disturbances at one particular frequency. A free passive mount is one where there is no connection at all. All three mounts are illustrated schematically in Figure A.1.

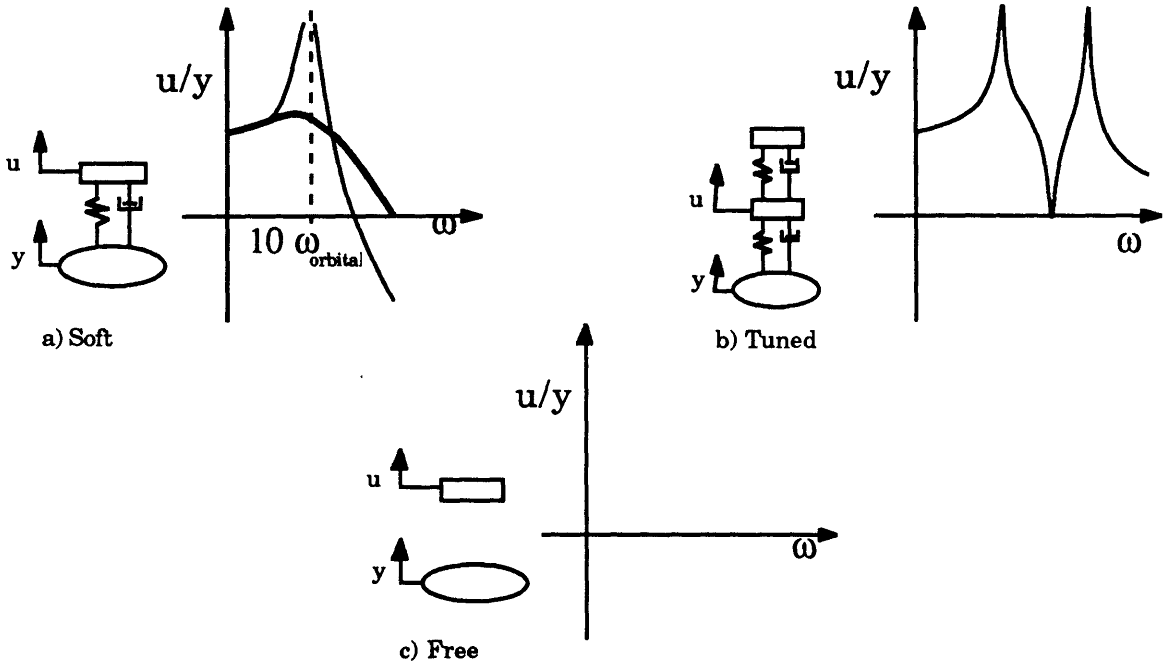

a) Soft

b) Tuned

c) Free

Figure A.1: Types of passive damping and isolation

The transmission of a disturbance or force across any spring, whether soft or stiff, is illustrated by its transmissibility function (Figure A.1). The level at which the force or disturbance acting on the basebody (position variable y) is transmitted to the payload (position variable u) depends on the value of the excitation frequency relative to the natural frequency of the whole spring-mass system. At frequencies no higher than a factor of ten below the mount resonance frequency, the excitation of the basebody is transmitted to the payload without amplification or attenuation; while at frequencies above the mount resonance, the level of excitation transmission decreases, or rolls off, as the excitation frequency increases. In the vicinity of the mount resonance, the excitation is amplified; the level of which depends on the amount of damping in the mount. With no damping, the amplification level at resonance is infinite and the transmissibility function rolls off with a slope of $-1/\omega^2$ (-40 dB/decade on a log-magnitude plot). When viscous damping is added the height of the resonant peak is lowered, while the function rolls off with a slope proportional to $-1/\omega$ (-20 dB/decade).

An example of the application of the soft mount method of passive vibration isolation is that of passive dampers attached to the reaction wheel assemblies on the Hubble Space Telescope (HST).[36,37] The HST is a free flying spacecraft that is pointed in a desired direction by torquing against freely rotating wheels. The vibration resulting from the rotation of these wheels was contributing more than the 0.0033 arcsec error budgeted for this vibration source. In fact, this was more than desired accuracy of 0.007 for the whole space telescope itself. The multi-axis mechanical / fluid mount shown in Figure A.2 with a resonant frequency of 20 Hz reduced this error contribution by over a factor of two, down to its acceptable level. This type of soft mount vibration damper has also been suggested for use with a potential payload pointing system on the Space Station.[3,38]

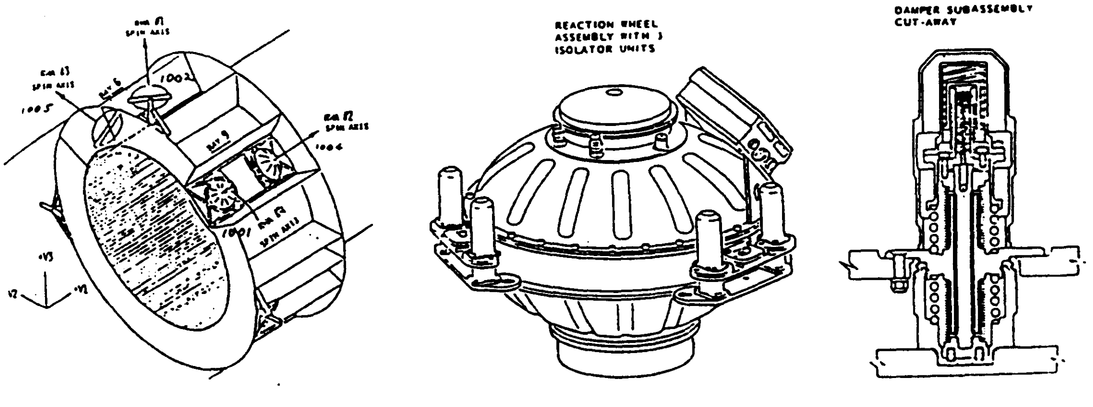

Figure A.2: Hubble Space Telescope vibration dampers and their locations on the reaction wheels on the spacecraft

The disturbance environment aboard the planned Space Station can be ameliorated by such isolation of disturbance sources. Figure 2.5 suggests that many on board disturbance sources are candidates for soft mount isolation, and that the resonant frequency of such a soft mount could be much lower than 20 Hz, perhaps as low as 10^{-3} Hz.

Sensitive instruments and materials processing modules can be similarly soft mounted. To quantify the stiffness of such a mount, it is useful to consider a specific example, the 4000 kg SIRTF instrument mounted to the Space Station at a location 5 m from the Space Station mass center. A mount translational resonant frequency of 3.6×10^{-3} Hz (20 times the frequency of atmospheric disturbances) is achieved by a spring constant of 2.1 N/m. The static gravity gradient deflection of this mount is then 2.5 cm. This is a very soft spring, perhaps an order of magnitude softer than that of a typical helical cord on an office telephone.

It is difficult to visualize implementing a multi-axis design for supply lines with effective stiffness as low as this. It thus appears that the soft mounting of sensitive instruments will be strongly constrained by the need to provide for data and power cabling and plumbing, and that practical soft mount resonant frequencies will not be as low as 10^{-3} Hz. If we assume that the lowest practical mount frequency is 10^{-1} Hz, then 10 Hz disturbances (from on board machinery) will be attenuated perhaps 50 dB. This may be a sensible compromise for passive soft mounting.

Tuned mounting creates a resonant system that opposes a specific disturbance frequency (Figure A.1). A zero is introduced into the transmissibility function and tuned such that it is in the vicinity of the undesirable resonant frequency. If single frequency disturbance attenuation is required, this method may be more appropriate than a power consuming active isolation system.

In an attempt to extend the micro-gravity capabilities of platforms such as the Space Station down to nano-g levels, it has been suggested that certain payloads be allowed to float freely for certain periods of time.[7,39] They become orbiting bodies in their own right. This is pure - or free - isolation. It has even been suggested that the Space Station fly itself around a payload to achieve zero-g free-fall for an indefinite period of time. This would make the stationkeeping of the platform more difficult. If the payload is not located at the center of gravity of the MPP, the ACS will have to apply a constant centripetal acceleration to the platform. This is costly in terms of fuel and weight and may also have adverse effects on other sensitive payloads. If the payload is allowed to co-orbit with the MPP, it can only go for certain periods of time before it will drift too far away or impact with it. If the payload is following behind the platform, the drift time is a just a matter of drag differential between the payload and the platform. When the payload is in the same orbit with a slightly different inclination, they may collide at twice the orbital rate - a collision every 45 minutes in LEO. A payload constrained to drift no more than a meter will have a couple of minutes of free-fall at this altitude.

A.2 Active Isolation

A.2.1 Mechanical Hard Mounts

In space, pure mechanical isolation has mostly been achieved through the passive methods discussed above and/or by designing a proper compensator that is implemented with an already existing positioning system. The latter method is usually applied to hard mounted structures whose position is controlled by a servo-mechanical system where precise positioning and large forces are required. The main applications for this type of technology are for astrometry missions where present missions such as the Hubble Space Telescope must maintain a pointing stability of 7 masec.[36] Missions proposed for deployment after the turn of the century have pointing requirements of a μasec and or positioning requirements, dictated by the need to resolve down to a fraction of a wavelength of light, on the order of 10 nm.[25,40] The servo-mechanical system using traditional motors most popular for this type of application is that of a gimballed structure. This is shown in Figure A.3. This type of mount is too stiff to be practical for pure vibration isolation. If there were only a few well identified disturbances, the payload could be isolated by tuning a passive isolator or by designing an active notch filter compensator that provides isolation in a narrow frequency band. Unfortunately, on a platform such as the space station there are many disturbances spread throughout the disturbance spectrum. Large forces would have to be applied at high accuracy in order for a stiff isolation mount to work. Soft isolation schemes offer a more reasonable chance of success

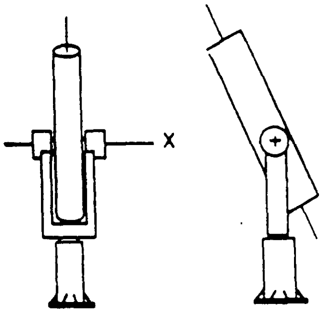

Figure A.3: Generic gimbal mount

A.2.2 Magnetic Mounts

Magnetic mounts offer vibration isolation and positioning actuation simultaneously, even down at the sub-Hz level. It is a type of soft mount (relatively low mount stiffness). This type of mount works by varying the electric current in magnets creating a magnetic field across a gap between the payload and the mount. The payload never touches the mount and is practically a free flyer. The only forces induced on the payload are those created by the magnetic field, making the system very flexible. It can be adapted for a number of payloads simply by making software changes. This also may make the system very robust with respect to modelling errors. Magnetic systems have the potential to give good isolation and pointing capabilities, but appear never to have been implemented in space.

A magnetic mount can be used as the sole actuation method for isolation purposes.[4,5] A transmissibility rolloff slope of 100 dB/decade and -80 dB of isolation have been achieved in the lab for the Fluids Experiment Apparatus Magnetic Isolation System (FEAMIS). This is a vast improvement over passive techniques which tend to roll off with a slope of -20 dB / decade. The basic governing equations of this actuation method are given in Reference 41.

Unfortunately, the efficiency of the magnetic actuator varies with the inverse square of the gap across the actuator. Most actuators have gaps on the order of millimeters. This also translates to a pointing range of only a couple of degrees. A Biaxial Fast Steering Mirror has been produced by

TRW with resolution down to 0.5 m-radians over ± 1 degree for a 0.7 to 2.5 inch diameter magnetically suspended mirror of a precision optical pointing system.[42] Thus magnetic pointing lends itself well as a vernier actuation / isolation stage on top of a coarse mechanism.[3]

Magnetic actuation should be used when vernier RW or CMG systems cannot provide the necessary accuracy. Magnetic actuation demands more power than gimballed systems. One such instrument is the Annular Suspension and Pointing System (ASPS). It uses the Advanced Gimbal System, a gimballed pointing system with 12 microradian stability, in conjunction with a magnetic isolation / vernier stage. The pointing stability improves to 0.05 microradian (0.01 arcsec) without adversely affecting the other performance characteristics. These numbers are the result of a Space Shuttle environment simulation.[2] The vernier actuator is similar to the Vibration Isolation and Pointing System (VIPS) actuator which produces ± 18 N of force allowing ± 9 mm of motion with 0.05% accuracy over a bandwidth of at least 25 Hz. The isolation achieved has a spring constant of 0.03 N/m. This is less than that deemed necessary above for soft passive isolation of a 4000 kg payload. Staged actuation has been also demonstrated for a linear force transmission set-up capable of producing forces in excess of 1000 pounds with -80 dB disturbance attenuation.[43] The magnetic pointing stability levels mentioned here are comparable to those of free flying payloads using reaction wheels or CMGs for pointing and attitude control (Hubble ST - 0.034 micro-radian pointing stability).

Magnetic isolation systems are at a relatively advanced state of development and definitely capable of achieving performance specifications. One factor to keep in mind is the need for its magnetic gap to stay at a small magnitude due to the power requirements involved and the non-linearity of the actuator.

A.2.3 Piezoelectric Actuators

The piezoelectric actuator options are discussed in section 2.5.1.

A.2.4 Other Actuation Methods

The above actuation methods are not the only possible solutions. As touched upon in the passive isolation section, air jets can be used to keep a floating table on the Space Station from drifting away.[7] The jets are controlled in such a way that the acceleration on the floating module is less than 10^{-5} g. A payload mass of up to 450 kg is enclosed in 106.7 cm wide x 190.5 cm high x 76.2 cm deep rack. There ARE other ways of implementing the soft spring approach. The soft spring ideally isolates the payload enough so that it is essentially a free flyer. Restraining methods using active tethers (inflatable or piezoceramic actuated) or guy wires have been considered.[14]

Appendix B

Sensor Options

B.1 Overview

This appendix is meant to illustrate the importance in the choice of sensor used in the microgravity isolation problem. The use of a force transducer adds to the hardware that must be assembled and built; but it may be necessary if sensors of this type are manufactured with resolution better than the Sundstrand accelerometers in the frequency rang of interest. If soft force transducers are used, additional restrictions may be put on the associated extra hardware and the dynamics of the system are altered so that a different compensator is needed. The choice of sensor type can make the system unnecessarily complicated.

B.2 Accelerometers

Since performance has been specified with respect to acceleration, an accelerometer is the natural choice for this application. Accelerometers generally work under the principle of measuring the force transmitted from the accelerometer casing to a calibrated mass through some calibrated force transducer. The acceleration is proportional to this force by a factor which is exactly that of the mass. The types of existing accelerometers are essentially the same as the types of existing force transducers.

Commercial accelerometers other than the Sundstrands addressed in section 4.2.3 were considered but determined to be inappropriate for this project either because of the inability to achieve the desired resolution or its inability to operate in the desired frequency range. Piezoelectric accelerometers have the theoretical capability of resolving down to the sub μg level but this technology has not yet been refined sufficiently for commercial use. Since piezoelectric materials only react to changes in strain and not steady state excitations, they do not perform well at the low frequencies inherent in this experiment. A charge amplifier which gathers the electrons produced by the mechanical strain of a piezoelectric material must not allow these electrons to leak at a rate noticeable at these low frequencies. A quick attempt was made to develop such an accelerometer because of its absence from the market and the requirement of apparently only needing to construct the appropriate amplifier. A piezoceramic bender was cantilevered so that a force could be applied at the tip. The appropriate force levels could be observed on an oscilloscope but its total magnitude drifted wildly at low frequencies due to local temperature changes in the lab. This approach was abandoned due to the need to develop reasonably sized thermal insulation to keep the temperature changes to frequency levels below 0.01 Hz or to keep the magnitudes below a μg. This method does offer hope for future sub-μg resolution accelerometers and force transducers. If the calibrated mass of an accelerometer is as large as the experiment will allow, the sensitivity requirements of the sensor are made less difficult to attain. If the mass is the whole payload the signals of the sensor are as large compared to the experimental noise as possible.

B.3 Force Transducers

With the original impression that acceptable accelerometers were not available, effort was put into producing a force transducer that could measure the force transmitted to the payload through its mounting structure. Its acceleration can then be deduced by dividing by its mass. These methods are still worth mentioning since they are a viable design option for future missions of this type. As described in the accelerometer section this type of technology may also be directly applicable to the development of new accelerometers. Many methods were looked into and were subject to some additional constraints. Since the transducer would be in series with the mounting structure, it is important that the dynamics of the sensor not interact adversely with those of the mount and the payload. If its stiffness is similar in magnitude to that of the mount, its resonant frequency will change; and if it has any internal resonances in the frequency range of interest, not only must this be taken into account, but it is likely that it may destabilize the system or make it too difficult to achieve necessary isolation levels. Also, since the sensor must work in multiple degrees of freedom, the sensor must be its stiffest in the degree of freedom or direction of the applied force; otherwise, if the sensor is stiffer in directions other than this, the majority of the force will be applied through unmeasured degrees of freedom. In the case of this experiment, an approach can be taken is where the arcs can apply a force to an intermediate box or series of platforms and force transducers inhabit the gap between the intermediate structure and the payload on at least two sides. These force transducers are stiffest in their extensional directions so that when lateral force is applied to the box relative to the force transducers on one side, the force is essentially transmitted through the sensors on one of the sides perpendicular to the one first mentioned. When these force transducers become soft, and they are not stiff enough to act like a rigid component near the control bandwidth of the experiment, additional dynamics are introduced into the system. The system can be destabilized by what is effectively a high frequency roll off in the controller. They can be analyzed using the representative linear two spring two mass system shown in Figure B.1. The intermediary box takes on the form of the middle mass and the force transducer stiffness dictates the stiffness of the spring between the intermediate mass and the payload. The extra effort involved in developing and implementing a force transducer instead of using a commercially available accelerometer can readily be envisioned.

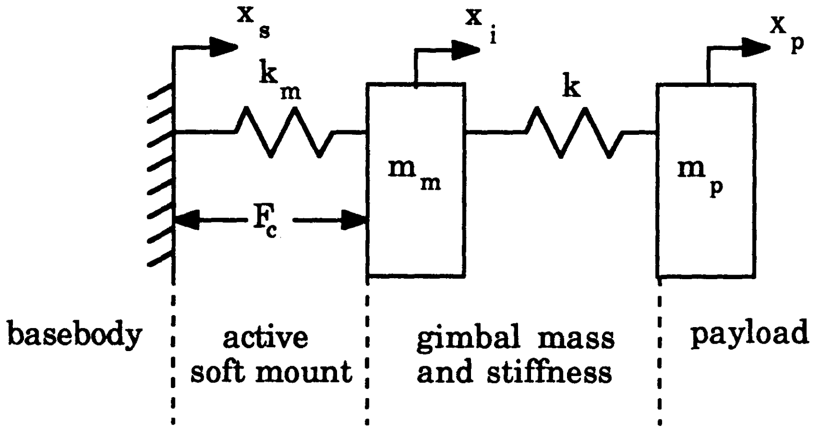

Figure B.1: Two spring - two mass - rigid wall model of a microgravity facility with a soft force transducer. The PVDF mount is represented by the spring attached to the wall, the sensor by the spring between the two masses, the payload by the mass furthest away from the wall, and the intermediate box by the intermediate mass.

There are some basic approaches to designing a force transducer. Two very common methods are where one can measure the strain of a component as it is deformed or one can measure the relative displacement change between two ends of such a component with the knowledge of the corresponding spring constant. Other transducers take advantage of the fact that the resonant frequencies of materials or components change when under different loading conditions .[8,44] The last kind that will be mentioned here is where a mechanism is incorporated into the transducer where when a deformation is sensed, an opposing reaction is induced so that the deformation is cancelled out. The resulting resistant effort is related to the initial force. This is essentially one of the first two approaches with the added ability to oppose the deformation. All of these types can be implemented with a calibrated proof mass to become an accelerometer. It has been previously mentioned that it is desirable to have sensors that are stiff or 'hard' compared to the mount so that it appears rigid in the control frequency of interest. The second pair of sensor types are usually hard sensors as applied to this problem. The Sundstrand Q-Flex accelerometers are of the kind where the measured signal is that of the effort needed to cancel out the effect of the disturbing force. The tip displacement of a precision quartz flexure is measured using a capacitive probe and the deformation is zeroed out using a magnetic coil assembly that works much like a speaker diaphragm.[45] The resonator type of transducer is also capable of producing the desired resolution.[29,44] This involves attaching a vibration sensor to a calibrated component, such as a quartz sheet, whose resonant frequency is relatively stable with respect to other environmental disturbances, thermal for example. Its resonant frequency changes are thus due mainly to the applied forces. However, upon consultation with people familiar with this type of accelerometer, it was decided that it would be potentially very expensive and, of more concern, that it would require more time to build and calibrate than practical to complete the microgravity experiment.[29,44] In fact, it was implied that the reason for the unavailability of this type of sensor for commercial use is due to the lengthy calibration procedure.[29] These types of hard sensors are capable of producing the desired resolution but were impractical due to logistical matters.

With the hard type of transducer impractical for use, soft transducers are investigated. Many types of systems can be devised using soft components. Noncontact displacement transducers with resolutions as small as 1 to 10 nm can be placed in parallel with these soft components. If it is desirable to resolve below a μg, then the necessary force resolution on a 100 kg. mass must be less than 1 mN, preferably by at least an order of magnitude. When 1 nm resolution is translated into 0.1 mN force resolution, the stiffness of the sensor must be less than 100 N/m. This is only five times the stiffness of the PVDF mount. If the inner box were on the sensor suspension instead of the PVDF suspension, the resonant frequency would be 1 rad/s (0.16 Hz). In the two spring mass system, if the sensor system is much stiffer than the PVDF mount, the frequency of the light intermediate mass vibrating on top of the more massive payload approaches $\sqrt{k_{sensor}/m_{intermediate}}$. If the intermediate mass is taken to be as low as 0.1 kg, this mode is at approximately 5 Hz. The dynamics of a "soft" force transducer must be accounted for in the compensator to ensure a stable high frequency roll off and avoid any dynamic coupling with the PVDF actuator.

Appendix C

PVDF Piezoelectric Film Properties

Table C.1: Typical Properties of Piezo Film.[8]

Property	Symbols	Values	Units
Piezo Strain	d_{31}	23×10^{-12}	(m/m)/(V/m)
Constant	d_{32}	3×10^{-12}	or
	d_{33}	-33×10^{-12}	
	d_t	-22×10^{-12}	$(C/m^2)/(N/m^2)$
		0.16	$(C/m^2)/(m/m)$ or
	e_{33}		$(N/m^2)/(V/m)$
Piezo Stress	g_{31}	216×10^{-3}	$(V/m)/(N/m^2)$
Constant	g_{32}	19×10^{-3}	
	g_{33}	-339×10^{-3}	or
	g_t	-207×10^{-3}	$(m/m)/(C/m^2)$
Electro-mechanical	k_{31}	12	% @ 100Hz (Vf_2)
Coupling Constant	k_t	29	% @ 100 MHz (Vf_2/Vf_3)
Capacitance Film	C	379×10^{-12}	F/cm^2 for 28 μm @ 10 KHz
Electrical Impedance	Z_e	1350	ohms for 100 cm^2 for 9 μm film@ 1KHz
Volume Resistivity	ρ_v	1.5×10^{13}	ohm-m @20° C
Mechanical Loss Tangent	tan-δ_m	0.10	
Max. Operating	E_o	10	V/μm @ d.c.
Field		30	V/μm @ a.c.
Density	ρ	1.78×10^3	kg/m^3
Elongation at Yield	SY	2-5	%
Young's Modulus	Y	2×10^9	N/m^2

Appendix D

Alternative Derivation of Arc Piezoelectric Properties

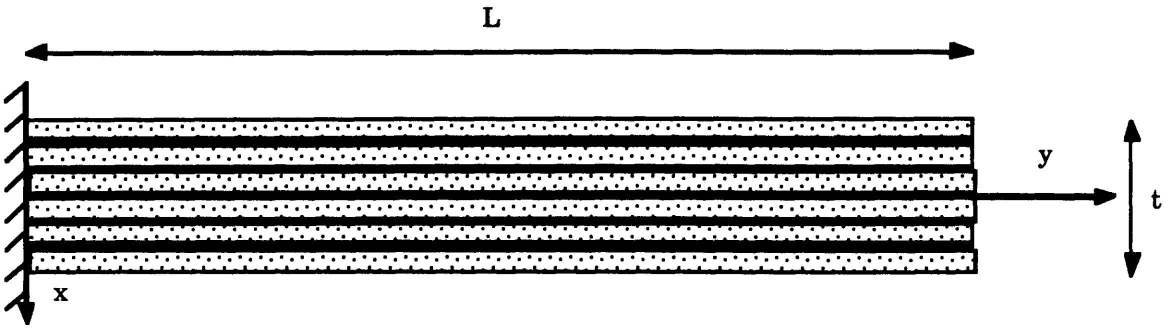

Figure D.1: Clamped-free laminated piezoelectric film beam with glue layers.

The following derivation of the displacement characteristics of a piezoelectrically excited PVDF arc is shown below to confirm the gross piezoelectric properties. For the laminated clamped-free beam of thickness t and length L in Figure D.1, the strain energy is

$$U = \frac{tL}{2} \int_{-t/2}^{t/2} E\varepsilon^2(x)\, dx \qquad (D.1)$$

and the corresponding strain due to bending is

$$\varepsilon(x) = \frac{\partial\psi}{\partial y} x - \varepsilon_p \qquad (D.2)$$

where, $\frac{\partial\psi}{\partial y}$ = the beam curvature,

$\varepsilon_p = \frac{d_{31}V}{t_p}$ = the piezoelectrically induced strain,

t_p = the thickness of each piezoelectric layer, and

d_{31} = the induced strain for an applied electric field.

Also, since the strain is symmetric about the center-line of the beam, the integral becomes

$$U = tL \int_{0}^{t/2} E\varepsilon^{2}(x)\, dx \tag{D.3}$$

When multiple layers are used, this integral turns out to be the sum of many such integrals. The first term will be that of the central glue layer integrated from its center, $x = 0$, to the start of the first piezoelectric layer, $x = h_{gl}/2$. h_{gl} is the thickness of the glue layer. This term will have no piezoelectrically induced strain but it has its own extensional modulus, E_{gl}. The second term represents the piezoelectric layer pair closest to the center-line. This integral goes from $x = h_{gl}/2$ to $x = h_{gl}/2 + h_p$. h_p is the thickness of the polymer piezoelectric layer. This second integral *will* have have the piezoelectrically induced term. Since this integral has to be evaluated each time for a laminate with a new number of layers the integral is only calculated here with a single pair of PVDF layers and a zero thickness glue layer. This is good enough for an approximate number because the glue layers are relatively small compared to the PVDF layers and they have a comparable extensional modulus. However, if more than just an approximation is needed, the glue layer, its thickness, and its modulus should be included.

When the glue layer is ignored, the integral in Eq. D.3 becomes

$$U = EtL \int_{0}^{t/2} \left(\frac{\partial\psi}{\partial y} x - \varepsilon_p\right)^{2} dx \tag{D.3}$$

and upon evaluation the strain energy is

$$U = EtL\left[\left(\frac{\partial\psi}{\partial y}\right)^{2}\frac{t^3}{24} - \frac{\partial\psi}{\partial y}\frac{t^2}{4}\varepsilon_p + \frac{t}{2}\varepsilon_p^{2}\right] \tag{D.4}$$

At equilibrium the energy is at a minimum with respect to the unfixed physical characteristic, namely the curvature.

$$\frac{\partial U}{\partial\left(\frac{\partial \psi}{\partial y}\right)} = EtL\left[\left(\frac{\partial \psi}{\partial y}\right)\frac{t^3}{12} - \frac{t^2}{4}\varepsilon_p\right] = 0 \qquad (D.5)$$

The additional curvature induced by the applied voltage can then be solved for. It is stated below, along with new radius, r, of the arc.

$$\frac{\partial \psi}{\partial y} = \frac{3\,\varepsilon_p}{t} \qquad (D.6)$$

$$r = \frac{1}{\frac{1}{R} + \frac{\partial \psi}{\partial y}} \qquad (D.7)$$

where R is the Radius of the arc when no voltage is applied. The total displacement of the arc tip from the equilibrium position is then the difference between the initial and new radii plus the extra distance the tip has travelled now that it is an arc of arc angle greater than π radians. The total radial and circumferential displacements are

$$\delta_p = 2(R - r) + r(1 - \cos\beta) \qquad (D.8)$$

$$\delta_q = r \sin\beta \qquad (D.9)$$

where β, the change in angular arc length, can deduced by taking advantage of the fact that the arc circumferential length does not change. It is expressed below in terms of the zero voltage arc angle, Ψ_o.

$$\beta = \left(\frac{R}{r} - 1\right)\Psi_o \qquad (D.10)$$

The above displacements are then be expressed below in terms of the applied piezoelectric voltage, V.

$$\delta_p = 2R - \left(\frac{Rth_p}{th_p + 3Rd_{31}V}\right)\left(1 + \cos\left(\frac{3Rd_{31}V}{th_p}\right)\right) \qquad \text{(D.11)}$$

$$\delta_q = \left(\frac{Rth_p}{th_p + 3Rd_{31}V}\right)\sin\left(\frac{3Rd_{31}V}{th_p}\right) \qquad \text{(D.12)}$$

These relations are not linear. This is different from the relations developed in the main body of the text. Keeping in mind that these equations do not account for the ineffectiveness of the glue layers, these relations can be used to predict the voltage-displacement relationship of actuator # 6 shown in Figure 5.3. The actuator is 193 μm thick with a radius of 0.0378 m. When the maximum electric field of 30 V/μm is applied, a vertical displacement of 4.1 cm and a horizontal displacement of 2.6 cm are predicted. Although these predictions are still not as high in magnitude as the measured displacement and would be lower still when the glue layer is taken into consideration, they are nonetheless closer than any of the previously mentioned linear analyses. If the prediction methods of this appendix are then linearized about the operating point of V = 0, the prediction is no better than the linear analysis of the main body. However, this model is handy to have since the plant is nonlinear; and a control scientist may want or need to use this model in the design of a controller.